A MEMS Multi-Cantilever Variable Capacitor On Metamaterial

THESIS

Luke Rederus, Captain, USAF

AFIT/GE/ENG/09-35

DEPARTMENT OF THE AIR FORCE
AIR UNIVERSITY

AIR FORCE INSTITUTE OF TECHNOLOGY

Wright-Patterson Air Force Base, Ohio

APPROVED FOR PUBLIC RELEASE; DISTRIBUTION UNLIMITED.

The views expressed in this thesis are those of the author and do not reflect the official policy or position of the United States Air Force, Department of Defense, or the United States Government.

AFIT/GE/ENG/09-35

A MEMS Multi-Cantilever Variable Capacitor On Metamaterial

THESIS

Presented to the Faculty

Department of Electrical and Computer Engineering

Graduate School of Engineering and Management

Air Force Institute of Technology

Air University

Air Education and Training Command

In Partial Fulfillment of the Requirements for the

Degree of Master of Science in Electrical Engineering

Luke Rederus, B.S.E.E.

Captain, USAF

26 March 2009

APPROVED FOR PUBLIC RELEASE; DISTRIBUTION UNLIMITED.

AFIT/GE/ENG/09-35

A MEMS Multi-Cantilever Variable Capacitor On Metamaterial

Luke Rederus, B.S.E.E.

Captain, USAF

Approved:

26 Feb 09

LaVern A. Starman, PhD, Maj, USAF (Chairman) — date

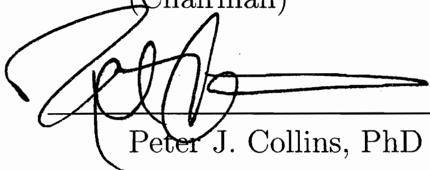

19 FEB 2009

Peter J. Collins, PhD (Member) — date

19 Feb 09

Ronald A. Coutu, Jr., PhD, PE, LtCol, USAF (Member) — date

AFIT/GE/ENG/09-35

Abstract

Negative refractive index materials are an example of metamaterials that are becoming increasingly popular. Research into these metamaterials could possibly be the first steps toward bending electromagnetic radiation (i.e., microwaves, light, etc.) around an object or person. Split ring resonators (SRR) are classified as metamaterials that create an artificial magnetic response from materials with no inherent magnetic properties. Once fabricated, an SRR has a specific resonant frequency due to its permanent geometry.

This research introduces a new concept of using a variable capacitive micro-electro-mechanical system (MEMS) device located at the gap of an SRR to mechanically alter the capacitance of the SRR structure and thus change its resonance. This design simplifies fabrication and uses less space than a varactor diode or MEMS switch since the MEMS device is the capacitive element and is fabricated in-situ with the SRR. This research is the first known to demonstrate the fabrication of a MEMS tuneable capacitive device on an SRR.

This thesis reports on the model, design, fabrication, and testing of the capacitive MEMS device as a stand-alone test structure and as located on an SRR. When pulled-in, the cantilever beams each add between $0.54 - 0.62$ pF.

Acknowledgements

Thanks to: My parents, sister, and G-ma for encouragement and support! Luke Rolfes for being a great friend. All the guys here for support during classes and on my thesis: Adam, Tod (WoW), James, Moe, Mimi, Dan, and Coleman. Bob, Sean, Trev, Phil, Howie, and Charlie for being awesome friends. And to James, Ben, Chris, Danny, and Eric—my good Florida buddies that I had to leave to come here.

My research would not be possible without the help of many here at WPAFB: Maj LaVern Starman for being my advisor, LtCol Coutu for help with cantilever beam modeling, Capt Kelson Chabak for always letting me in the clean room and helping me out, 1Lt Ginny Miller for dropping my quartz wafer and thus reducing my work load, Paul Cassity for depositing dielectrics, Larry Callahan for excellent wafer dicing skills, Rich Johnston for E-beam evaporation in a day, Mark Robinson at Agilent Technologies for LCR meter help, Dr Peter Collins and Maj Jeff McGuirk for help with metamaterial, and LtCol Fellows for being an awesome teacher.

Luke Rederus

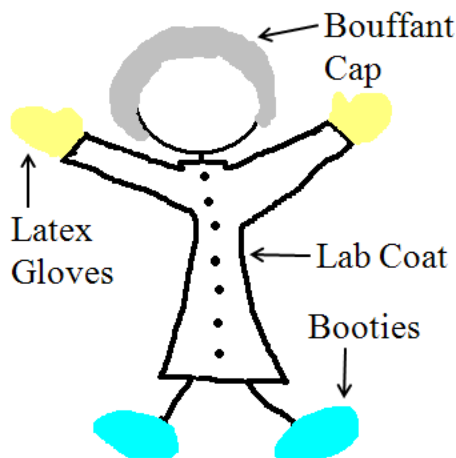

Cleanroom Stick Figure (courtesy of Mimi)

Table of Contents

Page

Abstract iv

Acknowledgements v

Table of Contents vi

List of Figures ix

List of Tables xiii

List of Symbols xiv

List of Abbreviations xviii

I. Introduction 1
- 1.1 Problem Statement 1
- 1.2 Micro-electro-mechanical Systems 2
- 1.3 Research Objectives 4
- 1.4 Design Requirements 4
- 1.5 Organization of Thesis 5

II. Background 6
- 2.1 Chapter Overview 6
- 2.2 Background on Contact and Capacitive Switches 6
  - 2.2.1 Contact Switch 6
  - 2.2.2 Capacitive Switch 13
  - 2.2.3 Designs Increasing Lifetime 19
  - 2.2.4 Varactors 21
- 2.3 Metamaterials 24
- 2.4 Split Ring Resonators 25
  - 2.4.1 Capacitor Loaded SRRs 26
  - 2.4.2 Tunable SRRs 29
  - 2.4.3 Tuning SRRs using MEMS 31
- 2.5 Chapter Summary 33

Page

III. Theory . . . 34
3.1 Chapter Overview . . . 34
3.2 Theory of Design . . . 34
3.3 Cantilever Beam Model . . . 35
3.3.1 Tip Deflection . . . 35
3.3.2 Spring Constant . . . 36
3.3.3 Improved Beam Model . . . 37
3.3.4 Parallel Plate Capacitor Models and Electrostatic Force . . . 38
3.3.5 Pull-in Voltage (Electrostatic Actuation) . . . 39
3.3.6 Improved Pull-in Model . . . 40
3.3.7 Collapse Voltage . . . 42
3.3.8 Release Voltage . . . 42
3.3.9 Dielectric Breakdown Voltage . . . 43
3.3.10 Mechanical Resonant Frequency . . . 44
3.4 Two-port Network Model . . . 45
3.5 Figures of Merit . . . 46
3.5.1 Quality Factor . . . 46
3.5.2 S-Parameters . . . 46
3.6 Split Ring Resonators . . . 47
3.7 Chapter Summary . . . 50

IV. Design and Fabrication . . . 51
4.1 Chapter Overview . . . 51
4.2 Design . . . 51
4.2.1 Varactor Design . . . 51
4.2.2 SRR design . . . 54
4.2.3 SRR with Multi-Cantilever Design . . . 55
4.3 Fabrication . . . 58
4.3.1 Custom Micromachining Process . . . 60
4.3.2 Fabrication Challenges . . . 62
4.4 Chapter Summary . . . 66

V. Analytic Predictions, Modeling, and Simulation . . . 67
5.1 Chapter Overview . . . 67
5.2 Analytic Predictions . . . 67
5.2.1 Pull-in Voltage . . . 67
5.2.2 Capacitance . . . 69
5.2.3 Collapse Voltage . . . 69

Page

5.2.4 Release Voltage 70
5.3 Finite Element Modeling and Simulation 70
5.4 Results Comparison 73
5.5 SRR Comsol Simulations 73
5.6 Chapter Summary 74

VI. Experiments and Test Results 75
6.1 Chapter Overview 75
6.2 Pull-in Voltage Measurements 75
6.2.1 Experiment Test Setup 75
6.2.2 Pull-in Voltage Results 77
6.2.3 Collapse Issues During Pull-in Voltage Tests . . 80
6.3 Capacitance Measurements 83
6.3.1 Experiment Test Setup 83
6.3.2 Capacitance Results 85
6.3.3 Capacitance Measuring Issues 87
6.4 Cantilever Lifetime Test 89
6.5 SRR Testing 90
6.6 S-parameter Measurements 91
6.7 Chapter Summary 91

VII. Conclusions and Recommendations 93
7.1 Overall Summary 93
7.1.1 SRR with MEMS Devices 93
7.1.2 Device Fabrication 93
7.1.3 Experiments and Results 94
7.2 Recommendations for Future Research 94
7.2.1 Design Recommendations 94
7.2.2 Fabrication Recommendations 96

VIII. Appendix 1. Process Followers 98

Bibliography 106

List of Figures

Figure Page

1.1. Split ring resonator unit cell 2

1.2. FET and MEMS switch comparison 3

2.1. Cantilever type contact switch 6

2.2. Parallel plate force model 7

2.3. Cantilever beam at pull-in voltage 8

2.4. Example of surface roughness (a) which leads to a decreased contact area at pull-in (b) 9

2.5. Contact area at pull-in 10

2.6. Plot of measured closed switch resistance vs. applied actuation voltage 11

2.7. Cantilever at collapse voltage 11

2.8. RF MEMS switch with electric contacts and actuation electrode co-located near the beam's end 12

2.9. A capacitive switch layout (a) and cross section view (b) 14

2.10. Parallel plate capacitance models 15

2.11. Dielectric surface roughness 16

2.12. Applied RF power vs. DC pull-down voltage 17

2.13. Calculated temperature vs. power at different frequencies for a capacitive switch 18

2.14. Voltage shift from trapped charge 19

2.15. Waveform of IBA method 20

2.16. Parallel plate variable capacitor 21

2.17. Parallel-plate capacitor with carrier beams 22

2.18. Two types of variable capacitors. The varying length cantilevers (a) pull-in longest-to-shortest. The bridge beam over the longest bottom electrode (b) pulls-in first, followed by the bridge over the next longest electrode 23

Figure | Page

2.19. C–V characteristic of a multi-cantilever capacitor 23

2.20. Cantilever collapsing tip first (a) results in a small contact area that creates a small capacitive change. As voltage is increased, more of the beam pulls-in (b), thus creating a "zipper effect". The extra contact area increase capacitance 24

2.21. SRR with axes labelled 26

2.22. SRR with capacitor loaded between rings (a), across the outer ring gap (b), and across the inner ring gap (c) 27

2.23. Schematic of SRR with dimensions d and t = 200 μm, w = 900 μm, and R = 3.6 mm (a), and a photograph of experimental setup using two monopole antennas for measuring transmission coefficients of a unit cell SRR (b) 27

2.24. Magnetic resonance frequency of an SRR as a function of loaded capacitances at different capacitive regions 28

2.25. Simulated electric field intensity profile at the magnetic resonance frequency of the SRR 29

2.26. SRR with varactor between internal and external split rings . . 29

2.27. Photograph of fabricated SRR with varactor diode 30

2.28. VLSRR resonance behavior 30

2.29. Varactor-loaded SRR system along with circuitry used for voltage biasing 31

2.30. SRR with MEMS switch placed in series 31

2.31. SRR with MEMS switch placed in parallel 32

2.32. Resonance of an SRR without a MEMS switch 32

3.1. Cantilever capacitive switch 35

3.2. Fixed end cantilever with intermediate load 36

3.3. Improved cantilever beam model 38

3.4. Cantilever beam showing electric-flux fringing fields which increase total capacitance 41

3.5. Non-uniform profile of the electrostatic pressure on a cantilever beam during actuation 41

Figure Page

3.6. Fixed end cantilever beam with simple support 43

3.7. A photograph showing dielectric failure 44

3.8. Equivalent circuit model of a capacitive RF MEMS switch . . . 45

3.9. Two-port network characterized by S parameters 47

3.10. SRR equivalent circuit diagram 48

3.11. SRR unit cell with dimensions 49

4.1. Dimensions of cantilever 51

4.2. Multi-cantilever variable capacitor 52

4.3. SRR modified design 54

4.4. SRR unit cell with cantilever array 55

4.5. Close up view of cantilever array 56

4.6. Final L-edit design layout for a 3 in wafer 57

4.7. $300 - 400$ μm cantilever array test structure 58

4.8. Example of a simple surface micromachining process flow for a cantilever beam 59

4.9. Illustration of custom fabrication process 61

4.10. SF-11 planar coating and conformal coating ability 63

4.11. Diagram of tensile and compressive stresses 63

4.12. SEM image showing cantilever beam curling up due to tensile stress introduced during the electroplating process 64

4.13. SEM image comparing electroplated Au from two test wafers . 64

4.14. SEM image showing surface roughness on the underside of a cantilever beam 65

5.1. Calculated pull-in voltages vs. beam length for SaW3 68

5.2. Calculated pull-in voltages vs. beam length for SaW4 68

5.3. Capacitance vs. average pull-in voltage for multi-cantilever array 69

5.4. Summary of custom fabrication process created in the Process Editor of CoventorWare® 71

5.5. Meshed cantilever in CoventorWare® 71

Figure Page

5.6. Generic FEM analysis of cantilever 72

5.7. Permeability of a simulated SRR 74

6.1. Schematic illustration of the experimental test setup used to actuate cantilevers and measure resulting deflection 75

6.2. Zygo interferometer measurement of SaW2 76

6.3. Zygo interferometer measurement of SaW4 cantilever array in the up-state 76

6.4. SEM image of a cantilever stuck in the down-state 77

6.5. Test devices failed due to dielectric breakdown 78

6.6. Pull-in and release voltage results for cantilever array 79

6.7. Zygo interferometer measurement of cantilever array with one beam pulled-in 82

6.8. Actuation of a curved beam 82

6.9. Zygo interferometer measurement of cantilever array with one beam pulled-in with actuation voltage reduced to the point just before beam release 83

6.10. Schematic illustration of the experimental test setup used to actuate cantilevers and then measure resulting capacitance 84

6.11. Observing cantilever deflection using optic focus 85

6.12. CV experimental test measurement for cantilever array 86

6.13. CoventorWare® simulation showing different stages of a collapsed beam 86

6.14. CV experimental test measurement for cantilever array 87

6.15. Measuring capacitance by manually pressing down beams with probe tips 88

6.16. Probes pressing down beam sections directly over electrodes . . 89

6.17. SEM image of SRR unit cell 90

6.18. Waveguide test setup 91

List of Tables

Table		Page
1.1.	RF switch technology comparison	4
4.1.	Coventor color legend for Figures 4.1 and 4.2	51
4.2.	L-edit color legend for Figures 4.4 and 4.5	56
4.3.	Summary of custom fabrication process with deposition thicknesses for SaW3 and SaW4	62
5.1.	Calculated collapse voltages for cantilevers on SaW3 and SaW4	70
5.2.	Calculated release voltages for cantilevers on SaW3 and SaW4	70
5.3.	CoventorWare® simulation results of 300 μm cantilever	72
5.4.	CoventorWare® simulation results of a cantilever array	73
6.1.	Initial SaW4 cantilever array test results with stiction issues	77
6.2.	Initial SaW4 cantilever array test results with breakdown issues	78
6.3.	Comparison of calculated and tested pull-in voltages for a SaW4 cantilever array	81
6.4.	Comparison of calculated collapse voltages and measured pull-in voltages for a SaW4 cantilever array	81
6.5.	Measured capacitance using probe to depress beams onto landing pad	88
6.6.	Capacitance measured when probe tips are used to depress beams onto electrodes	89

List of Symbols

Symbol		Page
F_s	Mechanical Restoring Force	7
F_e	Electrostatic Force	7
d	Distance Between Plates	7
k	Spring Constant	7
A	Surface Area	7
ε_0	Permittivity of Free Space	7
ε_r	Permittivity of Dielectric	7
V_{pi}	Pull-in Voltage	8
R	Resistance	10
ρ	Resistivity	10
L	Length	10
V_{cpi}	Collapse Voltage	11
CO_2	Carbon Dioxide	13
Au	Gold	13
Pd	Palladium	13
Pt	Platinum	13
Cu	Copper	13
Z_C	Reactive Impedance	14
ω	Frequency	14
C	Capacitance	14
t_d	Dielectric Thickness	15
C_{pp}	Parallel Plate Capacitance	15
P_f	Fringing Field Contribution	15
C_d	Capacitance at Down-state	15
Si_3N_4	Silicon Nitride	16

Symbol		Page
C–V	Capacitance-Voltage	19
V_r	Release Voltage	19
SiO_2	Silicon Dioxide	22
HfO_2	Hafnium Dioxide	22
a	Lattice Constant	25
L	Inductance	26
V_{dc}	Voltage Direct Current	31
L_o	Length Cantilever Extends Over SRR	34
F_a	Applied Force	35
a	Distance from Cantilever's Fixed End to Center of Electrode	35
d	Beam Tip Deflection	35
L_b	Cantilever Beam Length	36
$\tilde{E}$	Effective Young's Modulus	36
w_b	Cantilever Beam Width	36
t_b	Cantilever Beam Thickness	36
E	Young's Modulus	36
ν	Poisson's Ratio	36
I_z	Moment of Inertia About Z-axis	36
k_1	Spring Constant for Beam Model	37
d_1	Tip Deflection of Improved Beam Model	37
l	Anchor Height	37
g_0	Initial Gap Between Parallel Plates	37
Q	Charge	38
L_e	Electrode Length	39
g	Gap Height	39
k_{ss}	Simply Supported Beam Spring Constant	42
d_e	Collapse Distance	42
V_r	Release Voltage	43

Symbol		Page
V_{br}	Breakdown Voltage	44
$\vec{E}_{ds}$	Dielectric Electric Field Strength	44
m	Mass	45
V_s	Actuation Voltage	45
R_s	Beam Resistance	45
$C(t)$	Time Varying Capacitance	45
Z_0	Line Impedance	45
f	Frequency	46
μ	Magnetic Permeability	46
σ	Conductivity	46
Q	Quality Factor	46
S	Scattering Parameters	46
S_{11}	Input Reflection Coefficient	47
S_{12}	Reverse Transmission Coefficient	47
S_{21}	Forward Transmission Coefficient	47
S_{22}	Output Reflection Coefficient	47
ω_{pm}	Magnetic Plasma Frequency	48
Γ_m	Material Damping Loss Term	48
L_{av}	Average Inductance of Two Square Rings	48
C_g	Gap Capacitance from Concentric Rings of SRR	48
C_{OR}	Outer Ring Capacitance	48
C_{IR}	Inner Ring Capacitance	48
λ_0	Free Space Wavelength	49
w_{SRR}	Width of SRR's ring	49
ω_{IR}	SRR Inner Ring Resonant Frequency	55
ω_{OR}	SRR Outer Ring Resonant Frequency	55
Ti	Titanium	59
HF	Hydrofluoric Acid	59

Symbol		Page
Si	Silicon	59
Ni	Nickel	96
$SrTiO_3$	Strontium Titanate Oxide	97

List of Abbreviations

Abbreviation		Page
SRR	Split Ring Resonator	1
MEMS	Micro-Electro-Mechanical System	1
RF	Radio Frequency	2
FET	Field Effect Transistor	3
AFIT	Air Force Institute of Technology	4
AFRL/RY	Air Force Research Lab/Sensors Directorate	4
CPW	Coplanar-waveguide	13
IBA	Intelligent Bipolar Actuation	20
EM	Electromagnetic	27
VLSRR	Varactor-Loaded Split Ring Resonator	29
DC	Direct Current	31
PECVD	Plasma Enhanced Chemical Vapor Deposition	53
SEM	Scanning Electron Microscope	58
LIGA	Lithographie, Galvanoformung, Abformung	58
RIE	Reactive Ion Etching	60
PMGI	Polydimethylglutarimide	60
DUV	Deep Ultra-Violet	60
FEM	Finite Element Model	70
LCR	Inductance, Capacitance, Resistance	83
LOR	Lift Off Resist	96
LPCVD	Low Pressure Chemical Vapor Deposition	97
HDICP	High Density Inductively Coupled Plasma	97
CVD	Chemical Vapor Deposition	97

A MEMS Multi-Cantilever Variable Capacitor On Metamaterial

I. Introduction

1.1 Problem Statement

Ever since Pendry et al. [1] proposed using microstructured split ring resonators (SRR) to create artificial magnetic responses from materials with no inherent magnetic properties, SRRs have become increasingly popular for use as negative magnetic media, also known as metamaterial [2, 3]. An example of an SRR is shown in Figure 1.1. SRRs inhibit a narrow band of electromagnetic waves that lie in the SRRs resonant frequency, provided the electromagnetic waves are polarized along the axis of the SRR [4,5]. However, once fabricated, an SRR has a specific, unalterable resonant frequency due to its geometry.

Past research has focused on SRR metamaterials as passive devices in which the electromagnetic resonance of the structure remains constant. However, tunable SRRs are gaining particular interest for antenna beam steering [5]. Recently, studies have been carried out to answer the demand for a resonant-tuneable metamaterial device. For instance, one study used a varactor diode to electronically tune SRR-based notch filters [4]. Another study used pre-packaged micro-electro-mechanical-systems (MEMS) as switches to create a metamaterial SRR with a dual state electromagnetic response [5].

This paper introduces the novel concept of using a MEMS varactor device located at the gap of a split ring to mechanically alter the capacitance of the SRR structure and thus change its resonance. This design simplifies fabrication because the SRR and MEMS device are both fabricated using micromachining processes. This

design also uses less space than current tuneable SRRs since the MEMS varactor device is fabricated directly on the SRR. Another benefit is that a broad frequency response is available due to the large capacitance ratio of the MEMS varactor.

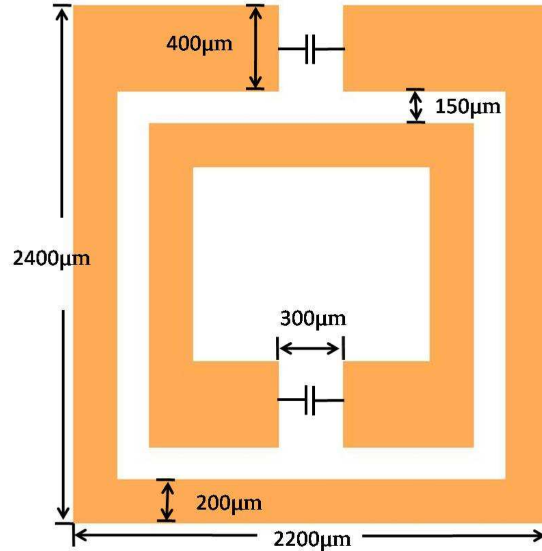

Figure 1.1: Split ring resonator (SRR) unit cell used in this study [6].

1.2 Micro-electro-mechanical Systems

MEMS have been researched and developed since the 1970's. MEMS technology refers to mechanical structures on the order of 1 to 100's of micrometers (μm). Recent advancements in reliability and lifetime issues have increased considerations for their use in many applications. Specifically, MEMS devices are becoming increasingly popular for use in radio frequency (RF) applications. MEMS are ideally suited for use as RF devices because of their many advantages over their solid state counterparts such as [7–11]:

1. Capacitive Switches:

   - high isolation: RF MEMS switches are fabricated with air gaps and therefore have low off-state capacitances in the tenths of fF as shown in Figure 1.2

- low power consumption: MEMS require high voltage ($20 - 80$ V) for electrostatic actuation, but consume a negligible amount of current (leakage current from the on-cycle)
- low insertion loss: typical transmission insertion losses of 0.06 dB/mm at 10 GHz have been reported [9]. Thicker transmission lines also reduce insertion loss when the beam is in the up-state [12] (as shown in Table 1.1)

2. Contact Switches:

- low resistive loss [12] (as shown in Table 1.1): the MEMS switch can be made with high conductivity metal
- high power handling capability [12]: MEMS switches are free of the pn junction breakdown limit
- excellent linearity: MEMS do not have nonlinearities like that in field effect transistors (FET) as shown in Figure 1.2 [13]. A MEMS contact switch is an all-metal structure which behaves like an ideal resistor and is thus not governed by the carrier statistics like that of a FET [14]

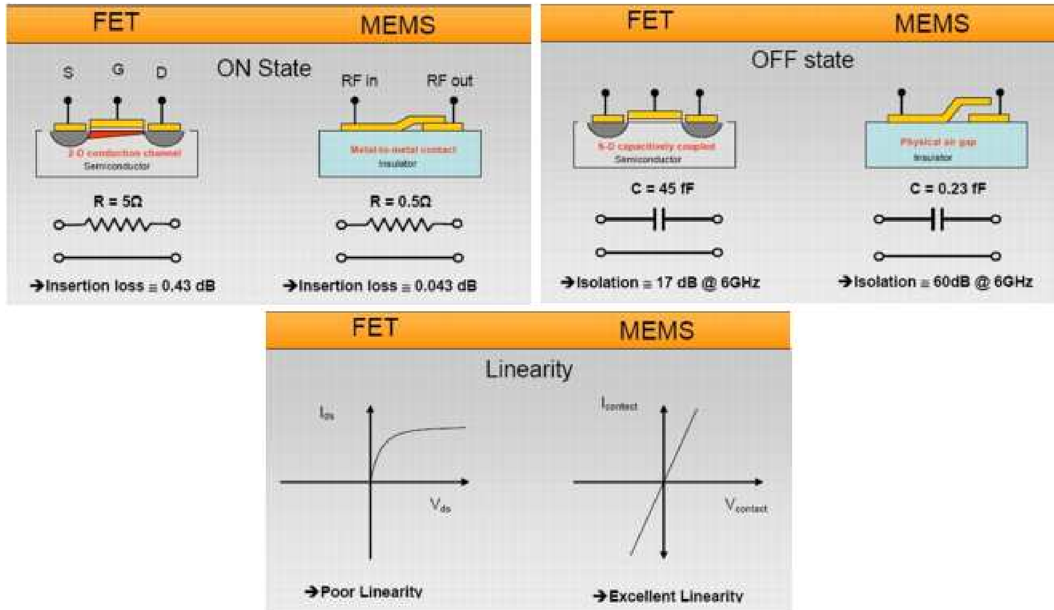

Figure 1.2: FET and MEMS switch comparison [14].

Table 1.1: RF switch technology comparison [14].

Characteristic	MagLatch MEMS	GaAs FET	Pin Diode	EMR (PCB)	Coaxial RF Switch
Size	Very small	Very Small	Very Small	Medium	Large
DC Resistance	<0.5 Ω	1-5 Ω	1-5 Ω	0.1 Ω	0.5 Ω
Carrying Power	3 WCW	0.5 WCW	5 WCW	10 WCW	35 WCW
Breakdown Voltage	Medium	Low	Varies	High	High
Speed	<0.5 msec.	5 nsec.	10-100nsec.	6 msec.	1-40 msec.
Life Cycle	$>10^7$ (cold) $>10^6$ (hot)	infinite	infinite	5×10^6 (cold) 3×10^5 (hot)	$10^5 - 10^6$
Frequency Performance	DC - 6 GHz	< 8 GHz (narrow-band)	< 20GHz (narrow-band)	DC < 6 GHz	< 40 GHz
Insertion Loss (dBmax)	<0.5	2	0.5	0.5	0.1
Isolation (dB min)	>40	28	30	40	80
3rd Order Harmonics	Very Good	Poor	Poor	Very Good	Very Good
Power Consumption (OFF state)	Zero	Low (1-20 mW)	Medium (10mW)	High (0-900 mW)	High (0-700)
Drive Voltage	5V or less	5-8 V	3V, 5 V	3-24 V	12 V, 28 V
Integration Capability	Very Good	Very Good	Very Good	Poor	Very Poor
Est. Retail Cost – SPDT Type	Low	Low (Few $)	Low ($1-$8)	High ($30-$100+)	Very High ($100-$200+)

1.3 Research Objectives

The objectives of this research are to:

1. Design and fabricate MEMS cantilever devices directly on an SRR
2. Characterize fabricated devices (i.e., actuation voltage, release voltage, capacitance, limited lifetime test)
3. Experimentally demonstrate tuning SRR frequency using a MEMS capacitor

1.4 Design Requirements

1. Devices must be fabricated on a dielectric substrate, preferably sapphire (for RF testing purposes)
2. Fabrication techniques must be available at the Air Force Institute of Technology (AFIT) or the Air Force Research Lab/Sensors Directorate (AFRL/RY)

3. Voltage needed to actuate cantilevers must not exceed the dielectric breakdown voltage
4. Beams must actuate one at a time to provide a controllable way to change capacitance
5. Cantilevers should not stick in the down state after actuation voltage is removed
6. Capacitive array should provide enough of a capacitance change to the SRR to observe a shift in resonant frequency ($\approx 1 - 3$ pF per beam)

1.5 Organization of Thesis

This thesis is divided into seven chapters and one appendix. Chapter one details the intent of the research. Chapter two provides a comprehensive literature review on MEMS cantilever and capacitive switches, tunable varactors, metamaterial, SRRs, and MEMS on metamaterials. Chapter three is a review of the mechanical theory of cantilever beams and a brief electromagnetic theory review on SRRs. Chapter four describes the method of device design and fabrication. Chapter five presents an analysis of cantilever mechanical modeling and simulation using analytic equations and a finite element modeling software program, CoventorWare®. Chapter six covers the experiments and test results. Chapter seven discusses overall conclusions from the test results and recommendations for future research. Appendix 1 contains the process followers used for device fabrication.

II. Background

2.1 Chapter Overview

This chapter presents background material pertinent to MEMS contact and capacitive switches. It gives the status of research on variable capacitors using MEMS devices, and it briefly explains metamaterials and split ring resonators.

2.2 Background on Contact and Capacitive Switches

There are many methods available to actuate a MEMS switch, such as electrostatic, electromagnetic, thermal, and piezoelectric; however, electrostatic actuation (used in this design) is the most widely implemented due to its near zero power consumption and simplicity [15]. The following subsections discuss the design, behavior, and reliability of electrostatically actuated contact and capacitive MEMS switches.

2.2.1 Contact Switch. The first major category of RF MEMS switches is the metal-on-metal contact switch, also known as an ohmic or series switch, which opens or closes electronic transmission through mechanical movement [15]. The contact switch in Figure 2.1 is composed of an anchored cantilever beam with contact dimples

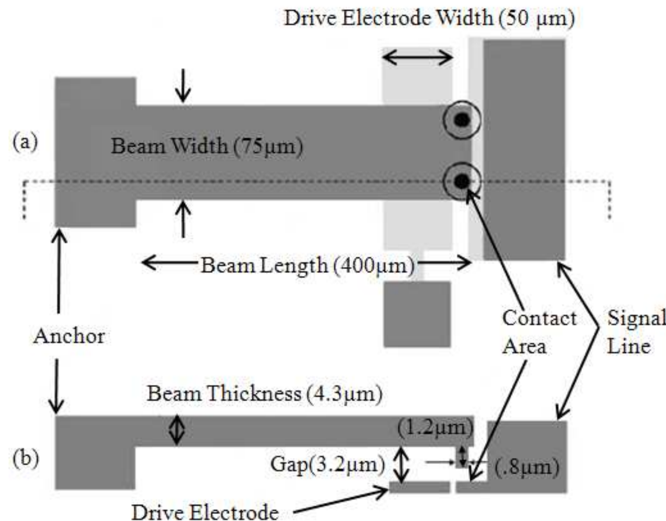

Figure 2.1: Layout (a) and cross section (b) view of a cantilever type contact switch [16].

at its free end, a drive electrode, and a contact area landing pad. A bias voltage (positive or negative) applied between the cantilever beam and the drive electrode operates the device. As the applied bias voltage increases, coulombic force attraction between the beam and electrode causes the free end of the cantilever to bend toward the bottom drive electrode. The dimples at the end of the cantilever land on the contact area, which creates an electrical connection.

2.2.1.1 Electrostatic Actuation. Figure 2.2 is a generic force diagram which models an electrostatic actuator as a parallel plate capacitor. The top plate can be thought of as the cantilever beam, and the bottom plate as the drive electrode from Figure 2.1. The two primary forces acting on the plates are (1) the mechanical restoring force (F_s), which is determined by beam geometry and material, and (2) the electrostatic force (F_e), which is governed by Coulomb's law.

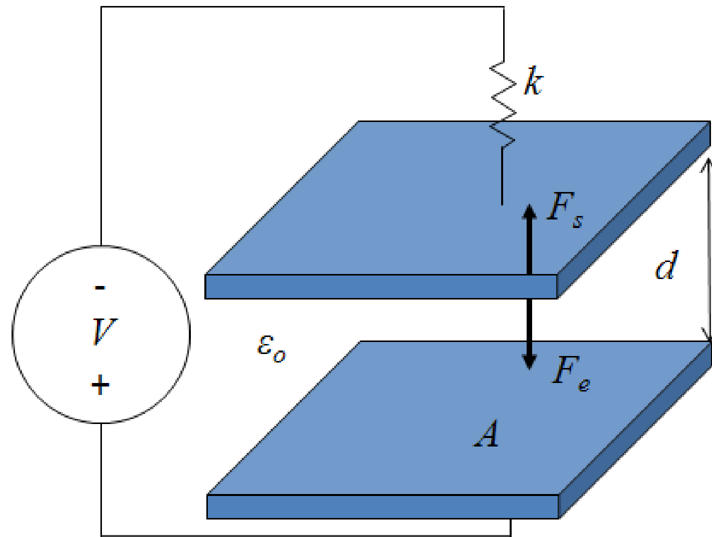

Figure 2.2: Generic force diagram for a parallel plate electrostatic actuation device (cantilever). The mechanical restoring force, F_s, is a function of plate separation, d, and the beam spring constant, k, which is dependent on material properties and device geometry. Electrostatic force, F_e, is a function of: the applied voltage across the parallel plates, the surface area of the plate, A, the permittivity of the dielectric between the plates, ε_0 and ε_r, and the distance between the plates, d [17].

Recall Coulomb's law, which states that like forces repel and opposite forces attract. Coulomb's law is an inverse square law which means that if the distance between two point charges doubles, then the Coulombic force attraction between the two points decrease by a factor of four. (Coulombic forces in MEMS structures are high because the distance between the two point charges is in the micrometer range) The electrostatic force between two parallel plates is given by [18]:

$$F_e = \frac{\varepsilon_0 \varepsilon_r A V^2}{2d^2} \text{ (N)} \tag{2.1}$$

where ε_0 is the permittivity of free space and ε_r is the dielectric constant of the medium separating the two sources, A is the plate area, V is the applied voltage, and d is the distance separating the parallel plates.

When the voltage source in Figure 2.2 is turned on, positive charges collect on the bottom plate and negative charges collect on the top plate. Following Coulomb's law, these opposite charges attract which forms an electrostatic force. Initially, the mechanical restoring force (F_s) resists the plates from moving toward each other. Increasing voltage further causes more charge to accumulate on the plates, which leads to a higher electrostatic force. Eventually, the electrostatic force overcomes the mechanical restoring force of the beam causing the beam to "snap" down onto the contact area as shown in Figure 2.3. The voltage at which the beam snaps down is called the pull-in voltage, (V_{pi}).

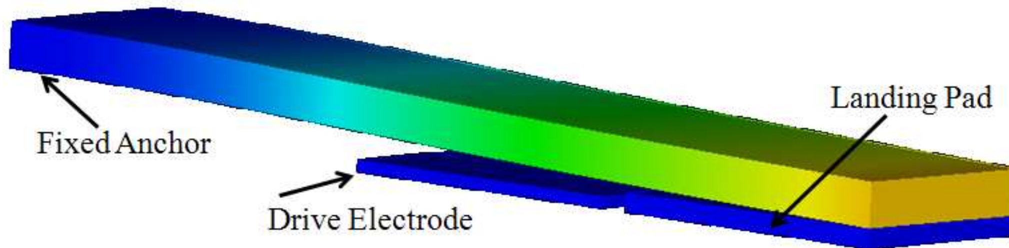

Figure 2.3: Cantilever beam at pull-in voltage. Colors represent magnitude of deflection; blue = no deflection, yellow = 2 μm deflection.

The cantilever snaps down in the tens of micro-seconds and is a function of the electrostatic force exerted on the cantilever [15]. Referring back to Figure 2.1, when the beam pulls into contact with the landing plate (referred to as the down, closed, or on-state) an electrical connection is made, which allows an RF signal to pass through the beam to the signal line. When the voltage applied is less than V_{pi}, the beam does not bend down enough to contact the signal line and the RF signal cannot pass (referred to as the up, open, or off-state). When the applied voltage is removed, the electrostatic force quickly falls to zero and the mechanical restoring force becomes the dominant force and restores the beam back to its original position.

2.2.1.2 Contact Force and Area. When in the down-state, the contact switch creates an electrical connection, however, the switch still introduces a small resistance (less than 3 Ω) to the circuit. Coutu et al. [19] showed that increasing the bias voltage beyond the pull-in voltage increases the contact force between the beam and the contact plate, which decreases contact resistance. Contact force is a compressive force which causes material deformation, therefore, when increased, it compresses the beam and contact plate together creating more surface contact area [19]. Contact area is determined by contact geometry, surface roughness, elastic modulus, and material hardness [19]. An example of a contact switch with surface roughness is shown in Figure 2.4(a). When the two plates come into contact as shown in Figure 2.4(b), the peaks (also known as surface asperities) contact first, therefore the contact surface area is not at its maximum [20]. The surface asperities undergo

(a) (b)

Figure 2.4: Example of surface roughness (a) which leads to a decreased contact area at pull-in (b).

a slight deformation [20] creating small areas of contact (Figure 2.5). Over-biasing the contact switch increases the contact force between two contacting objects, which elastically and plastically deforms surface asperities, thus creating a greater contact surface area.

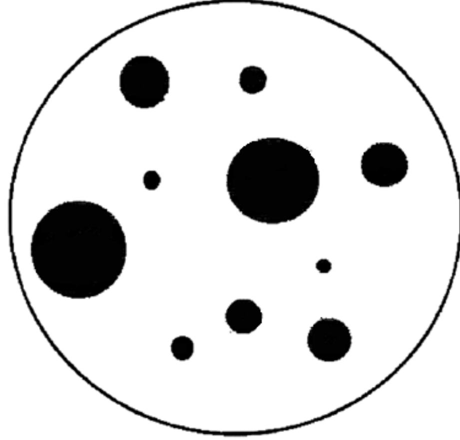

Figure 2.5: Example of contact area (in black) at pull-in voltage [19].

2.2.1.3 Contact Resistance. From Equation 2.2, as contact area increases, the total resistance (R) of the contact switch decreases proportionally [19].

$$R = \frac{\rho L}{A_c} \;\; (\Omega) \tag{2.2}$$

where ρ is resistivity of the material, L is the length, and A_c is the contact area. In Figure 2.6, switch resistance falls dramatically at V_{pi} indicating the switch has pulled-in and made an electrical connection. The slight increase in resistance that occurs directly after pull-in is due to the cantilever bouncing during pull-in, however, the beam quickly settles to form a stable contact [15]. The switch contact resistance then continues to decrease as actuation voltage increases, indicating that contact surface area is increasing.

2.2.1.4 Collapse Voltage. Device engineers desire a minimum amount of switch resistance, however, actuation voltage cannot be increased indefinitely.

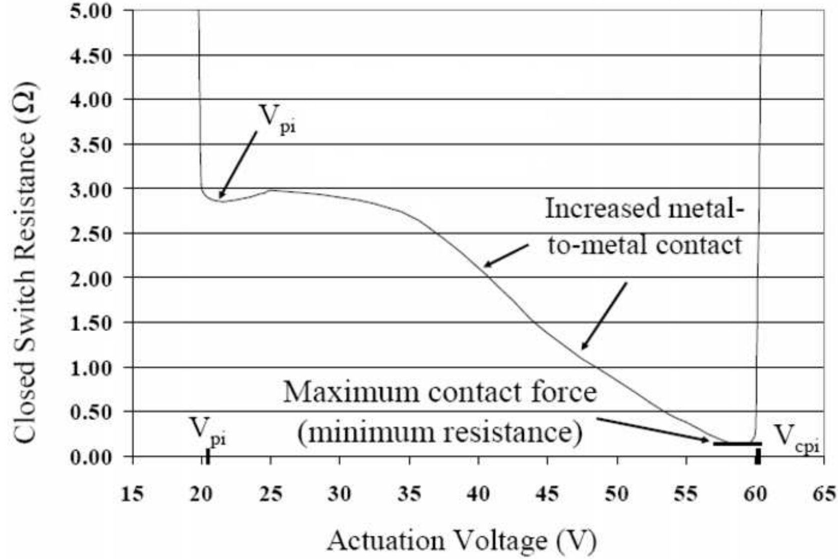

Figure 2.6: Plot of measured closed switch resistance vs. applied actuation voltage. Initial drop in resistance occurs at pull-in voltage and decreases with increasing actuation voltage (indicating an increasing contact area). At collapse voltage, V_{cpi}, the beam makes contact with the drive electrode and shorts the device causing device failure [20].

Eventually, the switch encounters the collapse voltage (V_{cpi}) [21]. As illustrated in Figure 2.7, a cantilever is at collapse voltage when contact is made between the cantilever and the drive electrode. If the drive electrode is not insulated, the device shorts out, causing device failure. Cantilever collapse occurs because coulombic forces continuously attract the beam towards the drive electrode (even after beam pull-in has occurred). As voltage increases, the electrostatic attraction force becomes strong enough to pull the beam down onto the drive electrode. The desired range of actu-

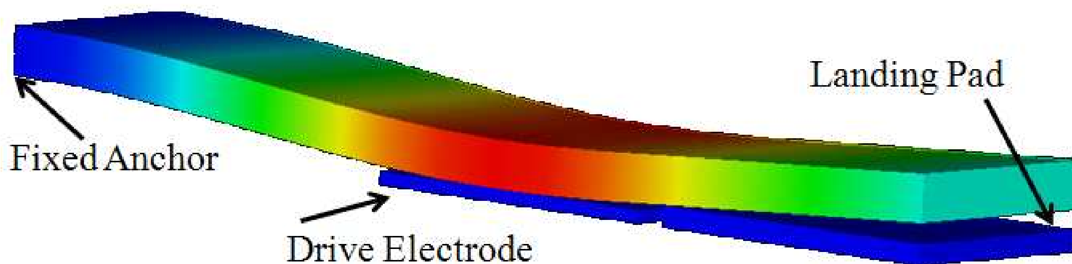

Figure 2.7: Cantilever at collapse voltage. Colors represent magnitude of deflection; blue = no deflection, red = 2.2 μm deflection.

ation voltage is between V_{pi} and V_{cpi}, however, switches operated near V_{cpi} have less contact resistance. An engineering tradeoff must be determined between actuation voltage and resistance because operating close to V_{cpi} also affects the reliability and lifetime of the switch by increasing chances of failure.

Coutu et al. [22] have designed an RF MEMS cantilever switch to prevent a beam from collapsing onto an electrode. In their device shown in Figure 2.8, the electric contacts and actuation electrode are co-located near the beam's end which allows for higher actuation voltages without increasing the chances of collapsing the beam [22].

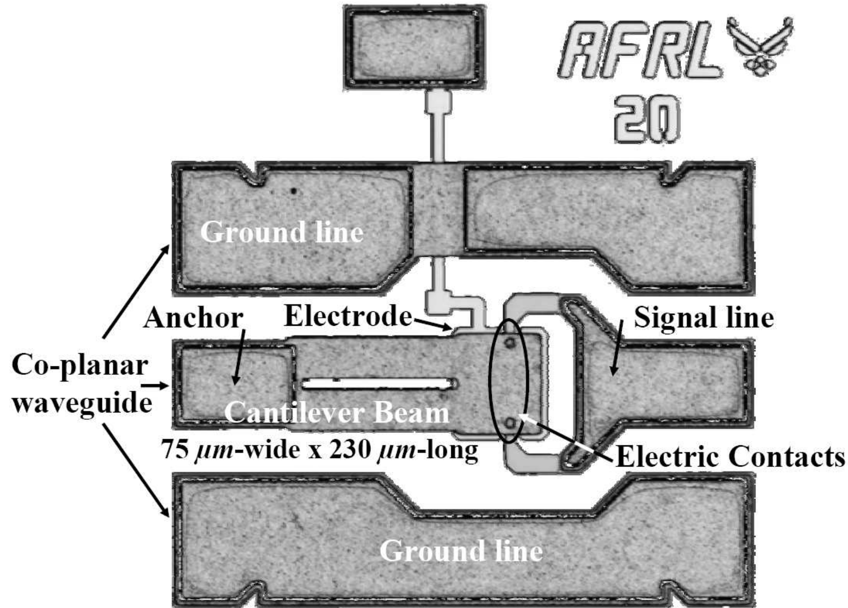

Figure 2.8: RF MEMS switch with electric contacts and actuation electrode co-located near the beam's end to prevent the beam from collapsing [22].

2.2.1.5 Reliability Issues. Device reliability of greater than 10^8 hot-switched switch cycles is a key performance criterion for RF MEMS switches [19]. A hot-switch is defined as voltage potential existing across a contact actuating from open to closed, or a current flowing through a contact actuating from closed to open. Hot-switching may create arcing, which damages contact dimples and reduces device lifetime. The two primary failure mechanisms that dictate MEMS device reliability

are stiction and the degradation of the ohmic contact. The first failure mechanism, stiction, occurs when micromachined parts adhere to each other or to the substrate due to various effects such as capillary forces, van der Waals forces, electrostatic attraction, or hydrogen bonding [19, 23]. Stiction of a device may occur when in use or during the release process. Capillary forces of the liquids in the release process can pull mechanical structures together [23]. Stiction caused during the release process can be mitigated by designing stiffer structures, reducing contact surface area by using dimples, or by using a carbon dioxide (CO_2) critical point dryer to release structures [23]. The second failure mechanism is a degradation of the ohmic contact in which the contact resistance significantly increases with increasing switch cycles [19, 20, 24]. Gold (Au) is typically used for metal-to-metal contacts primarily because of its low resistivity and high-resistance to oxidation. However, Au has a low material hardness factor and is easily eroded through material transfer, which increases contact resistance over time due to a reduced contact area as determined by Equation 2.2 [19]. It has been shown that Au alloyed with harder metals such as palladium (Pd), platinum (Pt), and copper (Cu) increases beam hardness and improves switch reliability with a trade-off of slightly higher contact resistances [19].

2.2.2 Capacitive Switch. Figure 2.9 shows a simple capacitive switch integrated in a coplanar-waveguide (CPW). The metallic membrane (bridge beam) has a high conductivity and stiff mechanical properties. A dielectric insulator covers the transmission line to prevent the control signal from shorting during device actuation. The ends of the beam (posts) are anchored to the CPW ground planes. The beam and transmission line act like a parallel-plate capacitor.

When no voltage is applied to the transmission line, the beam remains in its original up-state position. When a voltage is applied between the transmission line and the beam, positive and negative charges form on the conductor surfaces which induces an electrostatic force on the beam. As the applied voltage between the transmission line and beam increases, the electrostatic force eventually causes the beam to collapse

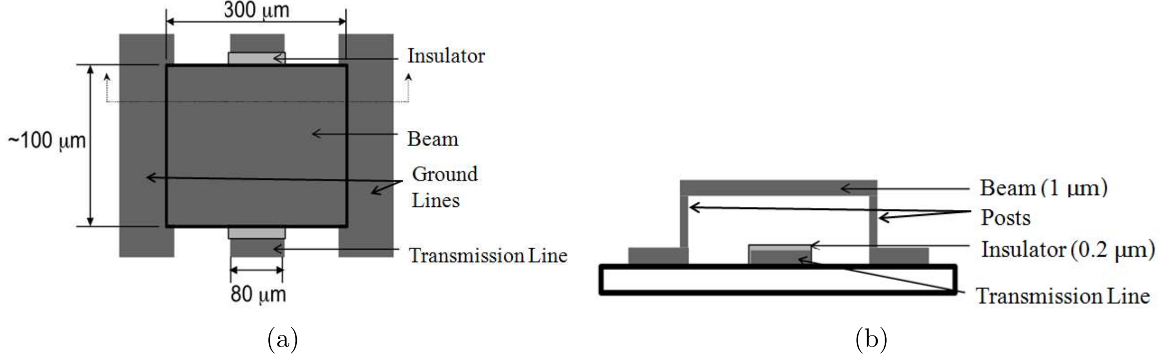

Figure 2.9: A capacitive switch layout (a) and cross section view (b) [25]. Charges on the transmission line pull the beam downwards. When the beam pulls-down on the insulator, a large capacitance exists between the beam and transmission line. At GHz frequencies, the impedance between the transmission line and ground line is low, which forms a reflective switch.

on the dielectric layer, which increases the capacitance by a factor of $30 - 150$ [26]. From Equation 2.3, a switch in the down-state increases switch capacitance ($\approx$ pF), which decreases the reactive impedance (Z_C) between the transmission line and the beam at microwave frequencies, thus creating a reflective switch:

$$Z_C = \frac{1}{j\omega C} \ (\Omega) \tag{2.3}$$

where ω is the frequency, and C is the capacitance provided from the capacitive switch [27].

When the applied voltage is removed, mechanical restoring forces return the beam to its original position. In the up position, the capacitance between the beam and transmission line is negligible ($\approx$ fF), which causes the impedance between the transmission line and beam to increase by multiple orders of magnitude. To the circuit, the high impedance is essentially an open, thus any signal travelling on the transmission line passes with little reflective loss to the ground lines.

2.2.2.1 Capacitance. A parallel plate capacitor model is shown in Figure 2.10. The capacitance between the two plates in the up-state (Figure 2.10(a)) is given by [7, 26]:

$$C_{pp} = \frac{\varepsilon_0 A}{d + \frac{t_d}{\varepsilon_r}} \quad \text{(fF)} \tag{2.4}$$

where t_d is the thickness of the dielectric layer. The total capacitance is actually higher than C_{pp} because of the fringing effect [26]. The total up-state capacitance is calculated using:

$$C_{up} = C_{pp}(1 + P_f) \quad \text{(fF)} \tag{2.5}$$

where P_f is the fringing field contribution of approximately 25 percent [26].

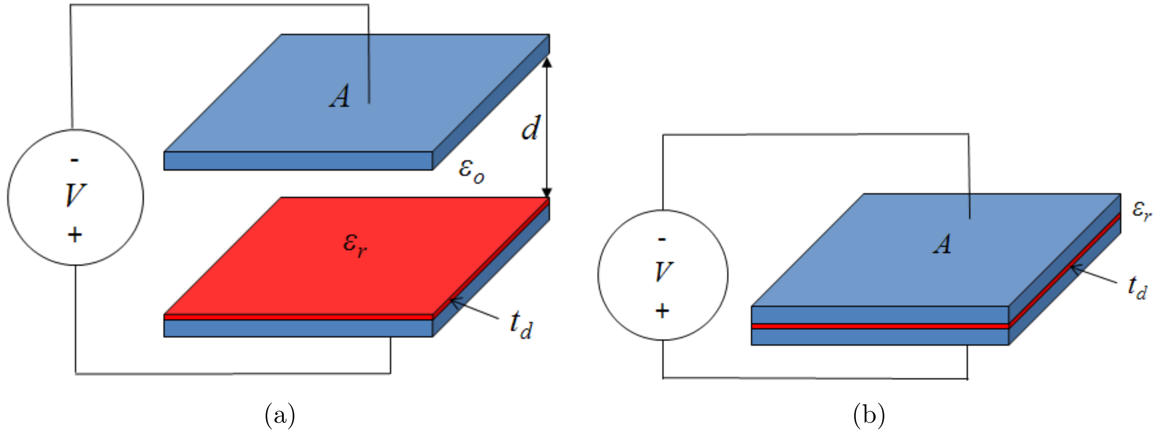

Figure 2.10: Parallel plate capacitor model in the up-state (a) and down-state (b).

Assuming a perfectly flat contact area, the capacitance in the down-state position (Figure 2.10(b)) is expressed as [7]:

$$C_d = \frac{\varepsilon_0 \varepsilon_r A}{t_d} \quad \text{(pF)} \tag{2.6}$$

However, C_d is expected to drop due to dielectric roughness, residue left after release etches, or contaminants—all of which cause poor contact between the moveable

beam and dielectric layer [12, 26, 28]. Lakshminarayanan et al. [26] report a reduction of calculated down-state capacitance (Equation 2.6) by 46 percent due to dielectric surface roughness.

2.2.2.2 Dielectric Surface Roughness. Device engineers desire that capacitive switches have a high off-state/on-state capacitance ratio, therefore, the down state capacitance must be as high as possible. The surface roughness of the dielectric film has a significant effect on the down-state capacitance. A rough dielectric surface creates parasitic air gaps as shown in Figure 2.11 and significantly lowers the down-state capacitance [29]. The dielectric film must be as smooth as possible such that when the cantilever beam pulls-down, the contact area between the dielectric film and metal beam is maximized [13]. The process used to deposit the dielectric film has a significant effect on surface roughness. Also, increasing actuation voltage deforms Au bridge beam asperities (silicon nitride (Si_3N_4) has a higher hardness factor than Au) to create a larger capacitance area (analogous to reducing resistance in a contact switch by increasing voltage).

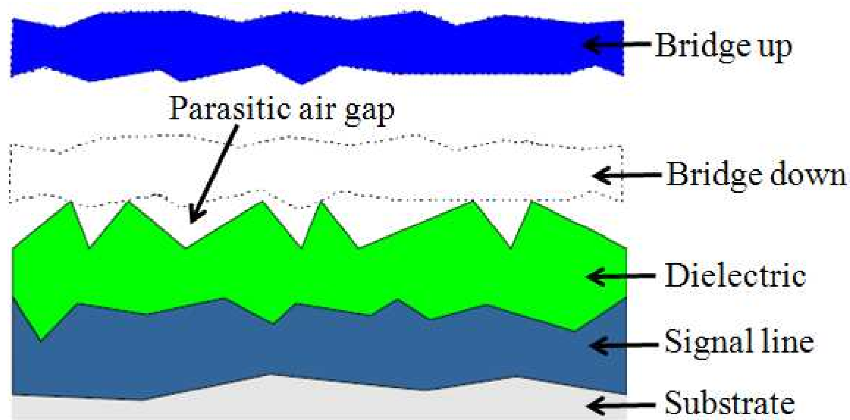

Figure 2.11: Dielectric surface roughness with parasitic air gaps that decrease the overall down-state switch capacitance by reducing surface contact area [29].

2.2.2.3 Microwave Power Effects. When a microwave frequency signal travels through a MEMS switch, it must be taken into account that microwave power affects MEMS switch operation [30]. The relaxation time of free electrons in Au is

0.29×10^{-15} sec which means the electrostatic force instantaneously follows the RF electromagnetic field [31]. Therefore, the average voltage of the rectified RF sine wave attracts the switch [31]. This can lead to two types of RF power failure mechanisms: RF latching and RF self-actuation [32]. RF latching occurs when the applied RF power is enough to keep the membrane switch held down even after DC bias has been removed. RF self-actuation occurs when the RF power is high enough to actuate (pull-down) the membrane without applying a DC bias [32]. However, for both cases of failure, when RF power is removed or reduced from the switch, the device returns to its original position (no longer in a failure mode). Pillans et al. [32] also show in Figure 2.12 that as RF power increases, the pull-down voltage decreases.

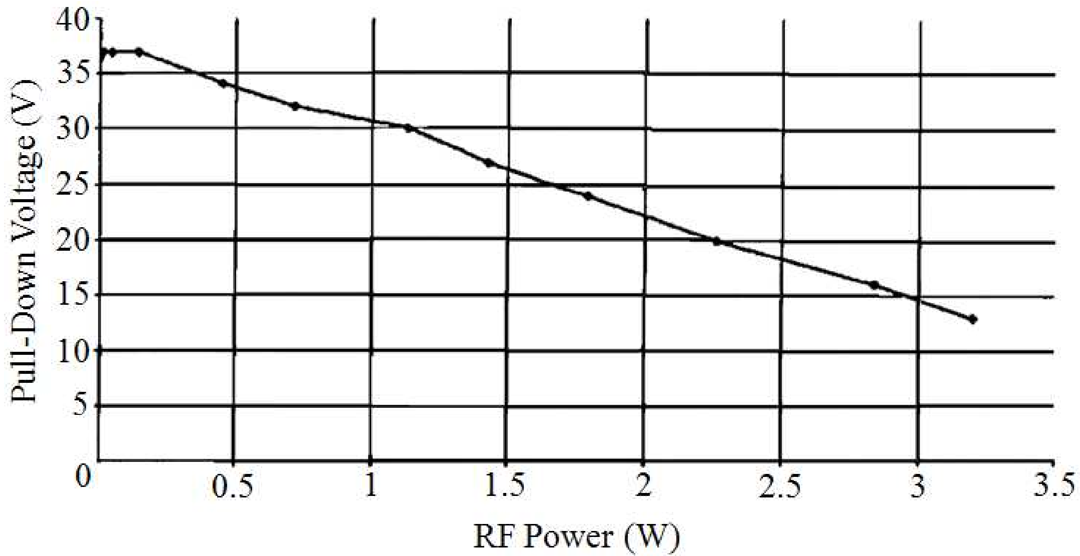

Figure 2.12: Applied RF power vs. DC pull-down voltage [32].

According to Reid et al. [30], RF power also induces a current in the beam bridge which creates ohmic heating that in turn lowers pull-in voltage. Beam temperature and beam pull-in voltage are related to microwave power and frequency as shown in Figure 2.13.

2.2.2.4 Reliability Issues. The main cause of low reliability in capacitive MEMS switches is due to stiction induced by dielectric charging [26, 33, 34]. When the beam collapses on the dielectric, the electric field across the dielectric is

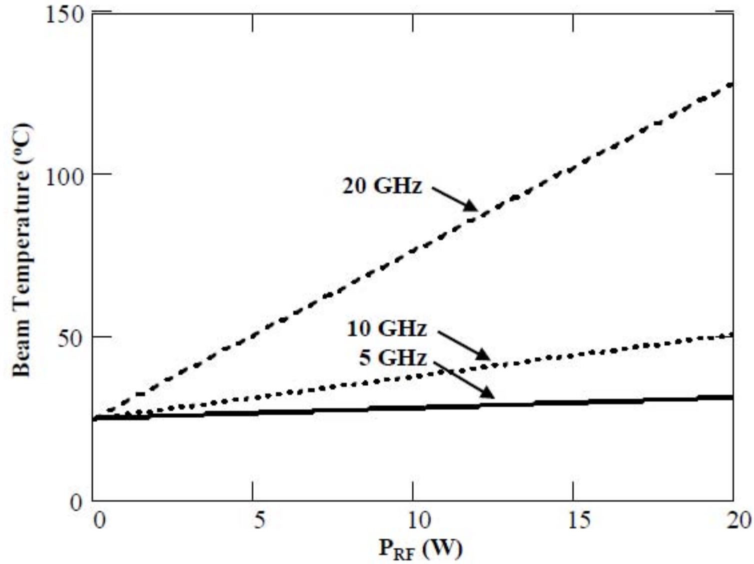

Figure 2.13: Calculated temperature vs. power at different frequencies for a capacitive switch [30].

in the MV/cm range [24, 35]. The high electric field causes charges to tunnel into the dielectric similar to Frenkel-Poole emissions [7,24,36]. The dielectric accumulates charge due to its high density of traps associated with dangling bonds and surface defects [35]. The charge then becomes trapped within the dielectric because there are no convenient conduction paths for the charge to escape [24] (recombination time for these charges can be on the order of seconds to days [7,35]). Trapped charge continues to accumulate in the dielectric as the switch cycles on and off. This trapped charge counteracts (screens) the applied voltage used to actuate or release the switch [24]. Figure 2.14 shows how trapped charge shifts the pull-in and release voltages. As the switch actuates over time, the electric field of the trapped charge becomes strong enough to keep the beam stuck in the down position. Since the hold-down voltage is much less than the actuation voltage (explained in next section), stiction occurs quickly [7, 24].

Contaminants (hydrocarbons and particulates), humidity, and temperature also affect switch lifetime [25]. Contaminants and humidity change the adhesion force between the beam and dielectric. Temperature changes the stress in the beam which

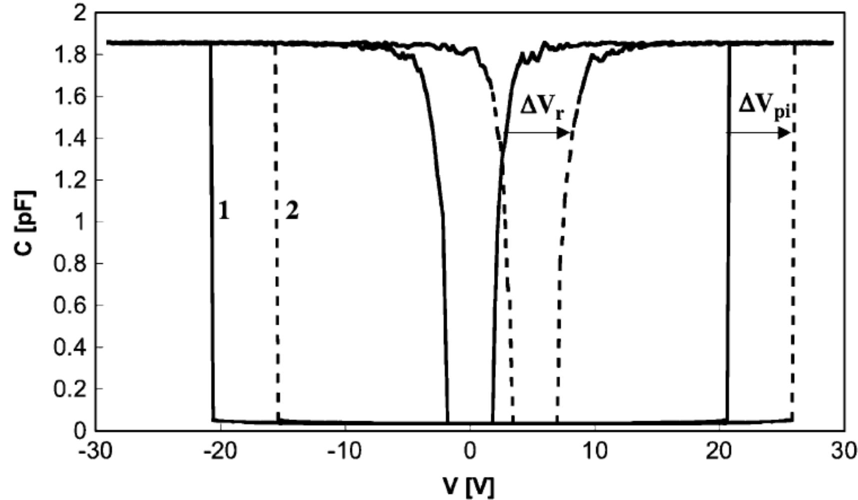

Figure 2.14: Capacitance-Voltage (C–V) relationship of a capacitive switch. Curve 1 represents a switch actuated for the first time and thus has little to no trapped charge. Curve 2 represents the same switch that has been actuated numerous times. Therefore, there is a +5 V shift in pull-in voltage, V_{pi}, and release voltage, V_r, due to trapped charges in the dielectric that have accumulated over time [25, 34].

changes the pull-in and release voltages [24, 30, 37]. Yuan et al. [35] also report that increasing temperature increases trap densities, which shifts actuation voltage and softens the dielectric membrane, making it more prone to stiction.

Mechanical failures are currently of little interest since they do not occur until switch lifetime reaches on the order of 100 billion cycles, which is beyond the failures due to device stiction [28].

2.2.3 Designs Increasing Lifetime. Goldsmith et al. [24] demonstrate that the switch lifetime is directly related to the applied voltage because of dielectric charging effects. In their experimentation, they used a dual-pulse square waveform where the first pulse was applied to pull down the beam and the second pulse was then applied at a lower voltage to keep the beam down. A beam in the down-state requires a lower hold-down voltage because the distance between charges is negligible [7] (recall Equation 2.1; a smaller distance creates a greater force). Switching to a lower holding voltage decreases the amount of time that a high voltage is applied to the electrode dielectric, and thus minimizes the amount of charge tunnelling into the dielectric; this

reduces stiction caused by dielectric charging. Yuan et al. [35] report using the dual pulse method minimizes dielectric charging due to its exponential voltage dependence. Goldsmith et al. [24] also report of an exponential relationship between applied voltage and switch lifetime. In their studies, lifetime improved by a factor of ten for every $5-7$ V decrease in actuation voltage.

The bipolar actuation waveform is another actuation technique used to reduce stiction. In bipolar actuation, the initial applied voltage actuates the switch. When the switch is pulled down, charge tunnels into the dielectric film. Voltage is then released followed by applying the next actuation voltage, but at the opposite polarity, which discharges the trapped charge in the dielectric [33]. This method keeps the trapped charge at a minimal level, thus decreasing stiction. The bipolar actuation method, however, is not completely free from stiction because the charging and discharging speeds are not the same for positive and negative voltages [33]. To correct this, Yamazaki et al. [33] have developed an intelligent bipolar actuation (IBA) method, as shown in Figure 2.15, to fix the imbalance between positive and negative charging and discharging speeds. They have developed a software algorithm that detects the amount of release voltage shift (ΔV_r) after every actuation cycle. If ΔV_r is higher than a threshold voltage (V_{th}), then the polarity of the next actuation voltage is reversed. Using the IBA method, Yamazaki and his team were able to free the switch from electrostatic stiction [33].

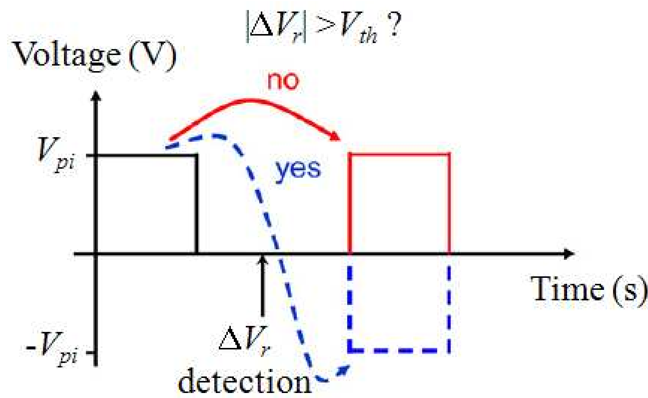

Figure 2.15: Waveform of IBA method [33].

Lakshminarayanan et al. [26] mitigated dielectric charging and temperature effects by changing device geometry rather than by adjusting the actuation method. They designed a miniature MEMS capacitive switch approximately 150 times smaller in lateral dimensions than a standard MEMS device [26]. The miniature MEMS device has a significantly higher mechanical restoring force than a standard MEMS device [26]. The miniaturization, however, results in a reduced capacitance ratio. Device reliability was found to be in the billions of cycles, which makes miniature MEMS more reliable than standard MEMS switch capacitors [26].

2.2.4 Varactors. MEMS are increasingly being used as variable capacitors (varactors) in microwave circuit applications because of their low power consumption, low insertion loss, and inherent tunability. Varactors are designed to have a broad capacitive tuning ratio, a high quality factor, and stiction immunity. Simple bridge or cantilever beams have a very narrow range of stable motion (1/3 the gap) and can only obtain a *continuous* tuning range of 1 : 1.5 before deflection instability occurs and the beam pulls-in [7, 28]. However, there are many capacitive MEMS device designs that allow a far greater tuning range than the simple beam structure switch.

Fang et al. [38] used simple MEMS technology to fabricate a low-voltage-controlled variable capacitor as shown in Figure 2.16. The parallel plate capacitor has a high quality factor and a simple design, however, considering the large surface area used, the tuning ratio for capacitance was minimal at 1 : 1.31.

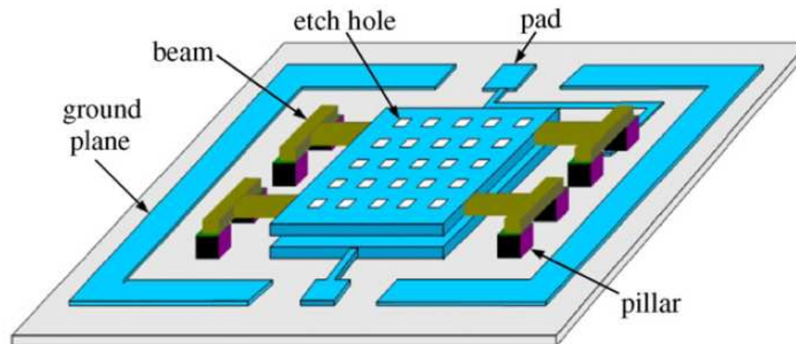

Figure 2.16: Simple parallel plate variable capacitor with a low tuning range [38].

Bakri-Kassem and Mansour [39] have developed a parallel-plate variable capacitor with carrier beams between the plates to increase the tuning range as shown in Figure 2.17. In this capacitor design, the movable plate pulls-in at V_{pi}, but the carrier beams prevent it from collapsing onto the fixed plate electrode. The carrier beams situated between the plates are designed with a high spring constant which prevents the top movable plate from collapsing onto the fixed plate. As the DC bias increases beyond the pull-in voltage, electrostatic forces draw the movable plate downwards, however, the carrier beams slightly bend down with the movable plate, still preventing it from pulling-in. Bakri-Kassem and Mansour's varactor has a quality factor of 14.6 at 1 GHz and is capable of an off/on capacitance ratio of 1 : 5.1 (410 percent tuning range) before pull-in (to the fixed plate). Their design also avoids stiction issues because the movable plate never fully collapses onto the fixed plate.

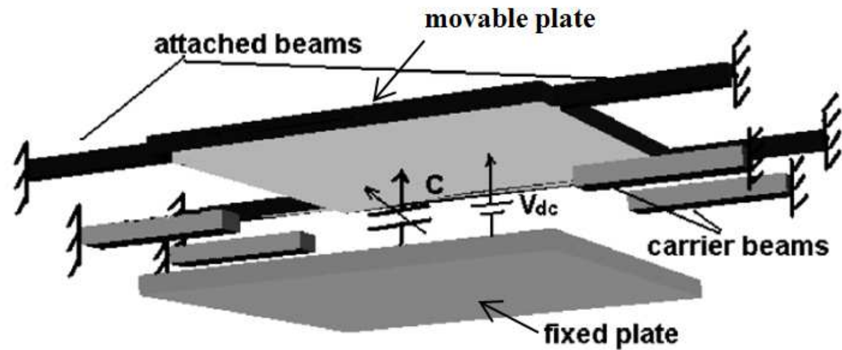

Figure 2.17: A parallel-plate variable capacitor with carrier beams. The movable plate collapses onto the carrier beams at pull-in voltage. The carrier beams bend with the movable plate with increasing voltage, which provides a controllable capacitive tuning range [39].

Luo et al. [40] used multiple beams as shown in Figure 2.18 to create a variable capacitor. Their devices consist of multiple cantilevers and bridges (with lengths ranging from 75 μm to 200 μm in 5 μm increments) that are suspended over an electrode. A dielectric layer is coated over the electrode, which forms a capacitive switch. Luo et al. [40] used three different dielectrics to achieve different capacitance ratios: silicon dioxide (SiO_2), silicon nitride (Si_3N_4), and hafnium dioxide (HfO_2) with dielectric constants of 3.8, 7.8, and 20, respectively (recall Equation 2.6, where

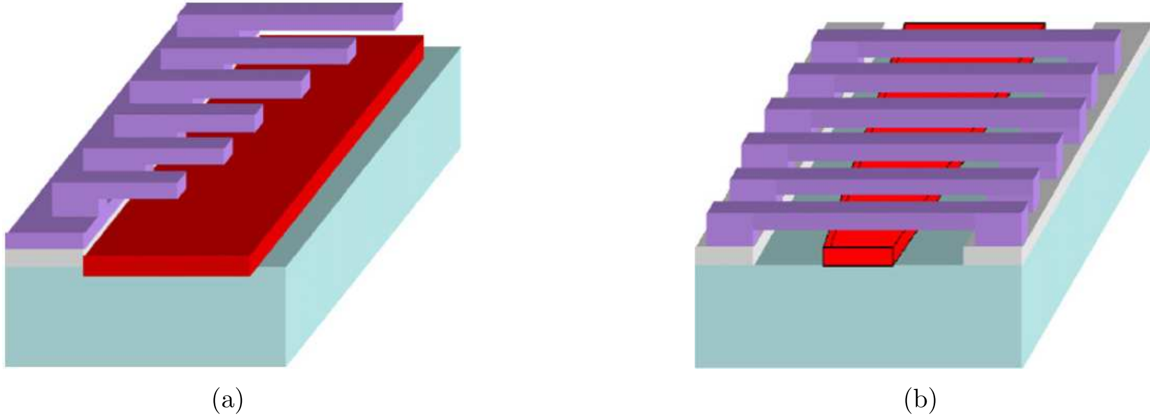

(a) (b)

Figure 2.18: Two types of variable capacitors. The varying length cantilevers (a) pull-in longest-to-shortest. The bridge beam over the longest bottom electrode (b) pulls-in first, followed by the bridge over the next longest electrode [40].

increasing the dielectric constant increases the down-state capacitance). As the bias voltage applied to the electrode increases, the cantilever and bridge beams pull-in one-by-one (longest-to-shortest) thus realizing a step increase in capacitance as shown in Figure 2.19 [40].

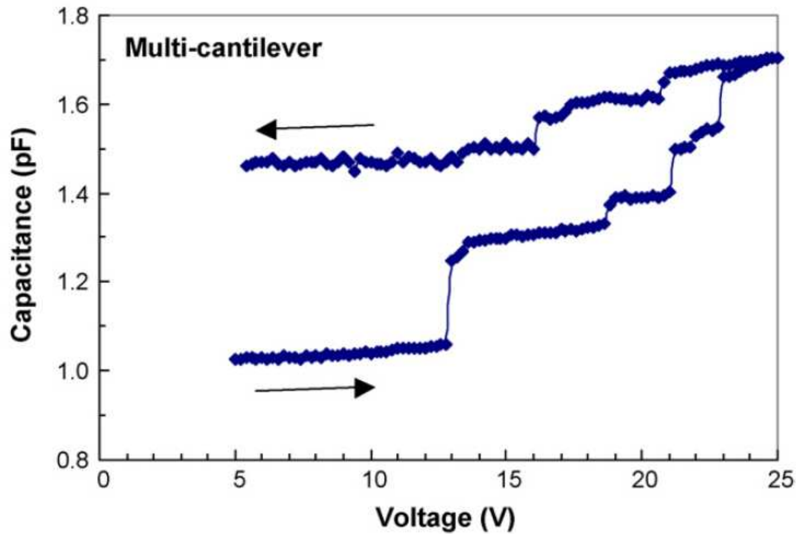

Figure 2.19: C–V characteristic of a multi-cantilever capacitor. The zipper effect is observed where the capacitance increases between 5 and 13 V even though no additional cantilevers have been pulled-down. The large step increase in capacitance at 13 V is due to three cantilevers being pulled-in at once. Also shown, is that capacitance does not return to its original value after actuation voltage has been released, which corresponds to cantilever stiction [40].

Referring to Figure 2.19, at 13 V, a sharp increase in capacitance occurs which represents a cantilever pulling-in. Luo et al. [40] report that the first increase in capacitance is too large for only one cantilever pulling-in, and is in fact the result of three beams pulling-in at once. Luo et al. [40] also show that capacitance still increases with voltage when no cantilevers are pulling-in (between $5 - 13$ V, $14 - 19$ V, etc.). This behavior is believed to be caused by the "zipping effect," [26] where the cantilever lands at an angle shown in Figure 2.20(a), thus the tip contacts the dielectric first while the rest of the cantilever pulls-in (zipper-like) with increasing voltage (Figure 2.20(b)) [40]. The added contact area caused by the zipper effect (Figure 2.20(b)) increases the capacitance contributed by each cantilever.

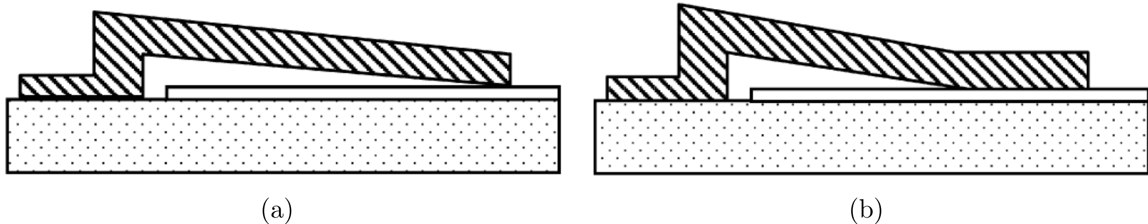

(a) (b)

Figure 2.20: Cantilever collapsing tip first (a) results in a small contact area that creates a small capacitive change. As voltage is increased, more of the beam pulls-in (b), thus creating a "zipper effect". The extra contact area increases capacitance [40].

Figure 2.19 also shows the C–V characteristics as voltage ramps down, however, only two decreasing steps in capacitance occur. Luo et al. [40] report that many of the cantilevers remained stuck to the dielectric layer after voltage had been removed—most likely caused by charge injection into the insulator [40].

2.3 Metamaterials

For this work, a metamaterial is described as a class of ordered microcomposites that exhibit electromagnetic material properties. A unique definition for metamaterials does not exist, however, there are essential aspects common in the many metamaterial definitions such as [41–44]:

- metamaterial properties are not observed in the constituent materials

- metamaterial properties are not observed in nature
- metamaterials are comprised of a periodic structure
- the metamaterial structure has lattice constants that are much smaller than the wavelength of the incident radiation

The first point compares the constituents with those of the whole. The metamaterial is comprised of lower-level components. "Only the co-existence of homogeneous materials with well-defined response properties causes new properties to appear on the next, higher level" [41].

The second point is that metamaterial properties are not found in naturally formed substances; they are man-made (this is a loose and inclusive definition since engineered objects are all non-natural).

The third point is an aspect that some definitions do not require [41]. This thesis uses a periodic metallic SRR structure (discrete "particles") that simulates a homogeneous material whose specific properties are not naturally occurring.

The fourth point is an important aspect because the global response (bulk effect) of the metamaterial is a function of the size of the scattering particles and their neighboring distances [41, 42]. The lattice constant of an SRR unit cell, a, must be smaller than the operating wavelength as shown in the following expression [42]:

$$0.01 < \frac{a}{\lambda} < 0.2 \tag{2.7}$$

This research focuses on metamaterials operating greater than 10 GHz. The wavelength at 10 GHz is 3 cm, therefore, lattice constants are no larger than 6 mm.

2.4 Split Ring Resonators

Artificial magnetics, such as SRRs, are classified as metamaterials. Even though they are non-magnetic, SRR particles possess magnetoelectric coupling, meaning that external electric fields induce electric and magnetic responses in the SRR particle [45,

46]. SRRs are sub-wavelength resonators that inhibit propagation of a narrow band of electromagnetic waves that lie in the vicinity of the SRRs resonant frequency, provided that the electromagnetic waves are polarized along the y-axis of the SRR [4, 5, 45] as shown in Figure 2.21.

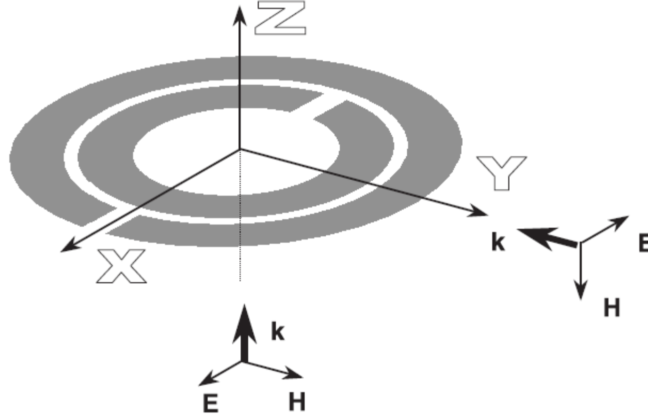

Figure 2.21: Simple SRR with axes labelled. Electromagnetic waves polarized along the y-axis prompt a magnetic response from the SRR [45].

Once fabricated, the SRR has a certain resonant frequency due to its fixed geometry. Resonant frequency of an SRR is given by [5, 47]:

$$\omega_0 = \frac{1}{\sqrt{LC}} \quad \left(\frac{\text{rad}}{\text{sec}}\right) \tag{2.8}$$

where L is the self inductance of the metal trace and C is the capacitance of the split ring. Past research has focused on SRR metamaterials as passive devices in which the electromagnetic resonance of the structure remains constant due to unalterable device geometry. Recently, studies have shown that it is possible to control the effective electromagnetic parameters of a metamaterial structure by using external tuning devices [5].

2.4.1 Capacitor Loaded SRRs. Aydin and Ozbay conducted studies that show SRRs loaded with capacitors at different locations on the split ring produce different frequency responses [2]. Their experiment (Figure 2.22) consisted of fabri-

cating SRRs on FR4 printed circuit board substrate and then mounting capacitors with various capacitance values in three different regions on the SRR structure.

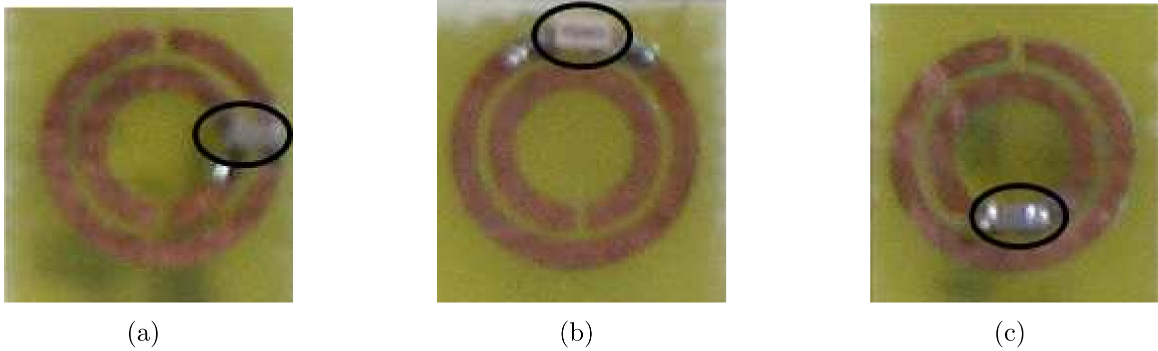

(a) (b) (c)

Figure 2.22: SRR with capacitor loaded between rings (a), across the outer ring gap (b), and across the inner ring gap (c) [2]. Capacitors (circled) at different locations on the SRR induce different frequency responses.

A schematic of Aydin's and Ozbay's SRR unit cell is shown in Figure 2.23(a). Two monopole antennas created from microwave coaxial cable with a length on the order of $\lambda/2$ were used for electromagnetic (EM) detection. Figure 2.23(b) shows a photograph of the experimental setup used for measuring transmission coefficients.

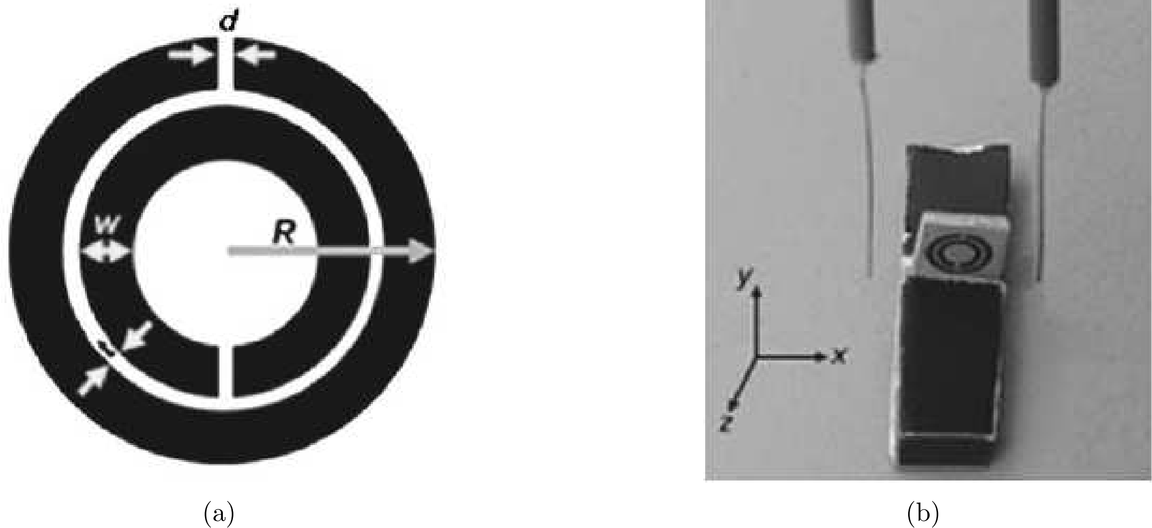

(a) (b)

Figure 2.23: Schematic of SRR with dimensions d = 200 μm and t = 200 μm, w = 900 μm, and R = 3.6 mm (a), and a photograph of experimental setup using two monopole antennas for measuring transmission coefficients of a unit cell SRR (b) [2].

The experimental results (Figure 2.24) show that as capacitance increases, the resonant frequency decreases.

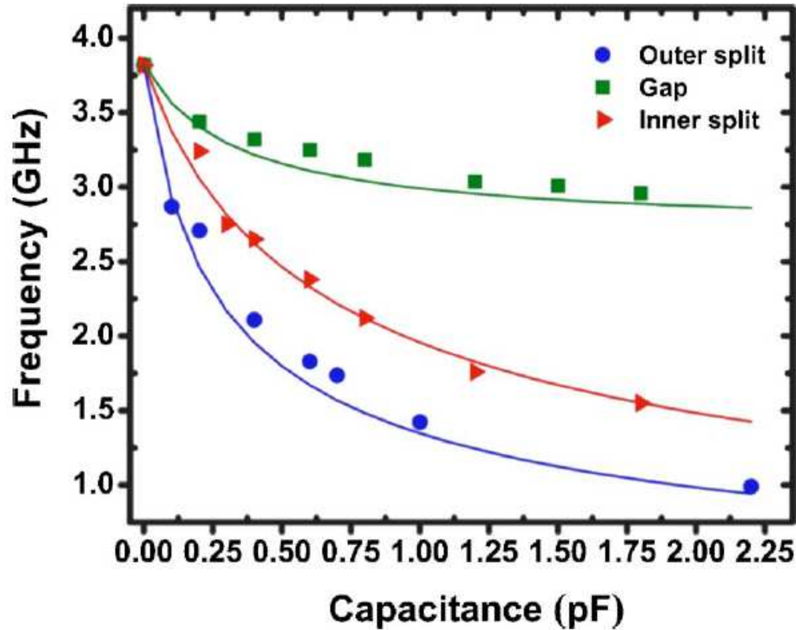

Figure 2.24: Magnetic resonance frequency of an SRR as a function of loaded capacitances at different capacitive regions. Results from numerical models (solid lines) agree with experimental data (data points). A variable capacitor located at the outer split provides the largest tuning ratio [2].

Figure 2.24 also shows that capacitors located on the outer ring have the highest change in resonant frequency vs. change in capacitance, which agrees with the simulated field intensity at magnetic resonance shown in Figure 2.25. From Figure 2.25, it is clear that the electric field intensity is greatest at the outer ring split region, followed by the inner ring split region, and lowest in the gap between the outer and inner rings. Therefore, loading capacitors at the outer split region achieves the highest amount of tuning [2].

In summary, Aydin and Ozbay have shown that it is possible to change the effective permeability values of an SRR particle using external capacitive devices. They also proved that capacitor location has a strong influence on the tuning ratio of SRRs.

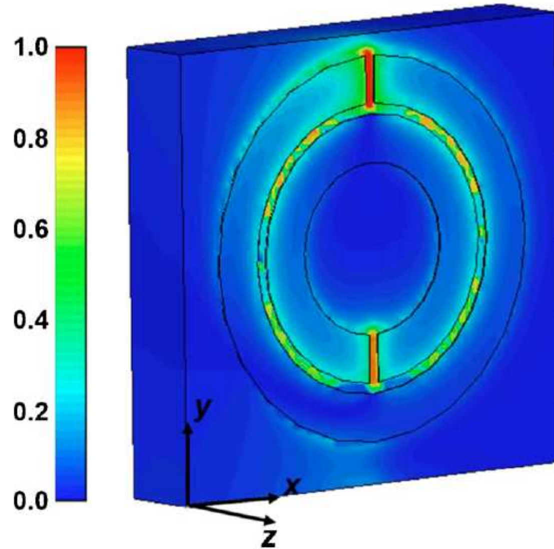

Figure 2.25: Simulated electric field intensity profile at the magnetic resonance frequency of the SRR. Note the highest intensity is between the outer ring gap, followed by the inner ring gap, and then between the two rings. This simulation agrees with the measured data shown in Figure 2.24 [2].

2.4.2 Tunable SRRs. Gil et al. [4] have developed a varactor-loaded split ring resonator (VLSRR) as shown in Figure 2.26 to tune a notch filter at microwave frequencies. The resonant frequency of the VLSRR is controlled by changing capacitance with a varactor diode located between the concentric split rings [4]. The varactor device, however, is larger than the SRR unit cell and thus requires a large surface area as shown in Figure 2.27.

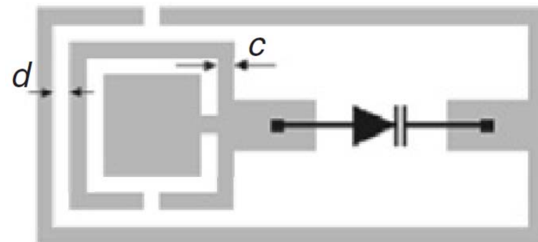

Figure 2.26: VLSRR with a diode varactor between internal and external split rings where d is the ring separation (200 μm) and c is the ring width (200 μm) [4].

The device is fabricated on Rogers RO3010 with a dielectric constant of 10.2. The silicon tuning diodes have a capacitance range of $0.75 - 9$ pF at $28 - 1$ V re-

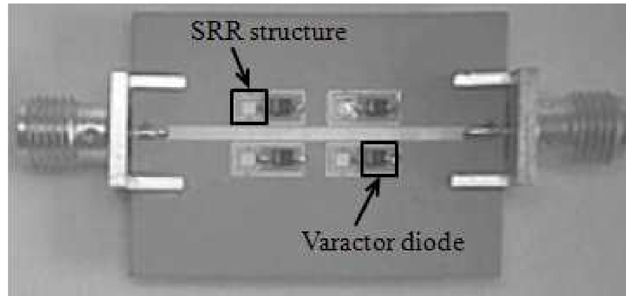

Figure 2.27: Photograph of fabricated SRR with varactor diode. The size of the varactor diode uses nearly the same surface area as the SRR structure [4].

verse bias, respectively. This capacitance range dominates over the original SRR capacitance (without varactors in-place) [4]. Figure 2.28 displays measured transmission coefficients for a VLSRR at different bias voltages. As capacitance of the SRR structure increases, the resonant frequency shifts to a lower frequency.

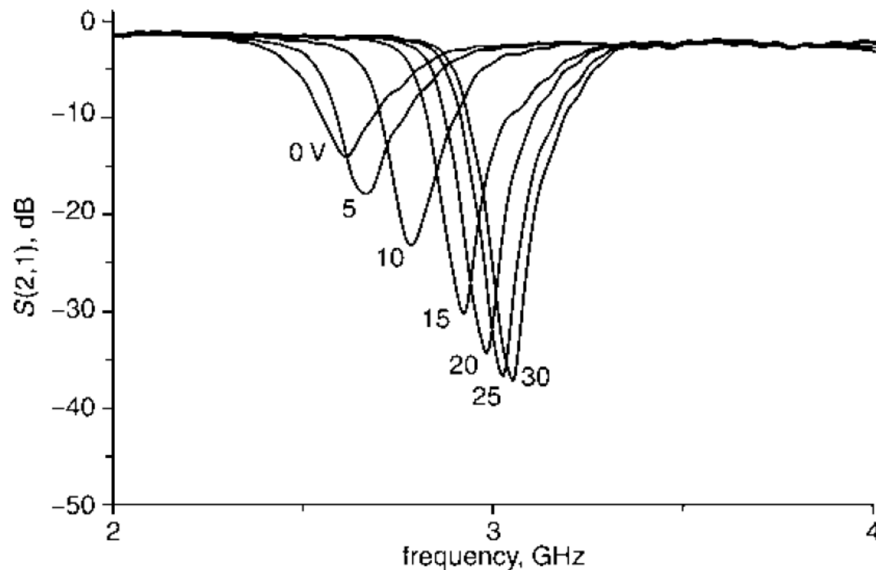

Figure 2.28: VLSRR resonance behavior under different bias conditions. The resonant frequency shifts to the left as capacitance is increased [4].

Shadrivov et al. [48] created a tunable SRR using a variable capacitance diode similar to Gil et al., however, the variable capacitor was placed between the outer split rather than between the concentric rings. Using the device shown in Figure 2.29, Shadrivov et al. [48] were able to tune the resonant frequency of the SRR particle from 2.27 − 2.9 GHz—a tuning range of approximately 26 percent.

Figure 2.29: Varactor-loaded SRR system along with circuitry used for voltage biasing [48].

2.4.3 Tuning SRRs using MEMS. Hand and Cummer developed a dual-state tunable metamaterial element using a TeraVicta RF MEMS switch to control the effective capacitance of an SRR [5]. In their design, the TeraVicta switch is used in the single-pole, single-throw configuration and operates from DC to 7 GHz, and actuates at 68 V_{dc}. The switch can be placed in either a series or parallel configuration with the SRR structure. When the switch is placed in series, it introduces a capacitance when in the open-state, thus shifting the resonance of the SRR as shown in Figure 2.30.

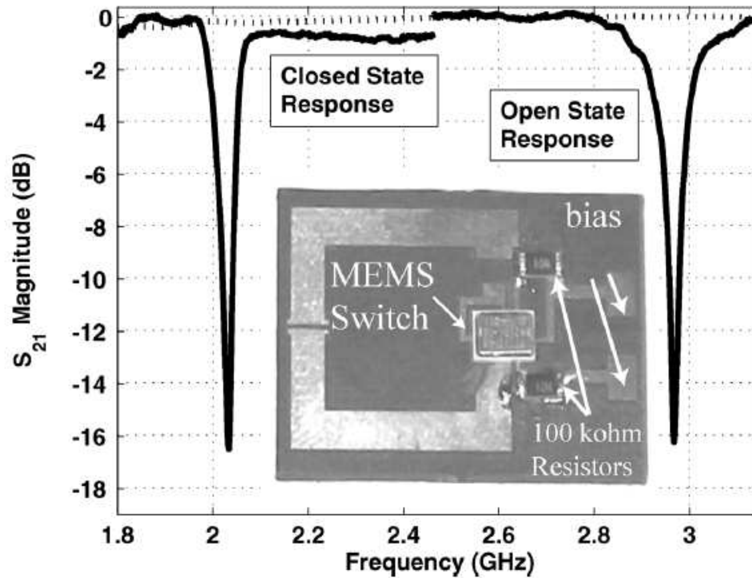

Figure 2.30: Open and closed switch responses for an SRR with a MEMS switch placed in series with the SRR. When the switch is opened, it introduces a capacitive element, which shifts the resonant frequency higher, thus creating a dual-state resonance. The 100 kΩ resistors are used for isolating the DC voltage source [5].

When placed in parallel with the SRR, the switch in the closed-state shorts out the SRR, which eliminates the SRR resonance as shown in Figure 2.31.

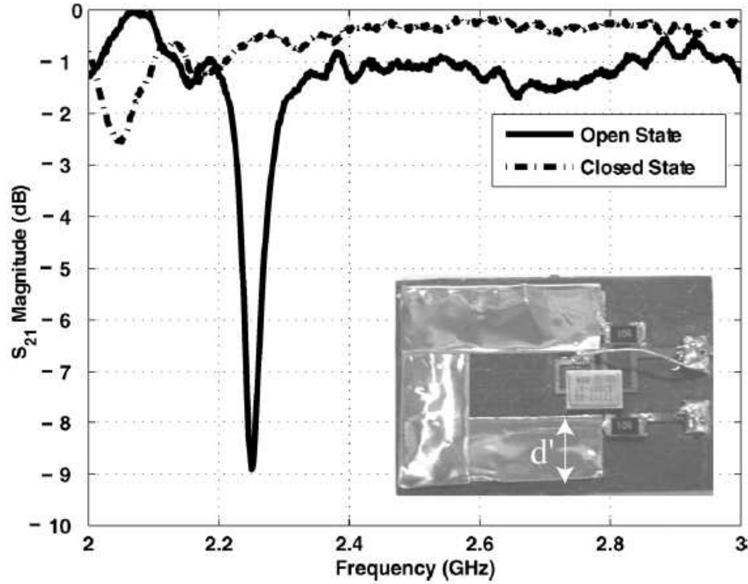

Figure 2.31: Open and closed switch responses for an SRR with a MEMS switch placed in parallel. In the closed-state, the MEMS switch shorts the SRR, preventing a resonant response. The 100 kΩ resistors are used for isolating the DC voltage source [5].

Hand and Cummer also demonstrate that inserting a MEMS switch alters the resonant behavior of the SRR [5]. The MEMS switch introduces a parasitic parallel capacitance which shifts the resonant frequency of the SRR [5]. The shift in resonant frequency can be seen when comparing Figure 2.32 to Figures 2.30 and 2.31.

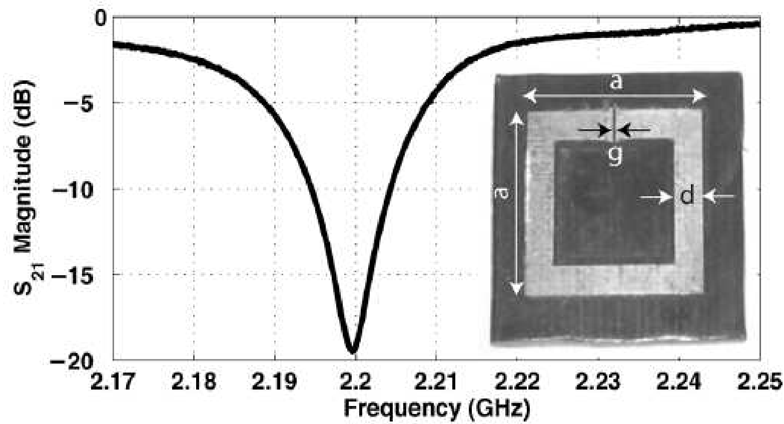

Figure 2.32: Resonance of an SRR without a MEMS switch. Inserting a MEMS switch alters the SRR resonant frequency [5] (compare to Figures 2.30 and 2.31).

Hand and Cummer demonstrate the feasibility of a tunable metamaterial element using MEMS technology, however, the MEMS device is only used as a switch and not as the capacitive element. Although the device is smaller than a varactor diode, the TeraVicta switch device still uses valuable area outside of the SRR unit structure as shown in the insets of Figures 2.30 and 2.31.

2.5 Chapter Summary

This chapter presented a comprehensive review on MEMS capacitive and contact switches. However, MEMS device designers are still trying to conquer the challenging aspects of RF MEMS switches such as lowering actuation voltage, reducing stiction, increasing switching speed, increasing power handling, and increasing lifetime and reliability [31]. A review of metamaterial, SRRs, and capacitors on SRR circuits was presented that provides the foundation for this research. The next chapter discusses the theory of cantilever bending and SRR resonance.

III. Theory

3.1 Chapter Overview

This chapter introduces the beam mechanics of the MEMS cantilever used for this thesis. Beam bending theory from Shigley [49] is used to produce analytical beam equations. This chapter also presents capacitance modeling of parallel plates and briefly touches on the physics of SRRs.

3.2 Theory of Design

A hybrid MEMS capacitive switch is used in this study to change the resonant frequency of an SRR. The mechanical design of this switch is based on a cantilever beam model while the electrical design is based on a parallel plate capacitor model. A capacitive cantilever MEMS device was chosen for use in this design because of its micrometer-size geometry, low actuation voltage (< 30 V), and large on-off capacitance ratio ($40 : 1$). In addition, the length of the split ring gap (300 μm) is an average distance for a cantilever length. Figure 3.1 shows a schematic of the core capacitive cantilever design used in this study, and is referred to in the following discussion. The cantilever beam is rigidly fixed (anchored) at one end of the SRR and free to move at the other end. The anchor also serves as an electrical connection between the beam and SRR. The cantilever extends across the SRR gap and overlaps the other split end of the SRR by a length of L_o. When a voltage is applied to the electrode, electrostatic forces pull the beam downwards. As voltage is increased, the electrostatic force eventually overcomes the mechanical restoring force of the material, and the end of the beam snaps down onto the dielectric. The beam snap-down increases the total capacitance of the SRR since one end of the beam is electrically connected to the SRR. Increasing the voltage further brings more of the beam in contact with the dielectric thus increasing the capacitance between the cantilever beam and SRR. This actuation method provides a limited tuning range since the max capacitance of the two plates is not reached until the overlapped beam is fully collapsed down onto the dielectric.

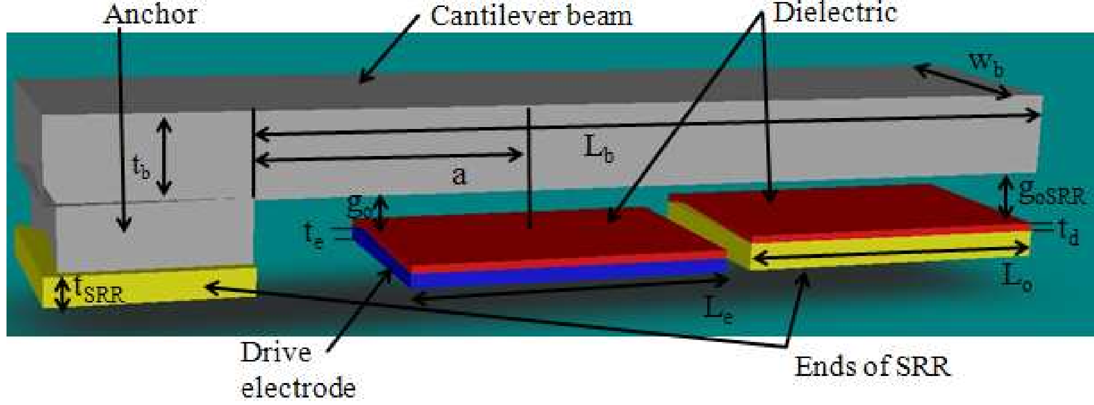

Figure 3.1: Schematic drawing of a capacitive cantilever used in this study. The cantilever is anchored to one end of the SRR. The other end of the beam is electrically isolated from the SRR. The electrode pulls the beam down to increase total capacitance of the SRR structure.

3.3 Cantilever Beam Model

The beam models discussed in this chapter are assumed to be flat and not curled up due to residual stress created from the fabrication process (experimentation proves this to be an incorrect assumption since the electroplating step introduces stress into the cantilever beam).

3.3.1 Tip Deflection. The applied force, F_a, that deflects the cantilever beam comes from electrostatic forces generated when a potential voltage is applied between the beam and the drive electrode (as discussed in Chapter 2). In this design, the electrode is positioned at an intermediate location underneath the beam with the electrode's center positioned at length, a, from the anchor as shown in Figure 3.1. For simplicity, the electrostatic force generated from the electrode is considered as a point source load, F_a, applied at position a as shown in Figure 3.2.

From mechanical engineering theory, maximum beam tip deflection, d, due to an applied force, F_a, at position a along the beam is found using [18, 23, 49]:

$$d = \frac{F_a a^2}{6\tilde{E}I_z}(3L_b - a) \ \ (\mu\text{m}) \tag{3.1}$$

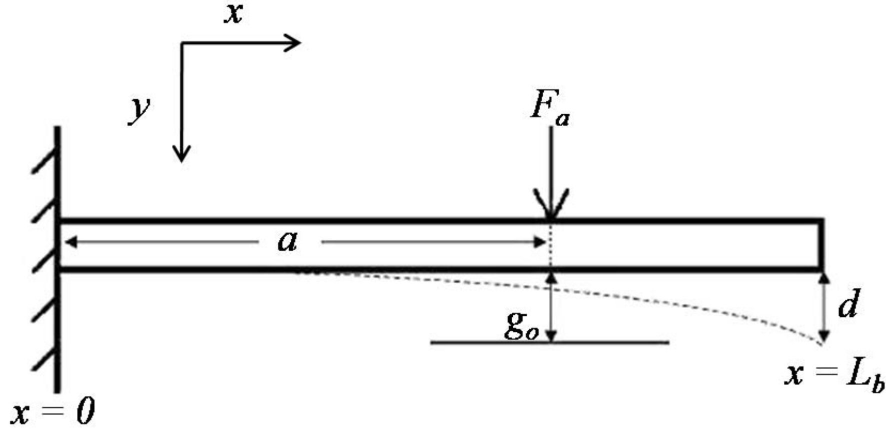

Figure 3.2: A cantilever beam with fixed end at $x = 0$, a free end at $x = L_b$, and an intermediately placed load, F_a, at length a along the beam. The electrostatic force generated by the electrode (labelled as a point source load for simplicity) attracts the free end of the beam downward by a distance of d. [16].

where F_a is the applied force, a is the load position, L_b is the length of the cantilever beam, $\tilde{E}$ is the Effective Young's modulus, which for wide beams ($w_b \geq 5t_b$, where w_b is the width of the beam and t_b is the thickness of the beam) is given by [50]:

$$\tilde{E} = \frac{E}{(1 - \nu^2)} \text{ (GPa)} \tag{3.2}$$

where E is Young's Modulus ($E = 80$ GPa was used for Au in this study [16]), ν is Poisson's Ratio of the beam material, and I_z is the moment of inertia about the z-axis. The moment of inertia is a measure of the dispersion of area about the centroid (center of gravity) of the beam and is given by [23, 49]:

$$I_z = \frac{w_b t_b^3}{12} \text{ } (\mu\text{m}^4) \tag{3.3}$$

3.3.2 Spring Constant. Young's modulus, also known as the modulus of elasticity, is the ratio of stress-to-strain in a body undergoing elastic deformation. In other words, it is the measure of the stiffness of a material [23, 49]. When a beam is loaded, it deforms and deflects. In this study, the beam deflects in the y direction

as shown in Figure 3.2. After load removal, the elasticity of the material forces the beam to return to its original configuration as long as the material's elastic limit was not surpassed [49]. The beam behaves like a spring because it has a mechanical element that exerts a force when deformed in the linear elastic region—the mechanical restoring force. Hooke's law equates the force from the applied load to the beam's mechanical restoring force [20, 49]:

$$k = \frac{F_s}{d} \quad \left(\frac{\mu\text{N}}{\mu\text{m}}\right) \tag{3.4}$$

where k is the spring constant of the cantilever, F_s is the mechanical restoring force of the beam, and d is the deflection distance at the tip of the cantilever found using Equation (3.1).

Substituting Equation (3.3) into Equation (3.1) and solving for the applied force over deflection derives an alternate expression for the spring constant. The expression is then set equal to Equation (3.4) resulting in:

$$k_1 = \frac{\tilde{E} w_b t_b^3}{2a^2(3L_b - a)} \quad \left(\frac{\mu\text{N}}{\mu\text{m}}\right) \tag{3.5}$$

where k_1 is the spring constant for the model in Figure 3.2.

3.3.3 Improved Beam Model. Meng et al. [51] developed an improved beam model, shown in Figure 3.3 that accounts for the effects of the anchor height on beam deflection. Using the method of moments, Meng et al. derived an improved analytical model for tip deflection, d_1 (with an error–missing w_b, corrected here) [51]:

$$d_1 = \frac{2(1-\nu^2)}{\tilde{E} w_b t_b^3}(-L_b^3 + 3aL_b^2 + (L_b - a)^3 + 6aL_b l)F_a \quad (\mu\text{m}) \tag{3.6}$$

where l is the anchor height ($t_b + g_0$), and g_0 is the initial gap between the two plates at zero bias. The use of Hooke's law produces a new spring constant for the improved beam model:

$$k_2 = \frac{\tilde{E} w_b t_b^3}{2(1-\nu^2)(-L_b^3 + 3aL_b^2 + (L_b - a)^3 + 6aL_b l)} \quad \left(\frac{\mu\text{N}}{\mu\text{m}}\right) \tag{3.7}$$

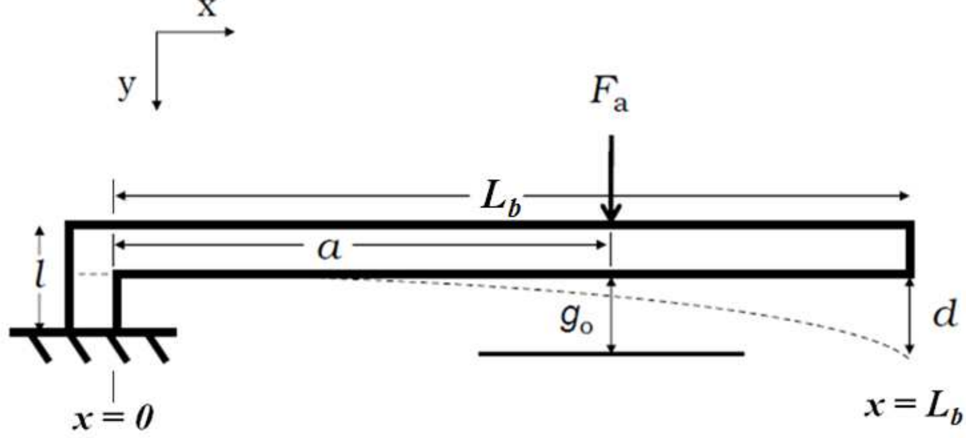

Figure 3.3: Improved cantilever beam model with fixed end at $(x = 0)$, a free end at $(x = L_b)$, and an intermediately placed load, F_a, at position a along the beam. Effects of anchor height, l, on beam tip deflection are considered in this model [20,51].

3.3.4 Parallel Plate Capacitor Models and Electrostatic Force. Recall that applying voltage to the pull-down electrode on the cantilever beam induces an electrostatic force. This electrostatic force is approximated by modeling the beam and SRR as a parallel-plate capacitor. The charge Q on each plate is given by [52]:

$$Q = CV \quad \text{(Coulomb)}. \tag{3.8}$$

The energy stored by the parallel plates at a constant voltage is given by [18,52]:

$$W = -\frac{1}{2}CV^2 = \frac{\varepsilon_0 A V^2}{2(d + \frac{t_d}{\varepsilon_r})} \quad \text{(J)}. \tag{3.9}$$

Potential energy is then converted to a force by taking the derivative of the electrostatic energy with respect to the distance separating the plates (distance separating plates includes dielectric thickness) [7,18,20,37,52]:

$$F_e = \frac{V^2 \varepsilon_0 w_b L_e}{2\left(g + \left(\frac{t_d}{\varepsilon_r}\right)\right)^2} \quad (\mu\text{N}) \tag{3.10}$$

where L_e is the length of the electrode and g is the gap height. F_e is represented by the externally applied load, F_a, in Figures 3.2 and 3.3.

3.3.5 Pull-in Voltage (Electrostatic Actuation). Using the beam and parallel plate capacitance models previously discussed, an expression for pull-in voltage, V_{pi}, is derived. The pull-in voltage is defined as the voltage at which the electrostatic force between the beam and drive electrode overcomes the mechanical restoring force of the beam, and the beam snaps down [7]. In equilibrium, F_e is equal to F_s, therefore, substituting Equation (3.10) into Equation (3.4), letting $g = g_0 - d$, and solving for voltage results in [7, 20]:

$$V_1 = \left(g_0 + \frac{t_d}{\varepsilon_r} - d\right) \sqrt{\frac{2kd}{\varepsilon_0 w_b L_e}} \quad (\text{V}). \tag{3.11}$$

To reduce the equation to one unknown, it is necessary to find the deflection distance, d, at the point where electrostatic forces overcome the mechanical restoring forces and the beam pulls-in. The deflection distance at which the beam pulls-in is renamed as the pull-in distance, d_{pi}, which is found by taking the derivative of Equation (3.11) with respect to d and setting the equation equal to zero—the height (d) at which equation instability occurs is the pull-in distance [7]. The deflection distance at which maximum voltage occurs is [7]:

$$d_{pi} = \frac{g_0}{3} \quad (\mu\text{m}). \tag{3.12}$$

The cantilever beam deflection becomes unstable at ($g_0/3$) because of a positive feedback loop in the electrostatic actuation of the beam. This is better understood by reviewing electrostatic force in terms of charge and electric field [7]:

$$F_e = \frac{Q\overrightarrow{E}}{2} \quad (\mu\text{N}) \tag{3.13}$$

where Q is the charge on the beam and $\overrightarrow{E} = V/g \left(\frac{\text{V}}{\mu\text{m}}\right)$ is the electric field due to the applied voltage. When the actuation voltage increases, the electrostatic field between the parallel plates increases, which increases the electrostatic force. This increase in force instantaneously pulls the beam downward thus decreasing the gap height, g, which, in turn, increases the parallel plate capacitance (recall Equation 2.4). This increase in capacitance further increases the charge and electric field, thus completing the feedback loop [7].

An expression for pull-in voltage, V_{pi}, is found by substituting Equation (3.12) into Equation (3.11) resulting in [7, 30]:

$$V_{pi} = \left(g_0 + \frac{t_d}{\varepsilon_r} - d_{pi}\right)\sqrt{\frac{2kd_{pi}}{\varepsilon_0 w_b L_e}} \quad (\text{V}). \tag{3.14}$$

By neglecting the thickness of the dielectric, Equation (3.14) is simplified with little error to:

$$V_{pi} = \sqrt{\frac{8g_0^3 k}{27\varepsilon_0 w_b L_e}} \quad (\text{V}). \tag{3.15}$$

3.3.6 Improved Pull-in Model. The previous expressions for pull-in voltage exclude the effects of fringing field capacitance which could introduce an error of 20 percent [7, 50]. Chowdhury et al. [50] take into account the capacitance due to the fringing fields. Thus, the total capacitance is comprised of parallel plate capacitance and fringing fields due to the width, thickness, and free end of the beam as shown in Figure 3.4. The improved model for the parallel plate capacitance is given by [50]:

$$C = \varepsilon_0 L_o \left[0.77 + \left(\frac{w_b}{g_0 + \frac{t_d}{\varepsilon_r}}\right) + 1.06\left(\frac{w_b}{g_0 + \frac{t_d}{\varepsilon_r}}\right)^{\frac{1}{4}} + 1.06\left(\frac{t_b}{g_0 + \frac{t_d}{\varepsilon_r}}\right)^{\frac{1}{2}}\right] \quad (\text{pF}) \tag{3.16}$$

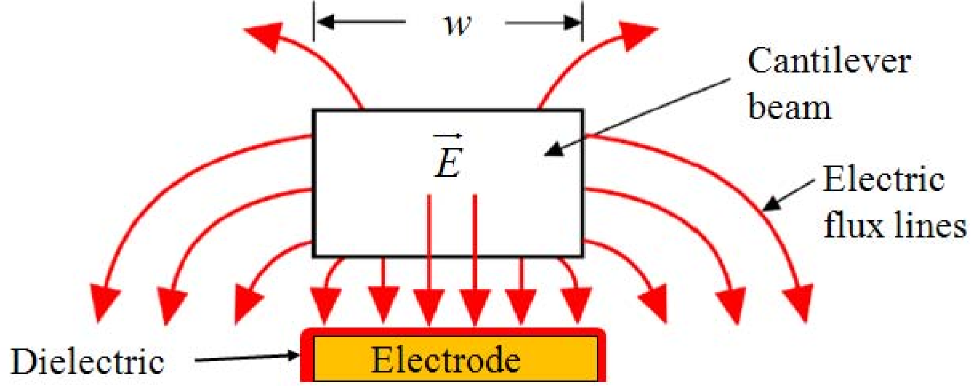

Figure 3.4: Cantilever beam showing electric-flux fringing fields which increase total capacitance [50].

where L_o is the distance the beam overlaps the SRR as shown in Figure 3.1. Chowdhury et al. also take into account that the electrostatic force on the beam becomes non-uniform due to the redistribution of the charges as the beam deflects downward as shown in Figure 3.5. Therefore, the tip area experiences a higher electrostatic force than the rest of the beam [50].

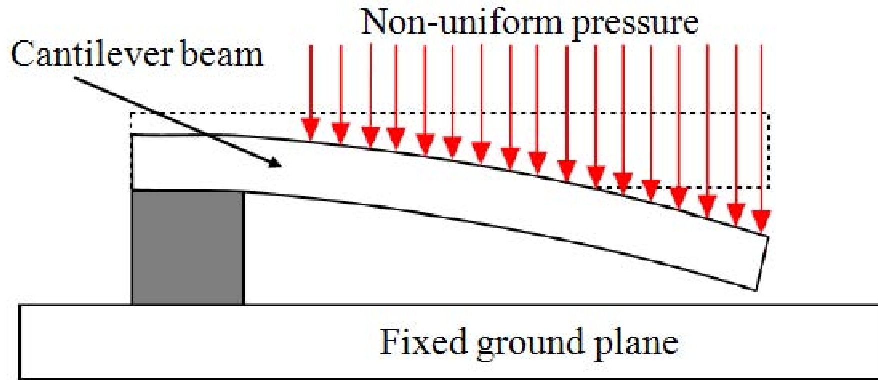

Figure 3.5: Non-uniform pressure profile of the electrostatic pressure on a cantilever beam during actuation [50].

Accounting for the effects of fringing field capacitance and non-uniform electrostatic forces on the beam, Chowdhury et al. [50] provide a new closed-form model to determine the pull-in voltage:

$$V_{pi} = \sqrt{\frac{2\tilde{E}t_b^3 g_0}{8.37\varepsilon_0 L_b^4 \left(\frac{5}{6g_0^2} + \frac{0.19}{g_0^{1.25}w_b^{0.75}} + \frac{0.19}{g_0^{1.25}L_e^{0.75}} + \frac{0.4t_b^{0.5}}{g_0^{1.5}w_b}\right)}} \text{ (V)}. \qquad (3.17)$$

This equation, assumes the total area under the cantilever beam is acting like an electrode, therefore, a deviation from Meng's pull-in voltage is expected.

3.3.7 Collapse Voltage. As described in Chapter 2, it is necessary to bias switches past V_{pi} to increase contact area for a reduced contact resistance. In the case of a capacitive switch, a maximum contact area is also desired to increase the total amount of on-state capacitance. The cantilever in this design is overdriven past its pull-in voltage to increase capacitance, however, at a certain voltage, the cantilever collapses onto the bottom electrode as discussed in Chapter 2. After pull-in is reached, the cantilever is modeled as a fixed end beam with a simply supported end at $x = L_b$ as shown in Figure 3.6. A new spring constant, k_{ss}, for the stiffened structure is given by [20]:

$$k_{ss} = \frac{-\tilde{E} w_b t_b^3 L_b^3}{a^2 b((3L_b(b^2 - L_b^2)) + a(3L_b^2 - b^2))} \quad \left(\frac{\mu\text{N}}{\mu\text{m}}\right) \tag{3.18}$$

where $b = L_b - a$. Collapse voltage, V_{cpi}, is defined as the voltage where the beam collapses onto the electrode. In this study, if the beam collapses, the device does not short out because the electrode is coated with a dielectric layer (Si_3N_4). However, collapse should be avoided to reduce the chance of beam failure due to dielectric breakdown or stiction. The collapse voltage is given by [16, 20]:

$$V_{cpi} = (g_0 - d_e)\sqrt{\frac{2k_{ss}d_e}{\varepsilon_0 w_b L_e}} \quad (\text{V}) \tag{3.19}$$

where g_0 is the initial gap under the beam and d_e is the remaining distance to the top of the electrode (collapse distance). Detailed derivation of V_{cpi} can be found in Coutu's dissertation [20].

3.3.8 Release Voltage. Once a beam pulls-down, applied voltage may be significantly reduced while still keeping the beam in a down-state position. A pulled-in beam does not require the same pull-in voltage to stay clamped down because there is

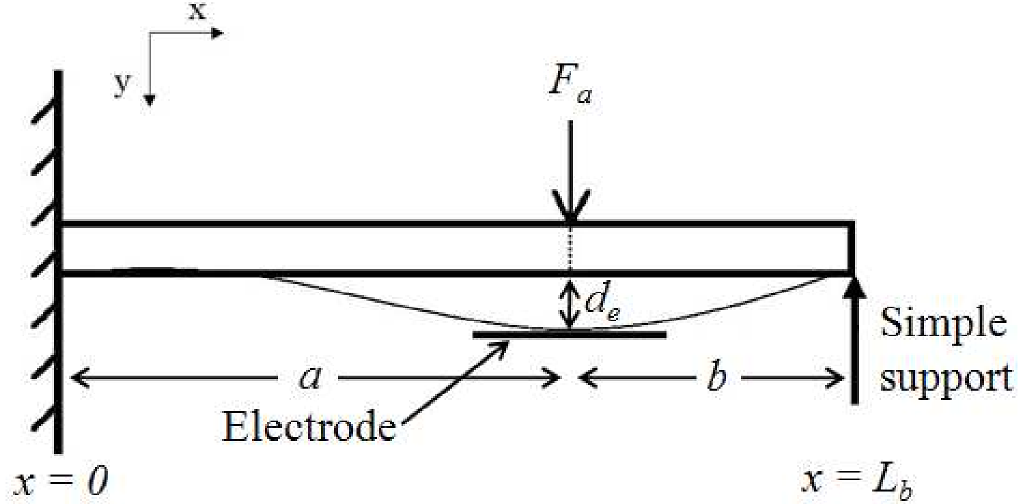

Figure 3.6: Cantilever beam model with a fixed end at $x = 0$ and a simple support at $x = L_b$. The simply supported beam has a stiffer spring constant then a cantilever beam [16].

little to no distance between the plates—recall Equation 2.1 where decreasing distance increases the electrostatic force regardless of applied voltage. As applied voltage reduces, the point at which mechanical restoring forces overcome the electrostatic forces and the beam releases (V_r) is found by [7]:

$$V_r = \sqrt{\frac{2k}{\varepsilon_0 \varepsilon_r w_b L_e}(g_0 - d_e)\left(d_e + \frac{t_d}{\varepsilon_r}\right)^2} \text{ (V)}. \tag{3.20}$$

Equation 3.20 is accurate up to $d_e \simeq 0$, but not at $d_e = 0$, primarily due to the unknown adhesion and repulsion forces between the metal and dielectric made at intimate contact ($d_e = 0$) [7].

3.3.9 Dielectric Breakdown Voltage. Dielectrics have a material parameter called dielectric strength. The dielectric strength (given in V/m) is the maximum electric field a dielectric can withstand before it can no longer electrically isolate charged bodies [52]. At breakdown, the electric field frees the bound electrons within the dielectric, thus creating a conductive path (short) between the electrodes. The

instantaneous, massive current flow superheats and destroys the dielectric layer and the underlying electrode as shown in Figure 3.7.

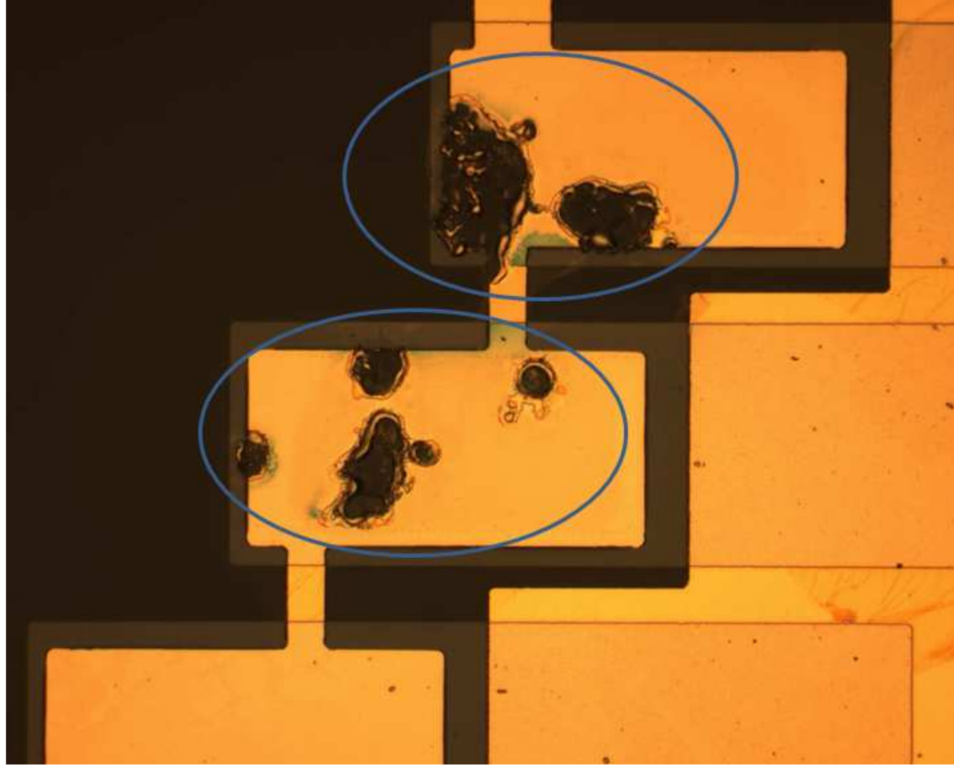

Figure 3.7: A photograph showing areas where dielectric breakdown occurred (circled). The dielectric breakdown creates a conductive path (short) between plates. The massive current flow that results superheats and then melts the dielectric and Au electrode (cantilever beams have been removed with a probe for illustration purpose).

The voltage at which breakdown occurs (V_{br}) is calculated by multiplying the dielectric's electric field strength ($\vec{E}_{ds}$) by its thickness:

$$V_{br} = \vec{E}_{ds} t_d \ \text{(V)} \tag{3.21}$$

3.3.10 Mechanical Resonant Frequency. Mechanical resonant frequency of a MEMS cantilever switch is given by [53]:

$$f_0 = \frac{\sqrt{\frac{k}{m}}}{2\pi} \ \text{(Hz)} \tag{3.22}$$

where m is the mass of the cantilever.

The switching time is then calculated by [53]:

$$t_s \simeq 3.67 \frac{V_{pi}}{V_s 2\pi f_0} \quad (\mu s) \tag{3.23}$$

where V_s is the actuation voltage.

The theoretical cut-off frequency of a capacitive switch is calculated by [12]:

$$f_{cut-off} = \frac{1}{2\pi R C_{pp}} \quad (\text{Hz}) \tag{3.24}$$

3.4 Two-port Network Model

The MEMS capacitive switch can be modeled as a two-port network shown in Figure 3.8. Where R_s is the beam resistance, L is the inductance, $C(t)$ is the time varying capacitance, and Z_0 is the line impedance [8].

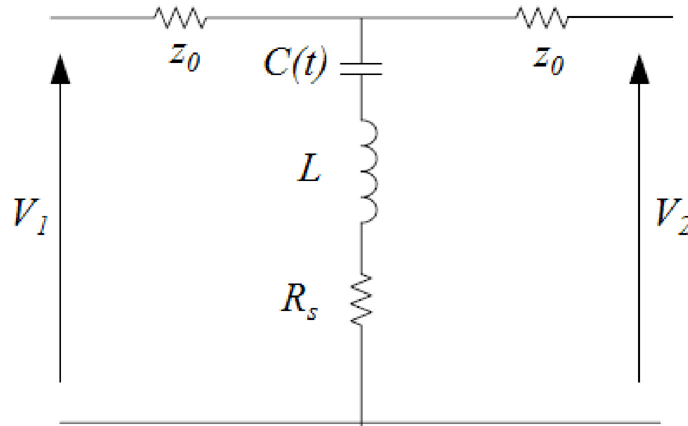

Figure 3.8: Equivalent circuit model of a capacitive RF MEMS switch [8].

The beam resistance is given by [8]:

$$R_s = \frac{L_b}{w_b} \sqrt{\frac{\mu \pi f}{\sigma}} \; (\Omega) \tag{3.25}$$

where f is the frequency, μ is the magnetic permeability of the beam, and σ is the conductivity of the beam. The beam inductance is given by [8]:

$$L = \frac{R_s}{2\pi f} \text{ (H)} \tag{3.26}$$

3.5 Figures of Merit

Figures of merit are dimensionless values used to assess and compare the capabilities and performance of electronic devices. [54].

3.5.1 Quality Factor. The Q (quality) factor compares the time constant for decay of an oscillating system to its period. A high Q factor would indicate that the oscillations of a system decay slower than a low Q factor system. Quality factor is given by [5]:

$$Q = \frac{1}{R}\sqrt{\frac{L}{C}} \tag{3.27}$$

3.5.2 S-Parameters. A commonly used figure of merit is a set of S (scattering) parameters used to represent reflection and transmission coefficients of a two-port network operating at microwave frequencies [27]. S parameters are ratios of the powers of travelling waves [54]:

$$\begin{bmatrix} b_1 \\ b_2 \end{bmatrix} = \begin{bmatrix} s_{11} & s_{12} \\ s_{21} & s_{22} \end{bmatrix} \begin{bmatrix} a_1 \\ a_2 \end{bmatrix} \qquad \begin{aligned} b_1 &= s_{11}a_1 + s_{12}a_2 \\ b_2 &= s_{21}a_1 + s_{22}a_2 \end{aligned}$$

The letters a and b are the powers of incoming (incident) and outgoing (reflected) waves, and subscripts 1 and 2 represent the input and the output of the two-port network, respectively. Figure 3.9 shows the two-port network with incident and reflected waves labelled.

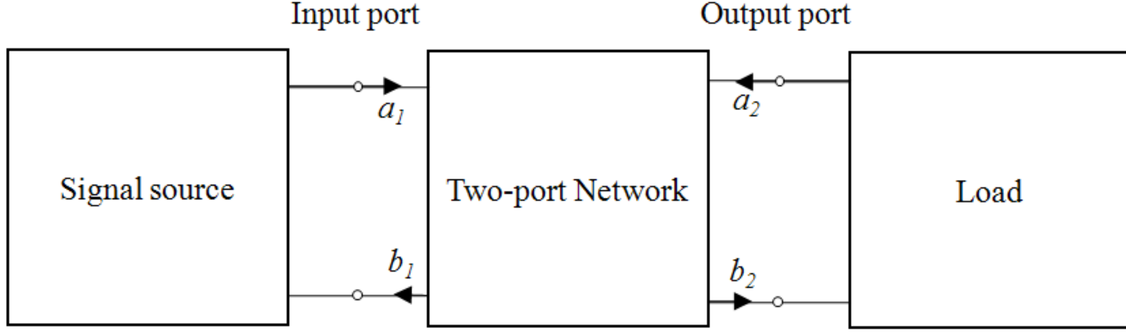

Figure 3.9: Two-port network characterized by S parameters [54].

Expressions for S parameters are found by terminating the incident waves a_1 and a_2 [27]:

$S_{11}=\frac{b_1}{a_1}\Big|_{a_2=0}$ Input Reflection Coefficient

$S_{12}=\frac{b_1}{a_2}\Big|_{a_1=0}$ Reverse Transmission Coefficient

$S_{21}=\frac{b_2}{a_1}\Big|_{a_2=0}$ Forward Transmission Coefficient

$S_{22}=\frac{b_2}{a_2}\Big|_{a_1=0}$ Output Reflection Coefficient

3.6 Split Ring Resonators

A split ring resonator (SRR) is the common name for a structure that creates a bulk permeability from non-magnetic materials. The effect is created by the split-ring geometry where the structure sizes are much smaller than the operating wavelength (as discussed in Chapter 2) The SRR structures create an inductance and capacitance such that it can be modeled as an RLC circuit where the inductance arises from the rings and the total capacitance of the SRR structure comes from the split ring gap capacitance and the gap of the concentric rings [2]. An equivalent circuit diagram of an SRR is shown in Figure 3.10. The capacitance and inductance of the SRR determine its resonant frequency as shown in Equation 3.28 (repeated for convenience) [5, 47]:

$$\omega_0 = \frac{1}{\sqrt{LC}} \quad \left(\frac{\text{rad}}{\text{sec}}\right) \tag{3.28}$$

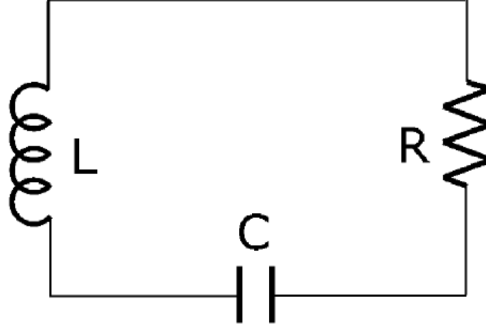

Figure 3.10: SRR equivalent circuit diagram [5].

The magnetic response of an SRR-type structure can be mathematically modeled as [55]:

$$\mu(\omega) = 1 - \frac{\omega_{pm}^2}{\omega^2 - j\Gamma_m\omega} \tag{3.29}$$

where ω_{pm} is the magnetic plasma frequency and Γ_m is a damping term associated with losses in the material. Assuming there are no losses for frequencies less than the plasma frequencies and $\omega < \omega_{pm}$, the constitutive parameter of effective permeability ($\mu(\omega)$) is negative. The plasma frequency is a function of the capacitance and inductance, both of which are controlled by varying aspects of the SRR geometry.

When using two split rings, the resonant frequency is found by [2]:

$$\omega_0 = \sqrt{2\pi L_{av}\left(\left(\frac{\pi C_g}{2}\right) + C_{OR} + C_{IR}\right)} \text{ (Hz)} \tag{3.30}$$

where L_{av} is the average inductance of the two rings, C_g is the capacitance due to the gap of the concentric rings, and C_{OR} and C_{IR} are capacitances due to the outer and inner splits, respectively (see Figure 3.11). Split capacitance is found using Equation 2.4 from Chapter 2.

An approximation of induction for a square ring is given by [5]:

$$L \approx \frac{\lambda_0 \mu_0}{5\pi}\left(2.3log_{10}\left(\frac{8\lambda_0}{5w_{SRR}}\right) - 2.85\right) \text{ (H)} \tag{3.31}$$

where λ_0 is free space wavelength(side length a=$\lambda_0/10$), and w_{SRR} is the SRR width (see Figure 3.11).

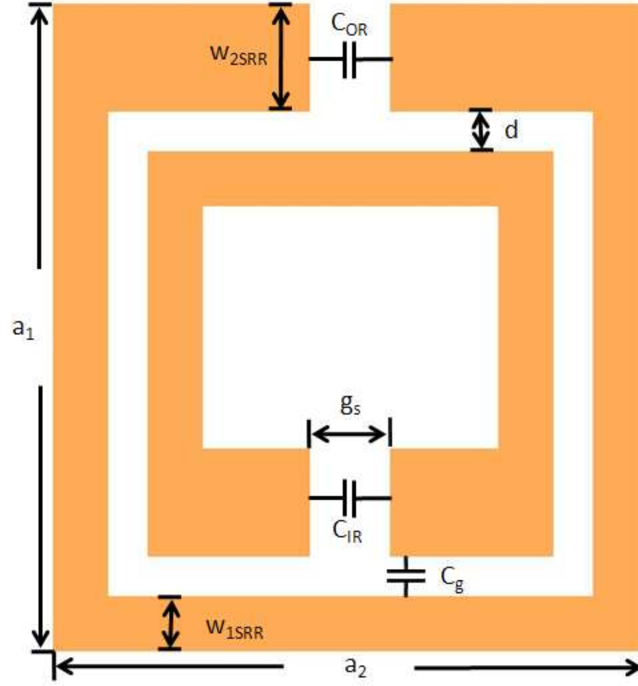

Figure 3.11: SRR unit cell with labeled ring dimensions.

More detailed calculations can be found in [45]. The capacitance of the split rings, however, must take into account the gap capacitance between rings as shown in Figure 3.11 [45]:

$$C_1 = C_{OR} + \frac{C_g}{2} \text{ (F)}, \quad C_2 = C_{IR} + \frac{C_g}{2} \text{ (F)}. \tag{3.32}$$

It should be noted that there are multiple shapes and geometries of SRRs that also demonstrate the capability to create magnetic effects, each with associated advantages and disadvantages [55]. For the purpose of this paper, the SRR in Figure 3.11 will be the sole focus.

3.7 Chapter Summary

This chapter presented a review of the necessary theory for an overall understanding of MEMS cantilever beam capacitive switches and SRR operation. There are many equations for spring constants and pull-in voltages derived from different authors, however, Meng's spring constant equation contains the most variables relevant to this thesis. More information on SRR operation is found in [55]. The next chapter explains device design and fabrication.

IV. Design and Fabrication

4.1 Chapter Overview

This chapter presents cantilever array, SRR, stand-alone test structure designs, and the custom fabrication process used to create them. Luo, Smith, Gil, Hand, and Cummer's research (reviewed in Chapter 2) influenced the design of the MEMS device and the SRR structure.

4.2 Design

4.2.1 Varactor Design. The core cantilever design shown in Figure 4.1 was used in creating an array of cantilevers.

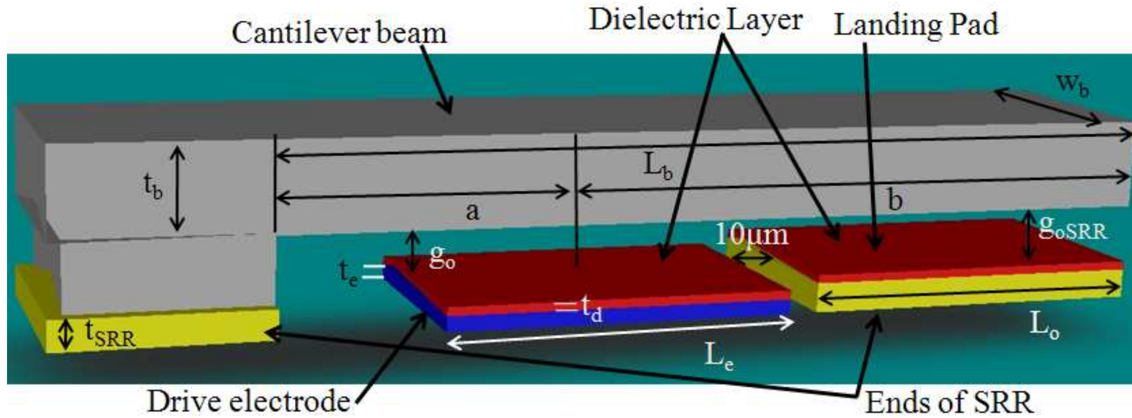

Figure 4.1: Schematic drawing of core cantilever model used in this study. The electrode pulls the beam down onto the landing pad, which increases SRR capacitance (see Table 4.1 for color legend).

Table 4.1: Coventor color legend for Figures 4.1 and 4.2. Colors are listed in the order fabricated.

Color	Material	Layer
Yellow	Gold	SRR
Blue	Gold	Electrode
Red	Silicon Nitride	Dielectric
Grey	Gold	Anchor and Beam

The cantilever array shown in Figure 4.2 is comprised of five core cantilevers that range in length from 400 μm to 300 μm in 25 μm increments, with a spacing

between beams of 10 μm. The widths of the beams are 75 μm except for the 400 μm long cantilever which is 60 μm wide due to size constraints. The changes in width alter the spring constant and capacitance of the beam, but it does not affect pull-in voltage (this statement is proved inaccurate during testing and is discussed in Chapter 6). The cantilevers are anchored at one end of the split ring; they extend across the split and overlap the other side of the split ring by 120 μm.

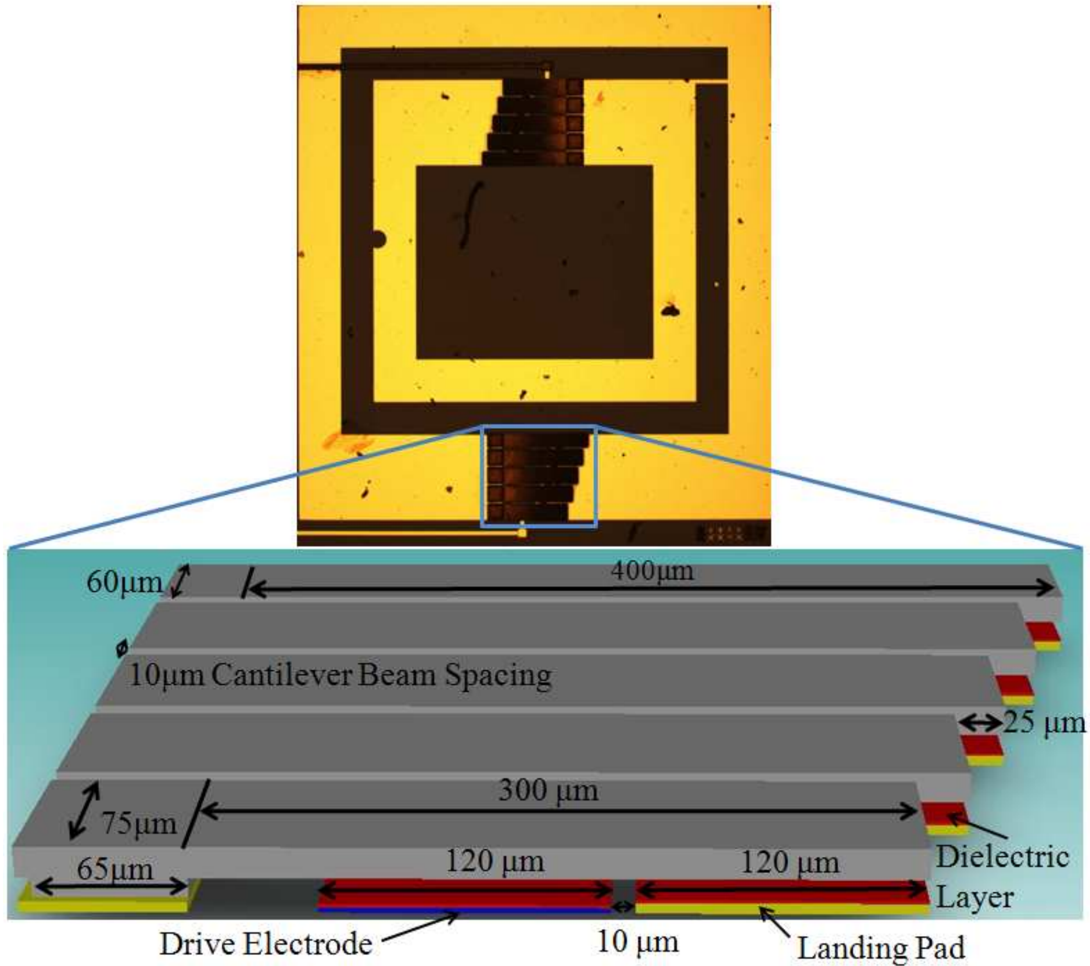

Figure 4.2: Photograph (from microscope) of a unit cell SRR with cantilever arrays spanning the split ring gap. Inset: Schematic drawing of a multi-cantilever variable capacitor. Cantilever lengths range from $300 - 400$ μm in increments of 25 μm. The longest cantilever, which has the lowest spring constant, pulls-in first followed by the next longest beam.

These beam dimensions were specifically chosen to produce a large on-off capacitance ratio with low actuation voltages. Specifically, each cantilever is predicted to

actuate between $22 - 98$ V depending on its length and thickness, and to contribute roughly $2.2 - 3.7$ pF of capacitance in the down-state.

Not shown in Figure 4.2 is that all electrodes in the array are electrically connected, therefore, one voltage source controls all beams. As voltage is applied to the drive electrode, the longest cantilever is the first to snap down since its spring constant is the lowest. Increasing voltage results in pulling the remaining beams down one–by–one (longest–to–shortest), realizing a step increase in capacitance [40].

The cantilever array shown in Figure 4.2 is similar to that of Luo et al.'s varactor shown in Figure 2.18, however, there are key differences in this design. First, to avoid multiple beams pulling in at the same time, the beam lengths differ from each other by 25 μm instead of 5 μm. Also, the electrode and landing pads are not the same element, instead the electrode and landing pad are separated, which decreases failures caused by stiction and dielectric breakdown. Additionally, the electrode thickness is slightly less ($0.1 - 0.5$ μm, depending on fabrication) than the SRR thickness. The lower electrode ensures that the beam contacts the landing pad first as it pulls-in. It also increases the amount of voltage needed to collapse the beam onto the electrode because after pulling-down to the landing pad, the beam becomes a fixed/simple-support fixture (as shown in Figure 3.6).

4.2.1.1 Dielectric Selection. This study uses silicon nitride Si_3N_4 as the dielectric layer because of its availability (at AFRL/RY) and high dielectric constant ($6 - 7.8$) [40,56]. Silicon nitride is deposited using plasma enhanced chemical vapor deposition (PECVD). The dielectric strength for PECVD silicon nitride is 5 MV/cm [13,18,56] corresponding to a breakdown voltage of 150 V for a 3000 Å-thick silicon nitride film (recall Equation 3.21). Silicon nitride, when compared to silicon dioxide, has a comparable breakdown strength with nearly twice the dielectric constant. However, PECVD silicon nitride can be plagued with pin holes and poor step coverage which may cause breakdown to occur lower than its theoretical breakdown voltage (V_{br}) [56]. It is also impractical to deposit a silicon nitride film thinner than

1000 Å using PECVD because large pin holes are generated, which results in a low dielectric breakdown [13].

4.2.1.2 Structural Materials. This design uses Au as the SRR structural metal because it is conductive, evaporates and then condenses at a low stress [18], and is compatible with standard lift-off technology. This project also utilized Au for the cantilever beam material because it deposits at a low stress (compared to other metals) when electroplated [18].

4.2.2 SRR design. SRR dimensions were chosen to provide a resonant frequency around 10 GHz. SRR geometries from Smith et al.'s [6] research were used to create two generic split rings (an inner and outer ring). As shown in Figure 4.3, the MEMS cantilever array required a modification of the split rings. Modifications

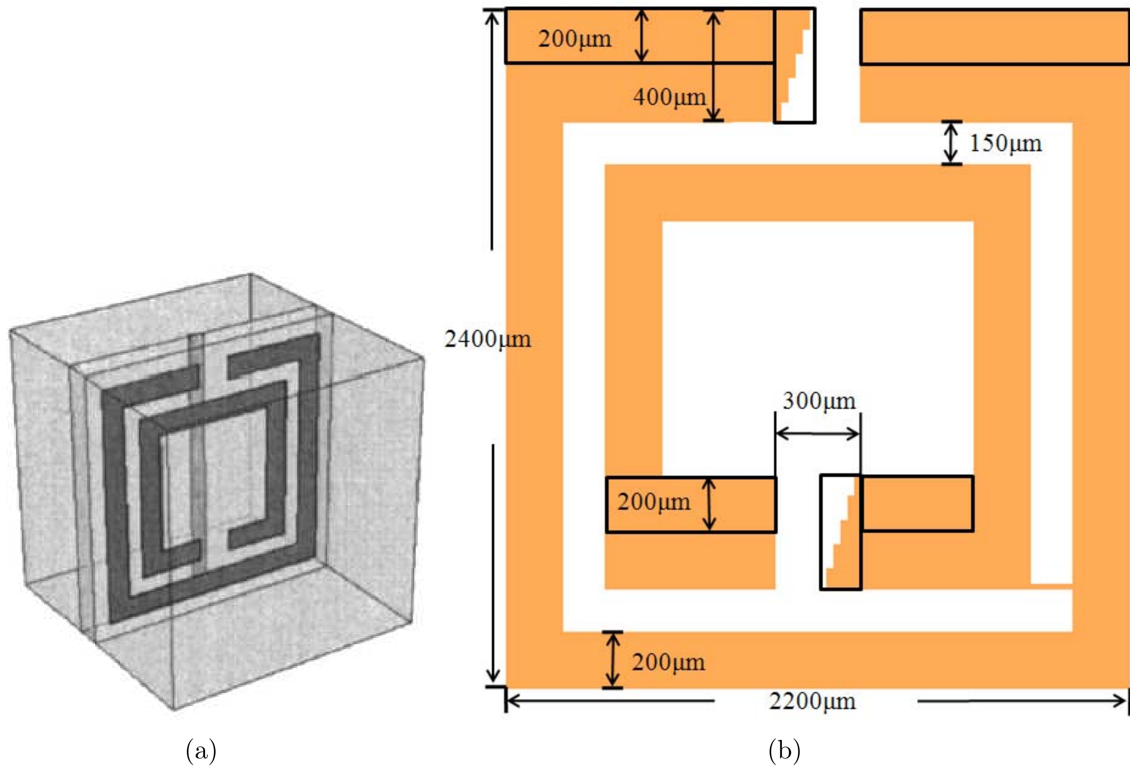

Figure 4.3: Original SRR design concept from Smith et al. [6] (a) and the modified design used in this study (b), which shows the added geometry (boxed) used to make area for the cantilever arrays. The SRR design layout was created in L-edit.

include widening the sides with the split ends by 200 μm to create area for the cantilever array. The split end was also narrowed (in a stair-step fashion) so that each cantilever would have the same landing pad area.

The resonant frequencies of the two geometries are close enough to one another that the resonant frequency of the inner ring is approximately equal to the resonant frequency of the outer ring ($\omega_{IR} \approx \omega_{OR}$) [45]. The outer ring provides a strong magnetic response where the real part of permeability is negative. The inner ring reduces resonant frequency because of its additional capacitance coupled to the outer ring. Also, the inner ring split must be located at the opposite side from the outer ring split, otherwise the gap capacitance, C_g, is not connected in parallel to the split capacitance [45].

4.2.3 SRR with Multi-Cantilever Design. The final unit cell SRR design with cantilever arrays and voltage supply lines is shown in Figure 4.4.

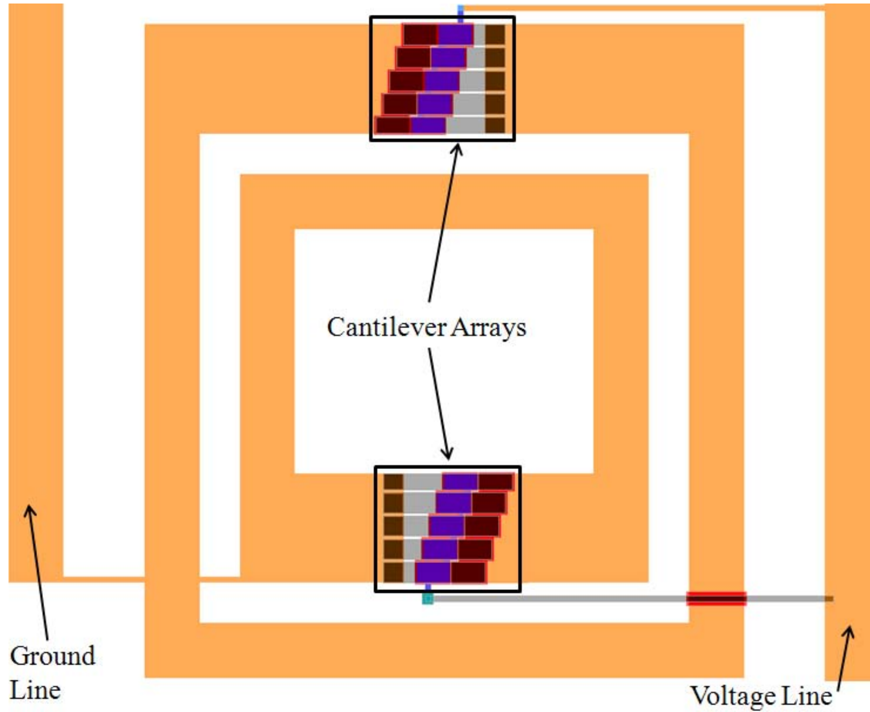

Figure 4.4: Unit cell SRR with cantilever arrays anchored to inner and outer split rings. Ground and voltage lines supply bias voltage for actuating the cantilever arrays (see Figure 4.5 for inset and Table 4.2 for color legend).

Table 4.2: L-edit color legend for Figures 4.4 and 4.5. Colors are listed in the order they were fabricated.

Color	Material	Layer
Orange	Gold	SRR and GND/VCC lines
Blue	Gold	Electrode
Red	Silicon Nitride	Dielectric
Checker	Gold	Anchor
Grey	Gold	Beam

Referring to Figure 4.4, the orange line on the left supplies ground to the outer and inner SRRs, and the orange line on the right supplies input voltage to electrodes. The lower gray line connects the lower cantilever array to the voltage line. The last layer (electroplated Au) was used to create a bias line for the lower cantilever array. A dielectric strip isolates the bias line from the outer ring. Figure 4.5 shows a close up view of the inset cantilevers from Figure 4.4 (in L-edit, the layers are transparent, therefore, bottom layers are visible).

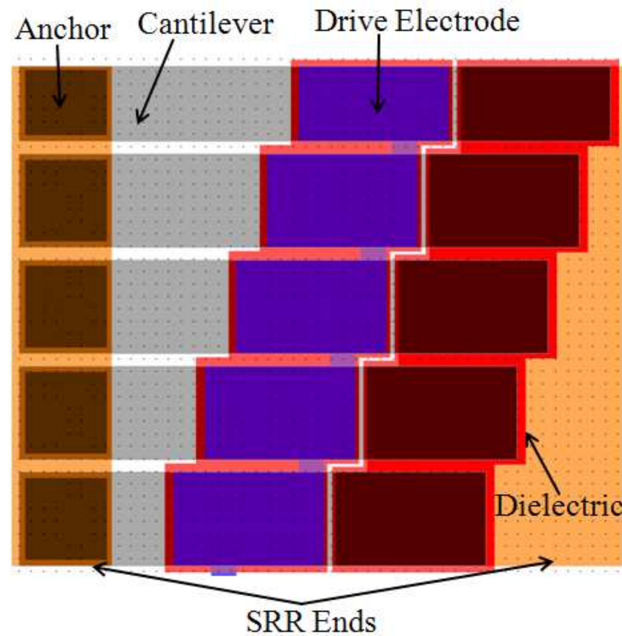

Figure 4.5: Close up view of cantilever array (inset from Figure 4.4).

After the SRR unit cell was created in L-Edit, the “Edit Object” feature was used to generate a 17 x 16 array of the SRR unit cells as shown in Figure 4.6. The

ground beams were then extended up and connected, and the voltage lines were extended down and connected to ensure all cantilever electrodes have the same voltage. This design used a large array of SRRs so that 6 x 1 strips of SRR unit cells could be diced if needed. Multiple stand-alone cantilever arrays and SRRs were designed for placement on the outer regions of the 3 inch wafer not taken up by the SRR array.

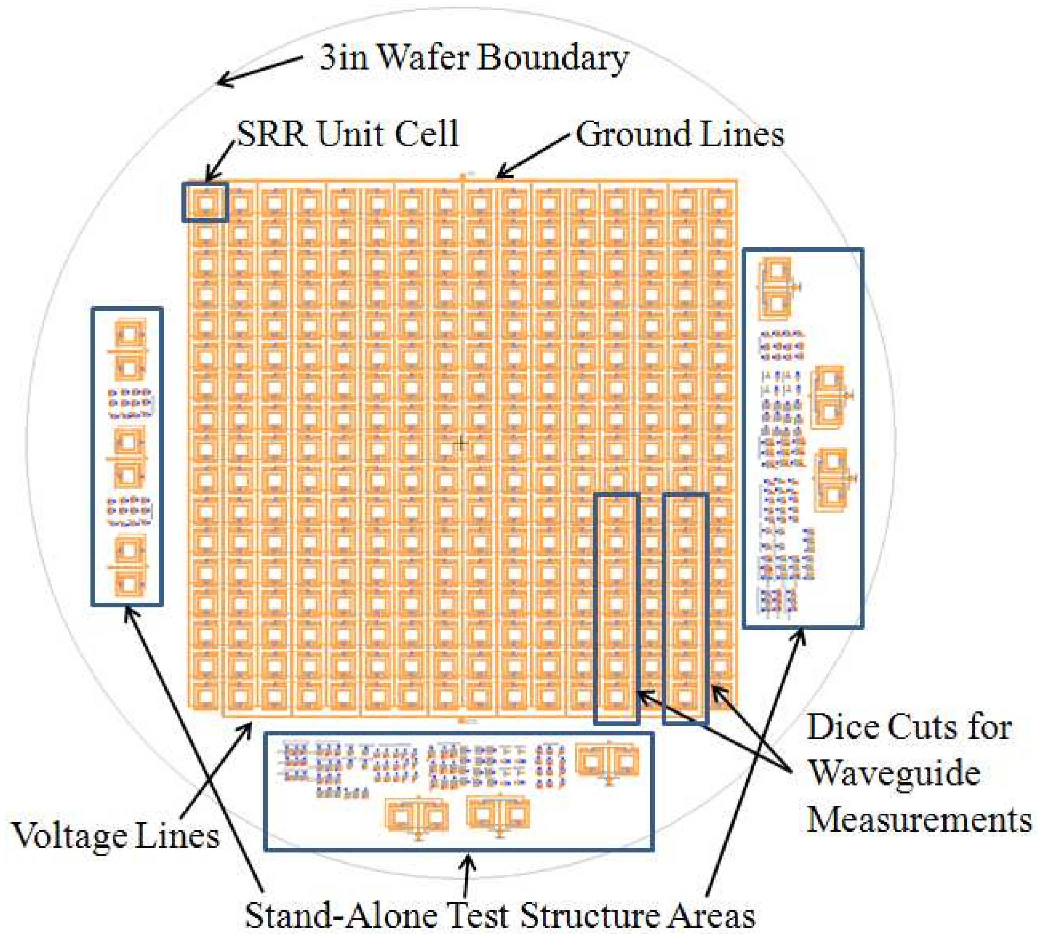

Figure 4.6: Final L-edit design layout for a 3 in wafer.

The main devices in the stand-alone test structure areas are multiple 300 – 400 μm cantilever arrays (as shown in Figure 4.7) which were designed for easy testing using the Zygo interferometer to record actuation voltage and out-of-plane beam bending.

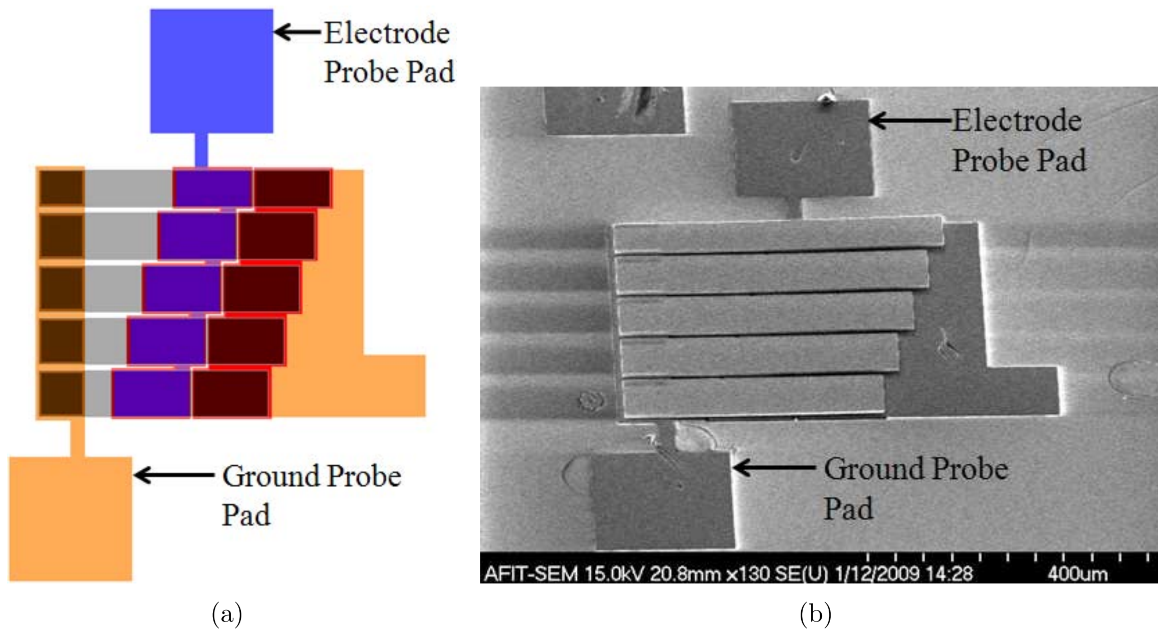

(a) (b)

Figure 4.7: $300 - 400$ μm cantilever array test structure designed in L-edit with large probe pads for easy test measurements (a) and a scanning electron microscope (SEM) image of the same device (b).

4.3 Fabrication

There are three main ways of fabricating MEMS structures: bulk micromachining, micromolding, and surface micromachining. Bulk micromachining is a process that removes "bulk" sections out of the substrate [18]. Micromolding such as LIGA (German acronym for LIthographie (lithography), Galvanoformung (electroplating), and Abformung (molding)) is a fabrication process that uses lithography, electroplating, and molding to create high-aspect-ratio metallic structures [18, 52].

Surface micromachining was used to fabricate the SRR and MEMS devices of this thesis. Surface micromachining is an additive process where materials (i.e., sacrificial layers, dielectrics, and metals) are deposited, patterned, and etched on top of a substrate. The MEMS device is "released" when the sacrificial layers are removed (by etching), leaving behind free standing mechanical structures [18, 20]. An example of a simple micromachining process flow is shown in Figure 4.8.

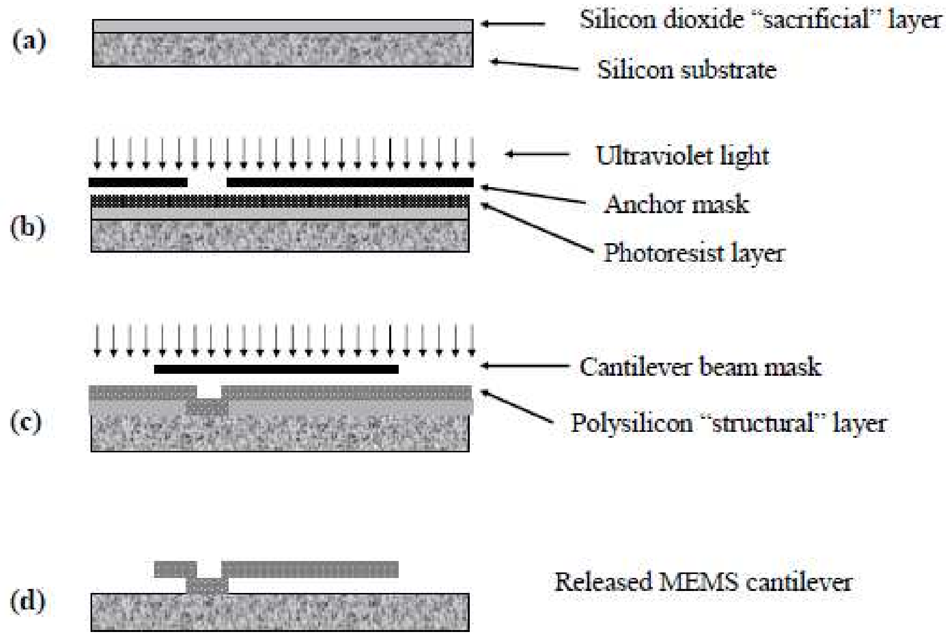

Figure 4.8: Example of a simple surface micromachining process flow for a cantilever beam [20].

When fabricating devices, compatibility of materials and etchants must be taken into account. For instance, titanium (Ti) structural layers are not compatible with the SiO_2 etchant, hydrofluoric acid (HF), which readily dissolves both SiO_2 and Ti. Deposition temperatures must also be compatible with the layers previously deposited.

A majority of conceptual MEMS devices are created with the PolyMUMPS™ [57], MetalMUMPS™, or SUMMIT foundry processes which offer consistent, working MEMS structures if minimum size rules are followed. The MEMS device of this project required a substrate–metal–dielectric–sacrificial layer–metal (bottom-to-top) layering, which the popular foundries do not provide (foundry fabrication steps cannot be conducted out of order). Also, a sapphire substrate is needed for its high resistivity (minimizes leakage current) and its dielectric properties (enables RF waveguide testing). The option of having sapphire as the substrate material is unavailable if using a foundry (PolyMUMPS™, MetalMUMPS™, etc.) for fabrication; the user has no control of substrate selection since multiple users share the same wafer (usually a silicon (Si) wafer). Instead, a custom process was developed to fabricate the MEMS

device with available facilities at AFIT and AFRL/RY. The specific fabrication procedures, however, still follow the generic surface micromachining process of starting with a base substrate and then building layers on top of each previous layer.

4.3.1 Custom Micromachining Process. The custom fabrication process used to create the devices in this study is shown in Figure 4.9, and is referred to for the following step-by-step fabrication discussion.

The custom process used in this design begins with a 0.5 mm- thick, 3 inch diameter, R-plane, highly resistive, sapphire wafer substrate. The base SRR layer was patterned using photolithography, then 200 Å of Ti followed by 5500 Å of Au were deposited using E-beam evaporation, the excess metal was then removed using a standard metal lift-off technique (a) [58–60] (the thin layer of Ti was evaporated prior to the Au deposit to facilitate Au adhesion to the sapphire substrate). Next, the 4500 Å-thick Au electrode with a 200 Å Ti adhesion layer was fabricated using the same evaporation and lift-off techniques (b). Next, 2000 Å of Si_3N_4 was deposited using plasma enhanced chemical vapor deposition (PECVD), patterned using photolithography, and then etched using reactive ion etching (RIE) (c). Next, two layers of MicroChem's polydimethylglutarimide (PMGI) based photoresist, SF-11 were deposited to form a 2 μm-thick beam gap (sacrificial layer) (d) [60]. Next, standard photolithography was used to pattern anchor points, the un-protected SF-11 was then exposed to deep ultra-violet (DUV) and developed (e). Next, the wafer was baked on a hot plate set at 270° C to re-flow and round off the $\angle 90°$ cantilever hinges (f). A 200 Å-thick seed layer of Ti followed by 1000 Å of Au was then sputtered on the entire wafer surface (g). Next, standard photolithography was used to pattern the cantilever beam. The wafer was then put into a Au electroplating bath to electroplate 5 μm of Au (h). Finally, the cantilever devices were released by stripping the PMGI sacrificial layer with 1165 Stripper followed by four isopropyl baths and four methanol baths and then dried using a CO_2 critical point dryer (i).

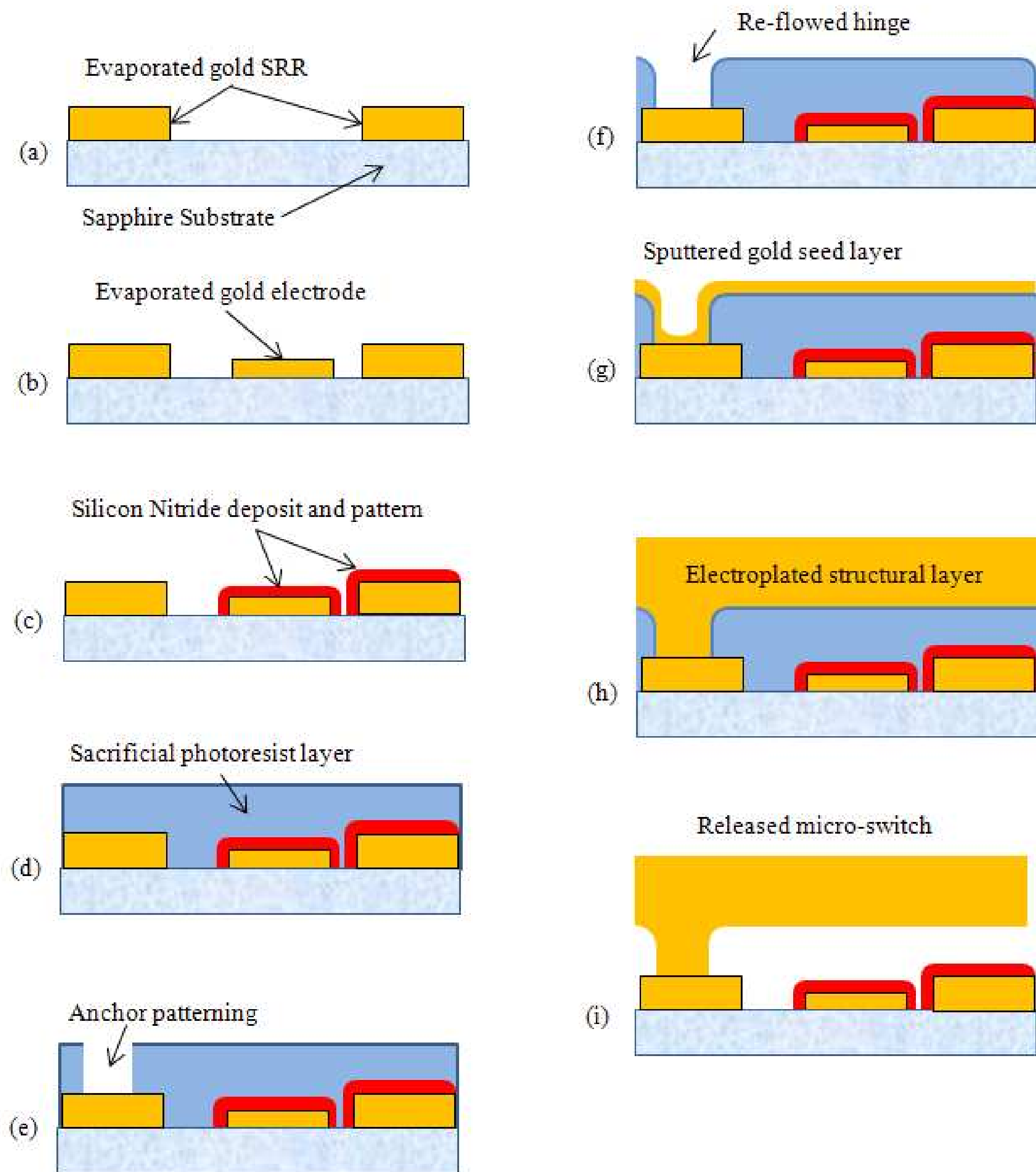

Figure 4.9: Illustration of custom fabrication process.

Nine wafers were created during the fabrication phase of this project. The wafers were identified by their material and by the order they were fabricated, for example, the first silicon wafer was identified as SiW1 (silicon wafer one). Three silicon wafers (SiW1 – SiW3) were fabricated to define process parameters, such as spin speeds,

exposure times, developing times, bake temperatures, etc. Two quartz wafers (QtzW1 and QtzW2) and four sapphire wafers (SaW1 – SaW4) were created for device testing, however, of the six wafers, only two wafers produced testable devices: SaW3 and SaW4 (QtzW1 broke, and the beams on QtzW2, SaW1, and SaW2 curled up from tensile stress). Table 4.3 summarizes the actions, materials, and layer thicknesses (for SaW3 and SaW4) of the custom fabrication process. The detailed process followers (step-by-step instructions) used for fabrication are shown in Appendix 1.

Table 4.3: Summary of custom fabrication process with deposition thicknesses for SaW3 and SaW4.

				Thicknesses (μm) for:	
Step	Action	Material	Layer/Mask Name	SaW3	SaW4
N/A	Clean	Sapphire	Substrate	500	500
a	Deposit	Ti	Adhesion Layer	0.02	0.02
	Deposit	Au	SRR	0.75	0.55
b	Deposit	Ti	Adhesion Layer	0.02	0.02
	Deposit	Au	Electrode	0.5	0.45
c	Deposit	Si_3N_4	Dielectric	0.15	0.2
d	Deposit	PMGI	Sacrificial Layer	2.0	2.0
e	Etch	PMGI	Anchor	2.0	2.0
f	Re-flow	PMGI	N/A	N/A	N/A
g	Deposit	Au	Beam Seed Layer	0.1	0.1
h	Deposit	Au	Beam Structure	8.0	5.0
i	Release	PMGI	N/A	2.0	2.0

4.3.2 Fabrication Challenges.

4.3.2.1 SF-11 Sacrificial Layer. Microchem reports that SF-11 becomes a planar layer after it is soft-baked to 275° C as shown in Figure 4.10. Microchem did not supply a re-flow time, therefore, 4 min was used according to Coutu's process follower [20]. After re-flow, the SF-11 layer was measured with a Tencor profilometer, which showed that the layer was not becoming planar, and was still conformal (even after multiple re-flow attempts). Re-flow attempts failed most likely because of insufficient soft-bake time.

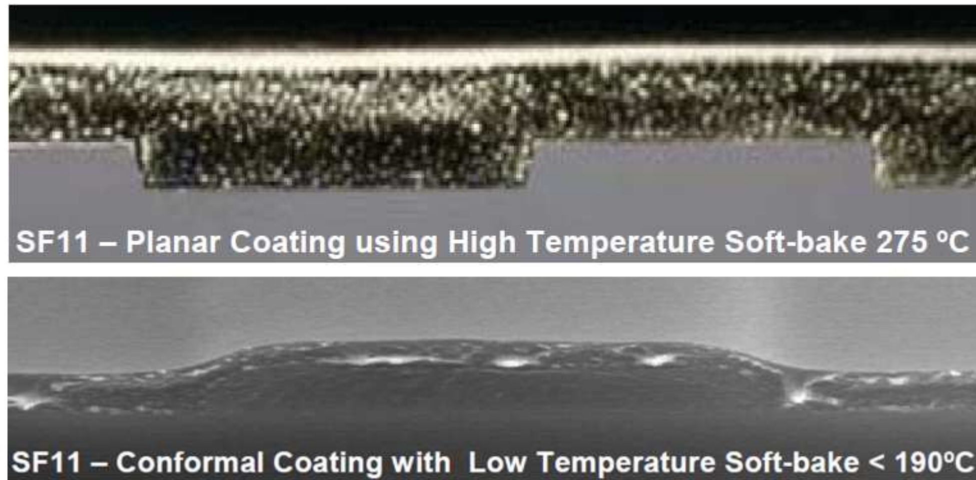

Figure 4.10: SF-11 planar coating and conformal coating ability [60].

4.3.2.2 Electroplating. When different layers with dissimilar coefficient's of thermal expansion are deposited on each-other during micromachining, they deform under tensile or compressive stress as shown in Figure 4.11.

Figure 4.11: Diagram of tensile (a) and compressive (b) stresses on two layers with different coefficient's of thermal expansion [56].

The cantilevers in this study have three layers: a 200 Å Ti adhesion layer (etched during release process) a 1000 Å Au seed layer followed by $5 - 8$ μm of electroplated gold. The electroplated cantilever beams on three wafers (QtzW2, SaW1, and SaW2) curled up as shown in Figure 4.12 after the release step, indicating that a tensile stress is in the electroplated Au. Current density settings and deposition thicknesses were adjusted for the next two sample wafers (SaW3 and SaW4), the results of which are shown in Figure 4.13. Increasing the electroplater current density and the thickness of the Au resulted in cantilevers with lower tensile stress, which produced working devices.

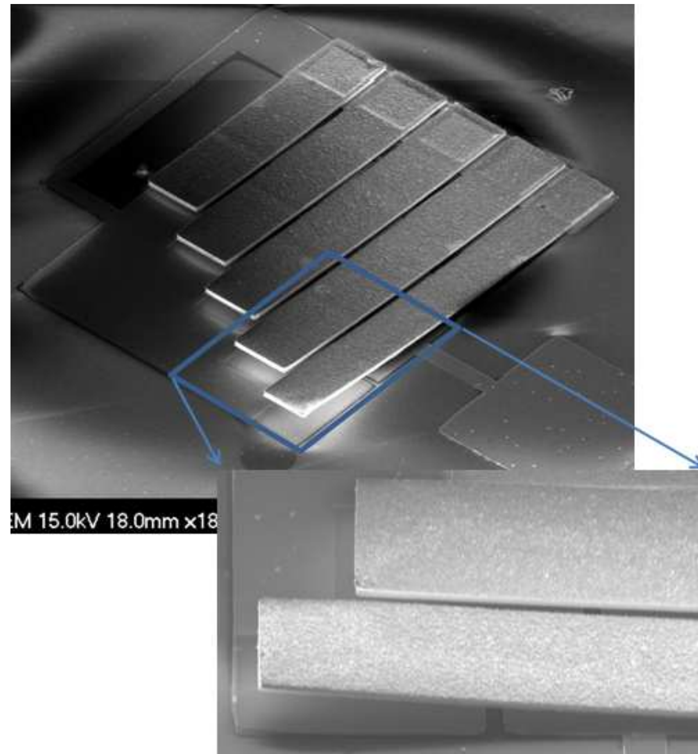

Figure 4.12: SEM image showing cantilever beam curling up more than 20 μm due to tensile stress introduced during the electroplating process.

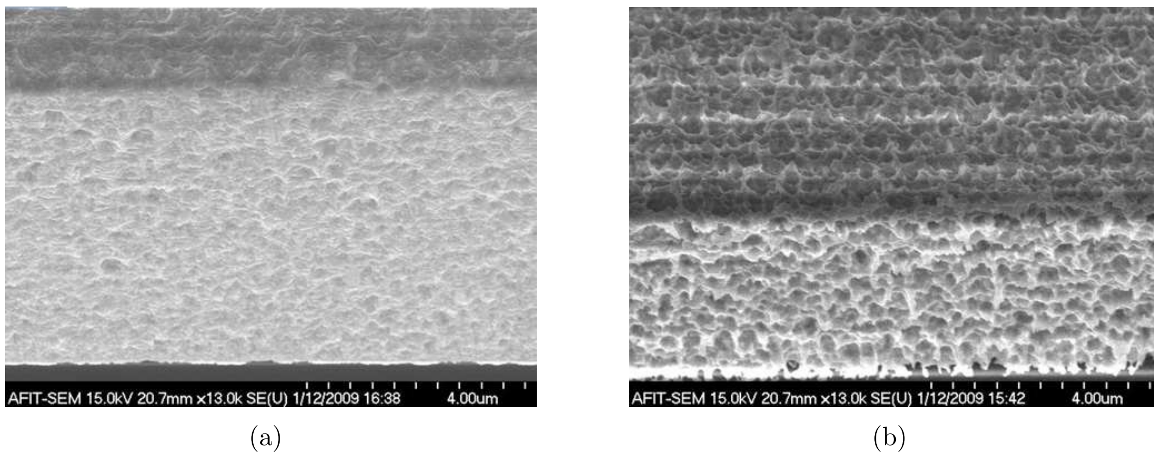

(a) (b)

Figure 4.13: SEM image showing cantilever beams electroplated with different current density settings. SaW3 was electroplated with an average current of 6 mA which produced a solid beam (a) and SaW4 was electroplated with an average current of 12 mA which produced a beam with voids throughout the material (b). The SaW4 cantilevers deflected less and actuated at a lower voltage than cantilevers from SaW3 (brighter sections are the sides and darker sections are the tops of the beams).

4.3.2.3 Tousimis Autosamdri Critical Point Drier Failure. The four-inch Tousimis Autosamdri critical point drier at AFRL failed to reach the temperature and pressure needed to start the critical point drying process, therefore, the SRR array had to be diced in smaller than desired pieces to fit into AFIT's one-inch critical point drier.

4.3.2.4 Beam Metal Surface Roughness. As shown in Figure 4.14, the bottom side of the cantilever beam (Au sputtered seed layer) is not a perfectly smooth surface. The surface roughness reduces the contact surface area which decreases overall capacitance.

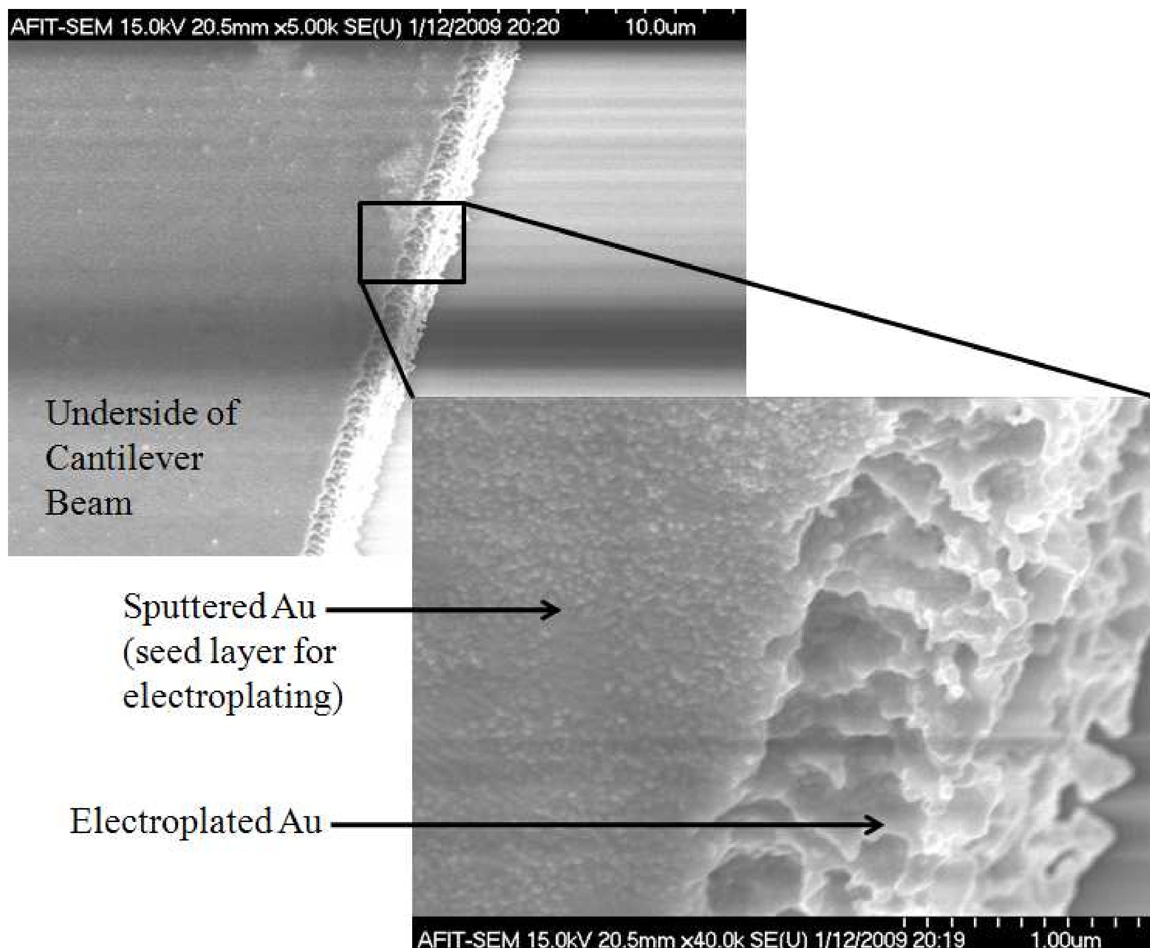

Figure 4.14: SEM image showing surface roughness on the underside of a cantilever beam (cantilever beam was bent back with a probe for illustration purpose).

4.4 Chapter Summary

This chapter discussed in detail the cantilever array, SRR structure, test-structure designs, and the fabrication process used to create them. The issues encountered during the fabrication process were also presented. However, there is still a significant deflection in wafers SaW3 and SaW4, therefore, an intensive Au electroplating study (out of the scope of this project) is needed to determine the optimal machine settings (i.e., current density, temperature, duty cycle) used for depositing Au with the least amount of tensile stress. For a comprehensive review of the fabrication process, refer to the process followers in Appendix 1. The next chapter combines the theory and design of the cantilever array and applies it to the modeling and simulation of cantilever actuation.

V. Analytic Predictions, Modeling, and Simulation

5.1 Chapter Overview

This chapter presents analytical predictions of cantilever beam behavior based on beam theory introduced in Chapter 3. This chapter also includes the modeling and simulation results of the capacitive cantilever design discussed in Chapter 4 to compare with the analytical predictions. Comsol electromagnetic simulations are also provided.

5.2 Analytic Predictions

Pull-in voltage, capacitance, collapse voltage, and release voltage are calculated using cantilever dimensions from fabricated test structures (SaW3 and SaW4) and equations from Chapter 3.

5.2.1 Pull-in Voltage.

Multiple pull-in voltages were calculated using Equation 3.14 with three different spring constant values:

1. a simple spring constant equation from Coutu et al. [16]
2. a modified spring constant to account for electrode position under cantilever (Equation 3.5)
3. a modified spring constant that accounts for electrode position and post height (Equation 3.7)

The pull-in voltage calculations conducted for SaW3 and SaW4 are shown in Figure 5.1 and Figure 5.2, respectively (note: an extra calculation using Luo's pull-in equation is also included [40]).

Analytic calculations confirm that the longest cantilever pulls-in first followed by the next longest beam. The spring constant selected for use in the pull-in equation has a significant impact on the calculated pull-in voltage. Meng's equation, which accounts for electrode position and beam height, theoretically provides the most accurate model for this study.

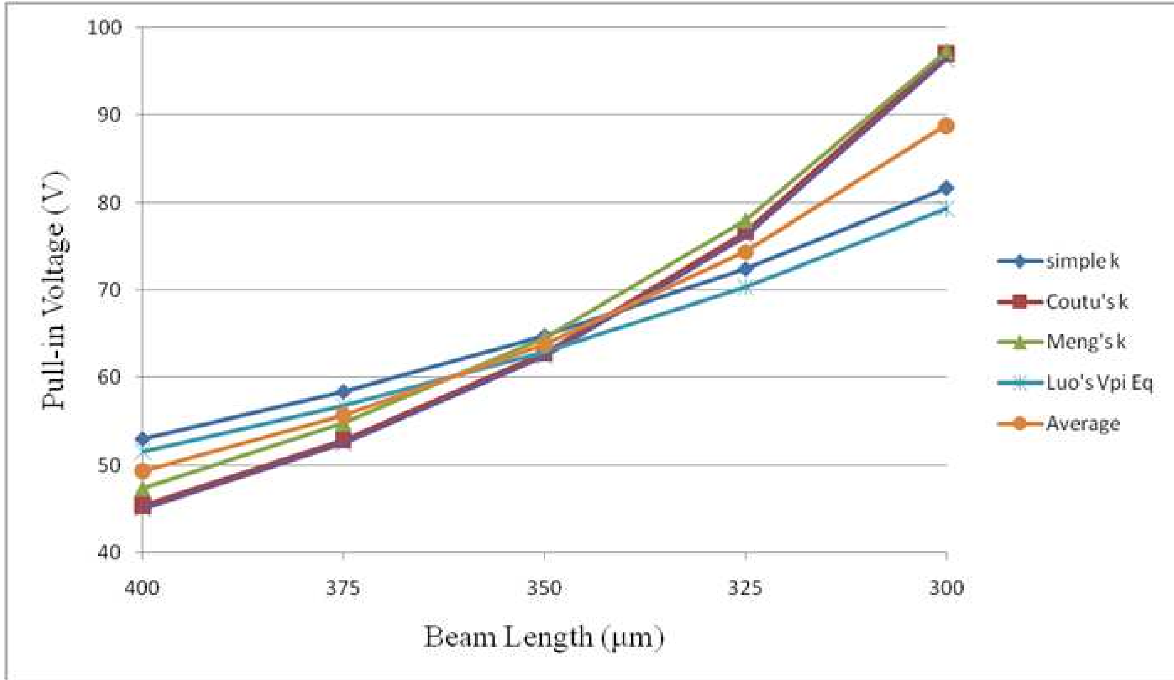

Figure 5.1: Calculated pull-in voltages vs. beam length for SaW3 ($t_b = 8$ μm).

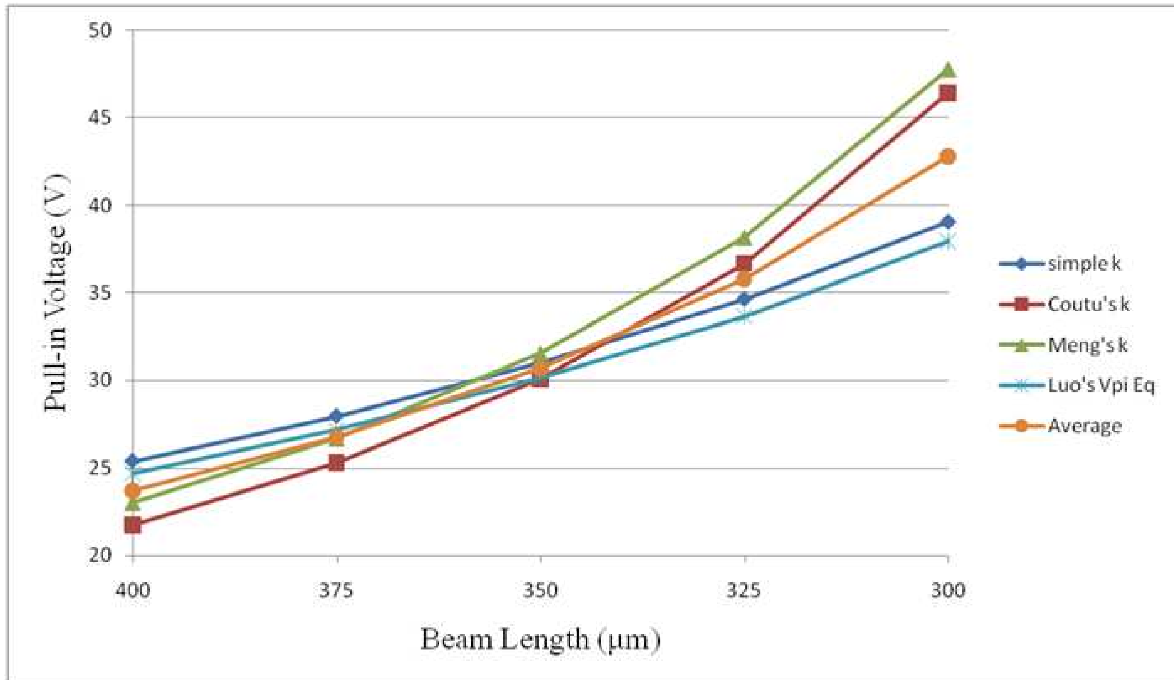

Figure 5.2: Calculated pull-in voltages vs. beam length for SaW4 ($t_b = 5$ μm).

5.2.2 Capacitance. When a beam is pulled-in, it increases the capacitance of the device. The capacitance contributed by each cantilever pulling-in was calculated using Equation 2.6 and then plotted in Figure 5.3 along with the corresponding cantilever's average pull-in voltage. This C–V curve is created with the assumption that total potential cantilever capacitance is reached at pull-in (assumes beam and dielectric are perfectly flat and make full contact). Each data point represents a cantilever snapping down at a corresponding pull-in voltage.

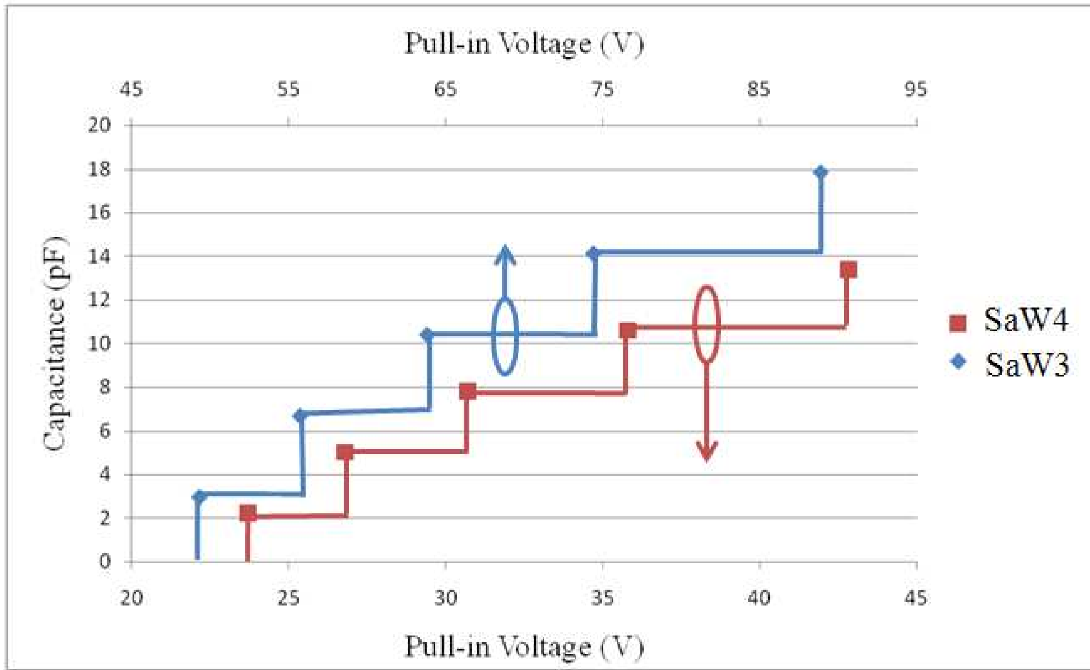

Figure 5.3: Capacitance vs. average pull-in voltage for multi-cantilever array.

5.2.3 Collapse Voltage. Collapse voltages were calculated for SaW3 and SaW4 using Equation 3.19 and are shown in Table 5.1. The cantilever array was designed so that all five cantilevers would actuate before the longest beam collapses (i.e., the V_{pi} of the 300 μm beam should be less than the V_{cpi} of the 400 μm beam). After comparing the collapse voltages in Table 5.1 to the pull-in voltages in Figures 5.1 and 5.2, all SaW3 cantilevers actuate before any collapse, however, SaW4's 400 μm beam could possibly collapse before all beams pull-in (depends on spring constant).

Table 5.1: Calculated collapse voltages for cantilevers on SaW3 and SaW4.

	Collapse voltages (V), V_{cpi}, for:	
Beam length (μm)	SaW3	SaW4
400	99.08	39.03
375	111.83	44.05
350	129.1	50.86
325	153.78	60.58
300	191.69	75.52

5.2.4 Release Voltage. Release voltages were calculated for SaW3 and SaW4 using Equation 3.20 and are shown in Table 5.2.

Table 5.2: Calculated release voltages for cantilevers on SaW3 and SaW4.

	Release voltage (V), V_r for:	
Beam length (μm)	SaW3	SaW4
400	4.19	1.24
375	4.85	1.43
350	5.72	1.69
325	6.91	2.05
300	8.61	2.57

5.3 Finite Element Modeling and Simulation

CoventorWare® (a finite element modeling (FEM) software program [61]) was also used to predict beam pull-in voltages. First, the cantilever array design was constructed in L-edit (recall Chapter 4, Figure 4.5) and then imported into CoventorWare®. Next, a custom fabrication process (shown in Figure 5.4) was developed using the Process Editor in CoventorWare® to construct a solid model of the cantilever beam array (Figure 5.5) out of the imported L-edit design. For simplicity, the substrate and SRR base were hidden from the mesh model, and the cantilever array was partitioned into separate beams to decrease computer process time. The solid model was then meshed using "Manhattan brick" mesher settings as shown in Figure 5.5. Small brick sizes were used in the mesher settings to ensure accurate simulation results. The anchored

end of the cantilever was designated as a "fixed-end patch" so the computer model would treat the beam as a fixed-end/free-end beam.

Number	Step Name	Layer Name	Material Name	Thickness	Mask Name	Photoresist	Comments
0	Substrate	Substrate	Sapphire	500	SubstrateMask		
1	E-beam Evaporation	Layer1	GOLD	0.75			SRR Base
2	Straight Cut				L13D0	+	
3	E-beam Evaporation	Layer1	GOLD	0.5			SRR ground plate
4	Straight Cut				L51D0	+	
5	LPCVD	Layer2	SI3N4	0.15			
6	Straight Cut				L45D0	+	
7	Planar Fill of Sacrificial Layer	Layer4	POLYIMIDE	2			SF-11 sacrificial layer
8	Etch Anchors for bridge				L43D0	-	Etching post holes
9	Sputter then Electroplate	Layer5	GOLD	8			cantilever electroplated
10	Straight Cut				L49D0	+	forms cantilevers
11	Release Wet Etch		POLYIMIDE				Release cantilever beams

Figure 5.4: Screenshot showing summary of custom fabrication process created in the Process Editor of CoventorWare®.

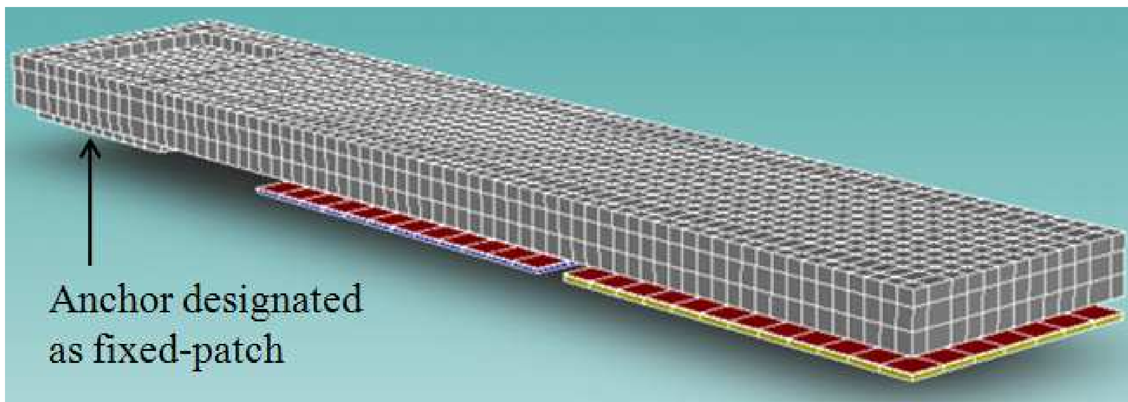

Figure 5.5: Meshed cantilever in CoventorWare®.

CoventorWare®'s analyzer tool, CoSolveEm, was then used to electromechanically simulate the meshed cantilever beam model. The cantilever beam was fixed at 0 V, and the applied voltage on the electrode was set as a trajectory over a range of voltages. The voltage range for each cantilever beam was specifically selected so results would include pull-in, zipper effect, and collapse. All modeled beams ($300 - 400$ μm) behaved the same mechanically, therefore, CoSolveEm beam results are shown generically in Figure 5.6.

The simulation results for a 300 μm beam from SaW3 are shown in Table 5.3. The results show the beam pulling down as voltage increased, however, no snap-

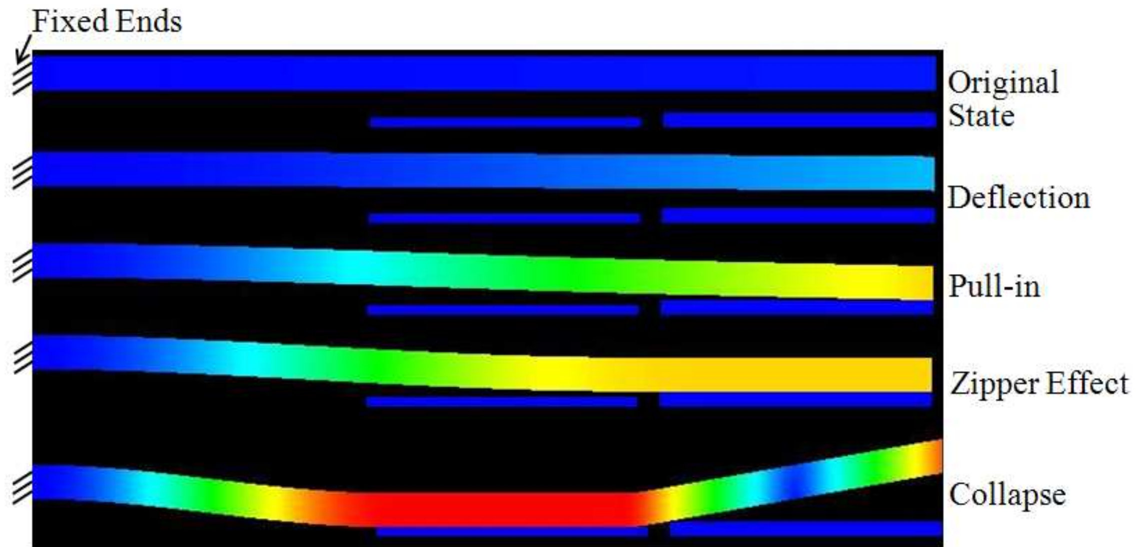

Figure 5.6: Generic FEM analysis of cantilever. The colors represent displacement magnitude; blue = no deflection, orange = 2 μm deflection, and red = max deflection of $2.1 - 2.2$ μm (depending on which fabrication dimensions are used).

down is observed at one-third of the gap deflection. One-third of the gap for the simulated cantilever is 0.73 μm, which according to Table 5.3, would put the pull-in

Table 5.3: CoventorWare® simulation results for displacement and capacitance of a 300 μm cantilever (using SaW3 dimensions).

Voltage (V)	Displacement (μm)	Capacitance (pF)
0	0.058	0.083
95	0.602	0.099
100	0.693	0.102
102	0.734	0.103
104	0.776	0.105
106	0.822	0.107
110	0.922	0.111
112	0.978	0.114
114	1.038	0.117
116	1.104	0.120
120	1.260	0.130
122	1.355	0.138
124	1.471	0.149
126	1.624	0.169
128	1.922	0.269
130	2.001	0.396

voltage between $100 - 102$ V, which agrees with analytical calculations in Figure 5.1. However, instead of deflecting to 2 μm at 104 V, the simulator continues with a gradual deflection until pull-in is reached at 130 V–well past the calculated value of pull-in voltage.

5.4 Results Comparison

The CoventorWare® simulated pull-in voltages for a cantilever array (Table 5.4) do not agree with the analytically calculated pull-in results shown in Figure 5.1.

Table 5.4: CoventorWare® simulation results for pull-in voltage of a cantilever array (using SaW3 dimensions).

Beam Length (μm)	Pull-in Voltage (V)
400	58
375	60
350	90
325	98
300	130

Deviation between analytical and simulated analysis is most likely due to assuming a point source load in the analytical calculations. In reality, the electrode exerts a distributed force on the cantilever beam. Also, the spring constant in Equation (3.5) was calculated using a point source force, F_a, located at position a, and a deflection, d, located at position L_b. However, according to [49], all variables from Equation (3.5) must be located at the same position. Another factor contributing to simulation error is residual stress. The residual stress of the beam is not taken into account using current analytical models. Further analytic modeling of the beam is necessary to develop a more accurate prediction of device operation.

5.5 SRR Comsol Simulations

S-parameter simulations were performed on a unit cell with the SRR geometry shown in Figure 1.1. Periodic boundary conditions were used to simulate an array of unit cells. Effective permeability was extracted from the S-parameter measurements.

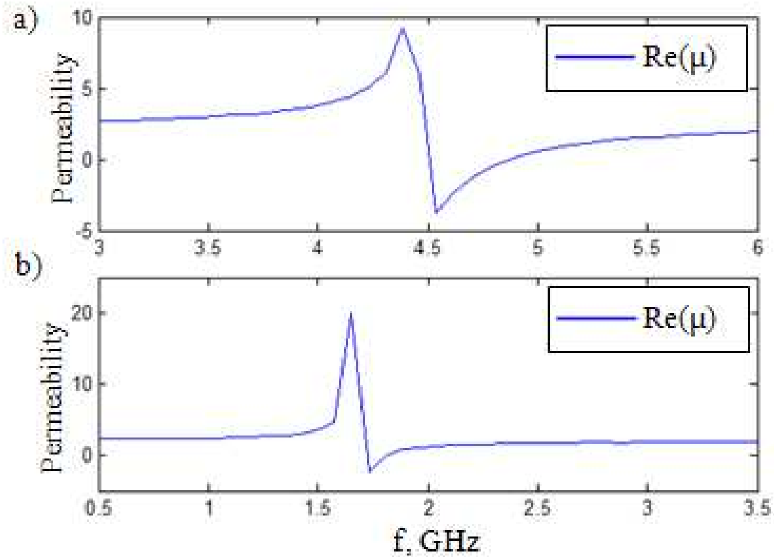

Figure 5.7: Permeability of a simulated SRR with MEMS devices in the up-state (a) and with one beam in the down-state (b). Note the shift in resonant frequency ($\mu < 0$).

The capacitance of the unit cell was changed by altering the permittivity in the gaps between the split ends. While this simulation does not simulate the actual MEMS structure, it does simulate the effects which should be induced. Figure 5.7(a) shows the retrieved permeability with an effective gap capacitance when all cantilevers are in the up-state, and Figure 5.7(b) shows the retrieved permeability when one cantilever is in the down-state.

5.6 Chapter Summary

This chapter presented the analytical predictions of cantilever beam behavior. Values for pull-in voltage, capacitance, collapse voltage, and release voltage were given, however, values for predicted voltages are significantly influenced by the spring constant models. CoventorWare® was also used to predict pull-in voltage, however, the software is not programmed to show snap-down occurring at one-third the gap, therefore, CoventorWare® modeled pull-in voltages is higher than expected. The next chapter presents the results of testing conducted on the cantilever array test devices.

VI. Experiments and Test Results

6.1 Chapter Overview

This chapter presents the results (i.e., pull-in voltage, release voltage, capacitance, and limited lifetime test) from testing conducted on the cantilever array test devices.

6.2 Pull-in Voltage Measurements

6.2.1 Experiment Test Setup. As shown in Figure 6.1, a Zygo interferometric microscope, power supply, and voltmeter were used to test the pull-in voltage of a standard $300 - 400$ μm cantilever array test structure. Micromanipulator probes were used to connect DC voltage to bond pads. Voltage was then applied and deflection was observed on the Zygo monitor. The voltage reading on the voltmeter was recorded at each beam pull-in. Testing was attempted on previous fabrication runs (QtzW2, SaW1, and SaW2), however, as shown in Figure 6.2, the cantilever beams were curled up to nearly 19 μm. Slight deflection was observed as voltage was applied, but even at maximum power source voltage (200 V), pull-in was not achieved. Note that a

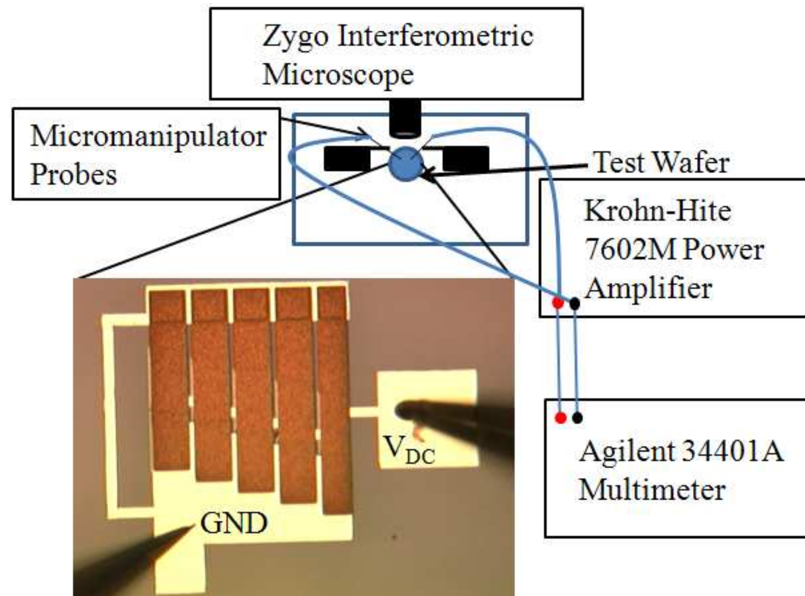

Figure 6.1: Schematic illustration of the experimental test setup used to actuate cantilevers and measure resulting deflection.

device actuating past the dielectric breakdown (100 V) instantaneously shorts out and destroys the device.

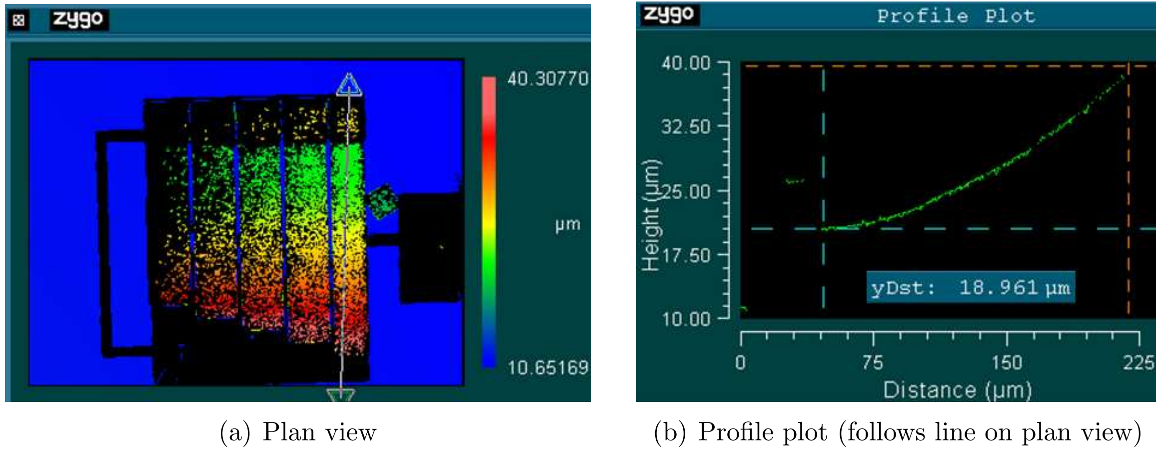

(a) Plan view (b) Profile plot (follows line on plan view)

Figure 6.2: Zygo interferometer measurement of SaW2. Beams are deflected up by 19 μm due to residual stress introduced during electroplating. Beams were deflected too high to be pulled-in. yDst in (b) is the height difference between the two inspection points. Data drop-out is due to the rough surface of the electroplated Au, which scatters light.

Pull-in voltage tests were accomplished on SaW4 devices. The beams on SaW4 had the least amount of tensile stress compared to previous test wafers as shown in Figure 6.3, and they were able to actuate below dielectric breakdown voltage (100 V).

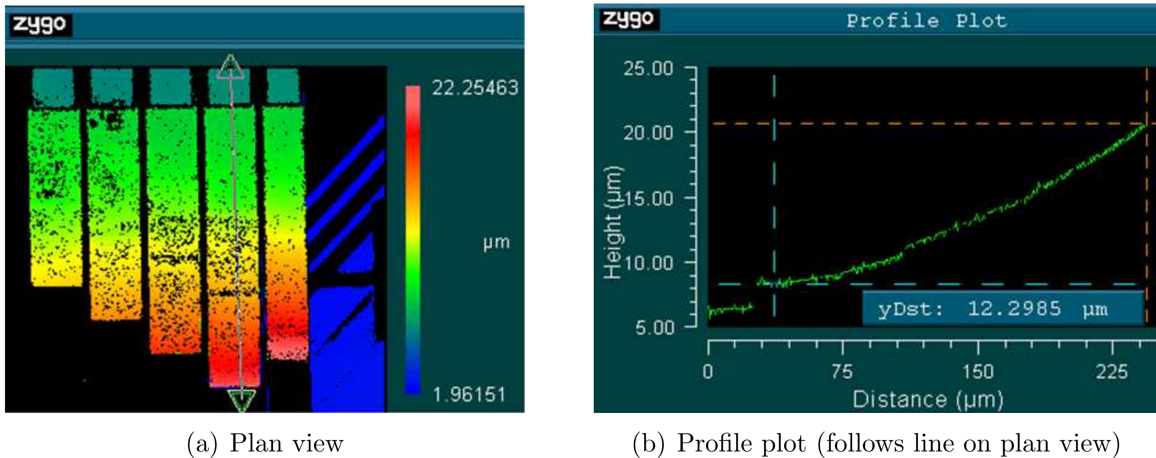

(a) Plan view (b) Profile plot (follows line on plan view)

Figure 6.3: Zygo interferometer measurement of SaW4 cantilever array in the up-state. The 400 μm beam appears short because it deflects beyond the range of measurement. SaW4 beams had the least amount of tensile stress of all test wafers.

6.2.2 Pull-in Voltage Results. During the first time testing, beams would pull-in, however, they either remained stuck as shown in Figure 6.4 (testing data example in Table 6.1) or the dielectric broke down at a lower voltage than the expected voltage of 100 V as shown in Figure 6.5 (testing data example in Table 6.2). Stiction occurred on most cantilevers most likely due to humidity in the characterization lab or from organic material not removed during the release process. However, beams that did not remain stuck when voltage was removed continued to actuate without failure. The test structures where V_{br} occurred could not be tested further because the breakdown created a shorted path between the cantilever and landing pad.

Table 6.1: Initial SaW4 cantilever array test results with stiction issues.

Beam Length (μm)	V_{pi} (V)	V_r (V)
400	49.7	stuck
375	48.3	stuck
350	52.1	25.8
325	59.5	47.4
300	71.1	stuck

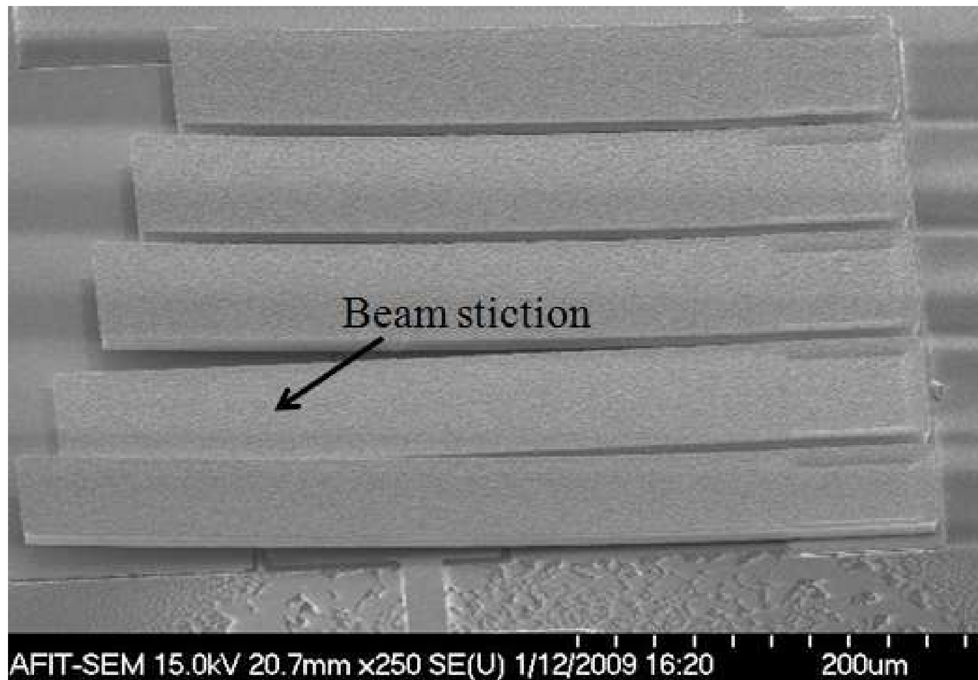

Figure 6.4: SEM image of a cantilever stuck in the down-state.

Table 6.2: Initial SaW4 cantilever array test results with dielectric breakdown issues.

Beam Length (μm)	V_{pi} (V)
400	51.7
375	49
350	53.6
325	V_{br} @ 70
300	N/A

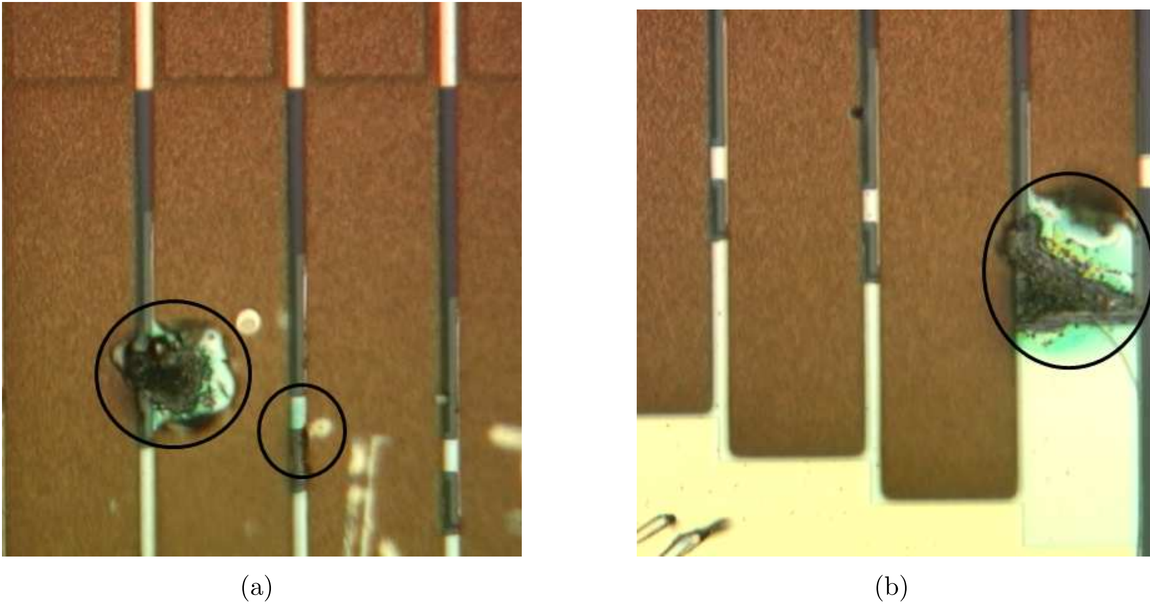

(a) (b)

Figure 6.5: Image of test device failure due to dielectric breakdown (circled).

After encountering multiple breakdown and stiction failures using different test devices, the wafer pieces were plasma ashed at 150 W for 30 minutes to remove any organic or moisture residue that could cause stiction. Test devices adjacent to the failed devices on SaW4 were then subjected to the same experiment. A test device was actuated through multiple pull-in/release cycles; the results are shown in Figures 6.6(a) and (b). A zygo interferometer measurement was taken post-ashing, and it was observed that the beams had deflected more, which explains why pull-in voltage increased after plasma ashing. Regardless of the increased deflection, the post-ashed devices pulled-in and demonstrated no stiction issues and few dielectric breakdown instances. Therefore, the ashing step removes any contaminants that cause

stiction, however, it also removes a combination of a thin layer of Au and organic material lodged in the crevices of the electroplated Au (large crevices are shown in Figure 4.13); both of which decrease the spring constant of the beam causing an increased deflection.

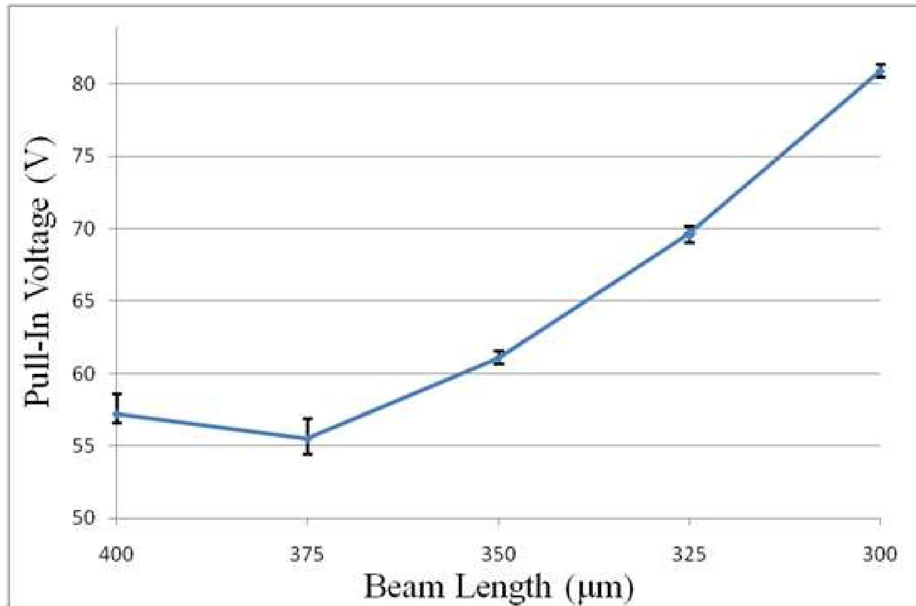

(a)

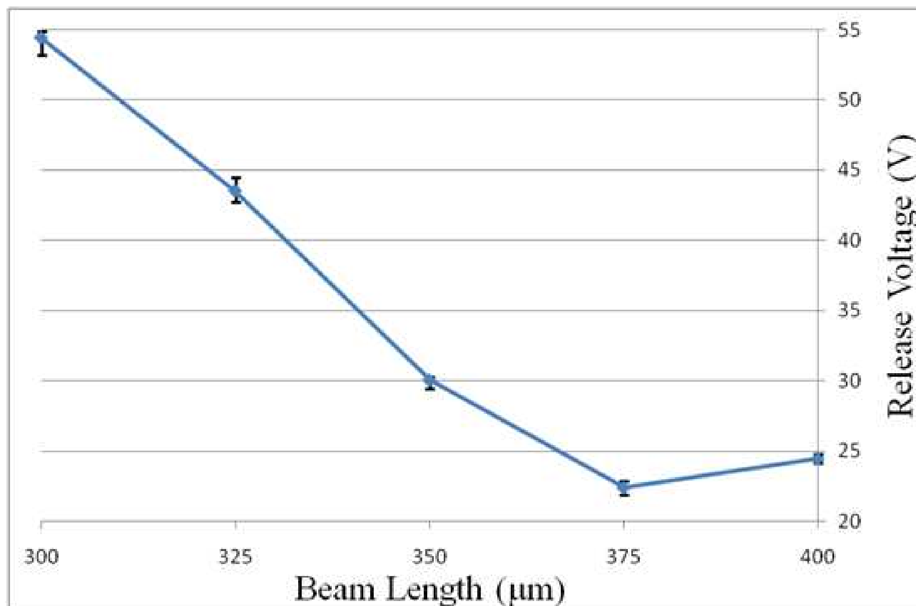

(b)

Figure 6.6: Pull-in (a) and release (b) voltage results for a SaW4 cantilever array.

As shown in Figure 6.6(a), the first beam that pulls-in is the 375 μm beam instead of the 400 μm beam. This occurs because the 400 μm beam is not as wide (60 μm instead of 75 μm) as the other beams and it subsequently has a lower material spring constant. A beam with a higher spring constant resists curve deflection caused by tensile stress, therefore the 400 μm beam curls up more than the other beams. Since the 400 μm beam has a steeper curve, it requires more voltage to pull it down, which is why it pulls-down out of sequence. The test device structure, however, still demonstrates a one-at-a-time actuation scheme, which satisfies the design requirement.

The beams also release one-at-a-time as shown in Figure 6.6(b). The release voltage is higher than expected due to the tensile stress deflection. The curling of the beam caused by the tensile stress is a plastic deformation which increases the mechanical restoring force, therefore, the beams release at a much higher voltage than if they were flat beams. Again, the 400 μm beam releases out of sequence because it has a higher tensile stress gradient than the other beams.

Table 6.3 shows the calculated pull-in voltages and tested pull-in voltages for comparison. The cantilever devices actuated at nearly twice their respective calculated values, however, this was expected since the cantilever beams were not perfectly flat. The deflection due to tensile stress is measured from the beginning of the beam to the tip of its free-end. The gap between the cantilever beam and electrode, g_0, is not increased by the full deflection amount, rather, it is increased by a quarter of the tensile stress deflection.

6.2.3 Collapse Issues During Pull-in Voltage Tests. First, a Zygo interferometer measurement was taken of all beams in the up-state as shown in Figure 6.3. Voltage was then applied to the actuation electrode and increased to the point where the first beam pulled-in. A measurement was then taken with the Zygo and is shown in Figure 6.7. The profile plot (Figure 6.7(b)) displays that the middle of the beam has collapsed onto the electrode and the end of the beam has been deflected upwards

Table 6.3: Comparison of calculated and tested pull-in voltages for a SaW4 cantilever array.

Beam Length (μm)	Calculated V_{pi} (V)	Ave. Tested V_{pi} (V)	Measured Deflection due to Tensile Stress (μm)
400	23.7	57.2	8.6
375	26.8	55.5	7.4
350	30.7	61.1	6.2
325	35.8	69.7	5.7
300	42.8	80.9	4.3

(recall the profile plot is similar to the collapsed beam simulation shown in Figure 5.6). Similar measurements were taken on pulled-in beams of multiple test devices. The multiple measurements confirm that the cantilever beams are instantaneously collapsing at pull-in. The beams are collapsing at pull-in because they were not designed to actuate at high voltages—meaning the pull-in voltage of a curled beam is higher than the collapse voltage of a flat beam with the same dimensions as shown in Table 6.4.

Table 6.4: Comparison of calculated collapse voltages and measured pull-in voltages for a SaW4 cantilever array. Pull-in voltages are greater than collapse voltages, which means the cantilever instantaneously collapses at pull-in.

Beam Length (μm)	Calculated V_{cpi} (V)	Ave. Tested V_{pi} (V)
400	39	57.2
375	44	55.5
350	50.9	61.1
325	60.6	69.7
300	75.5	80.9

Another possible contributing factor causing instantaneous beam collapse, is the way a curved beam pulls-in as shown in Figure 6.8. If the beam has a high curvature, then the middle of the beam contacts the electrode first, and would do so even if the pull-in voltage did not exceed the collapse voltage.

After the beam pulled-in, voltage was reduced to the point just before beam release and a Zygo measurement was taken as shown in Figure 6.9. A comparison of the profile plots in Figures 6.7 and 6.9 indicates that the beam slightly lifts off the

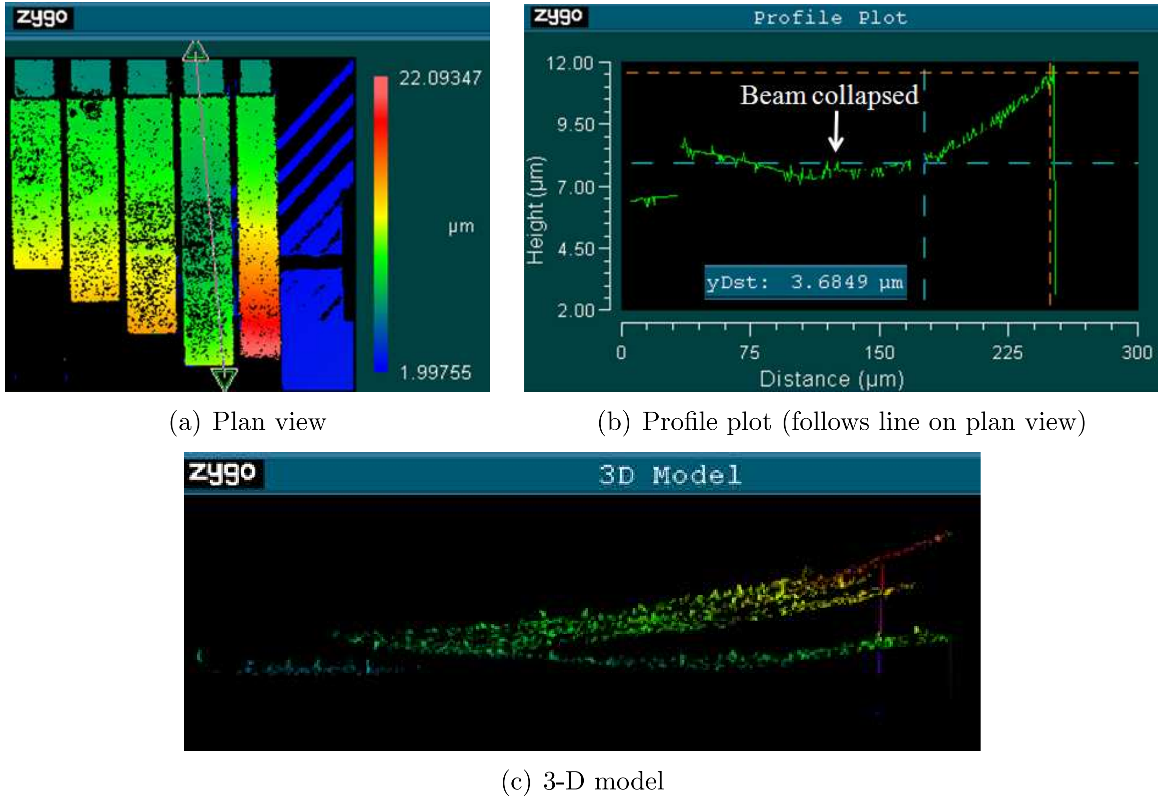

(a) Plan view

(b) Profile plot (follows line on plan view)

(c) 3-D model

Figure 6.7: Zygo interferometer measurement of cantilever array with one beam pulled-in. The cantilever beam is instantly collapsing onto the electrode at pull-in.

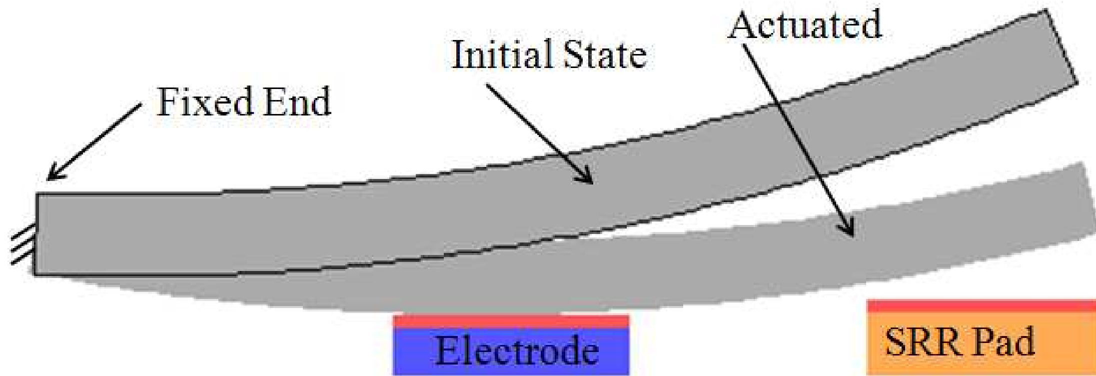

Figure 6.8: Actuation of a curved beam. The curvature of the beam causes the beam to land on the lower electrode pad before the SRR pad.

electrode when the voltage is reduced, but the electrostatic attraction is still strong enough to keep the beam in the down-state. This test demonstrates that there is contact being made between the beam and SRR landing pad.

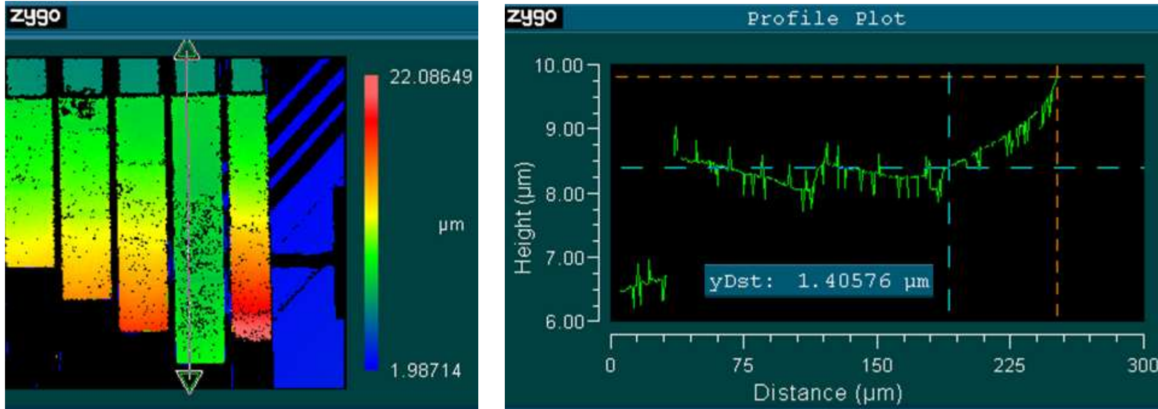

(a) Plan view (b) Profile plot (follows line on plan view)

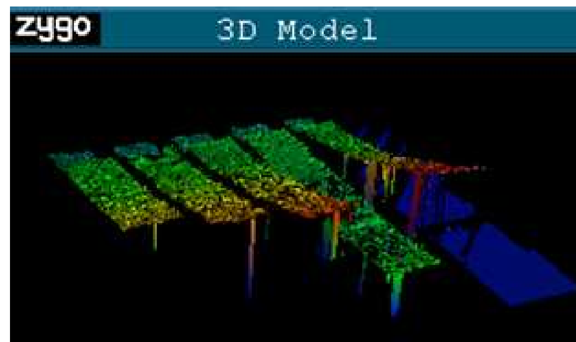

(c) 3-D model

Figure 6.9: Zygo interferometer measurement of cantilever array with one beam pulled-in with actuation voltage reduced to the point just before beam release. The beam has pulled up slightly and is not as collapsed as it was at pull-in (Figure 6.7(b)).

6.3 Capacitance Measurements

6.3.1 Experiment Test Setup. As shown in Figure 6.10, an Agilent 4284A Precision LCR (Inductance, Capacitance, Resistance) meter was used with the Micromanipulator probe station to test capacitance of the cantilever array. A test fixture (HP 16048 D) with a 1 m-long cable was used to connect directly to the micro probes. Separate micro probes were used to control actuation of the cantilever beams using a Krohn-hite 7602M power amplifier. Open/short corrections were then performed according to the 4284A user manual [63]. It should be noted that the optic power selected on the probe station affects the open correction measurement, therefore, the optic power *used* for observing deflection must be in position during the open mea-

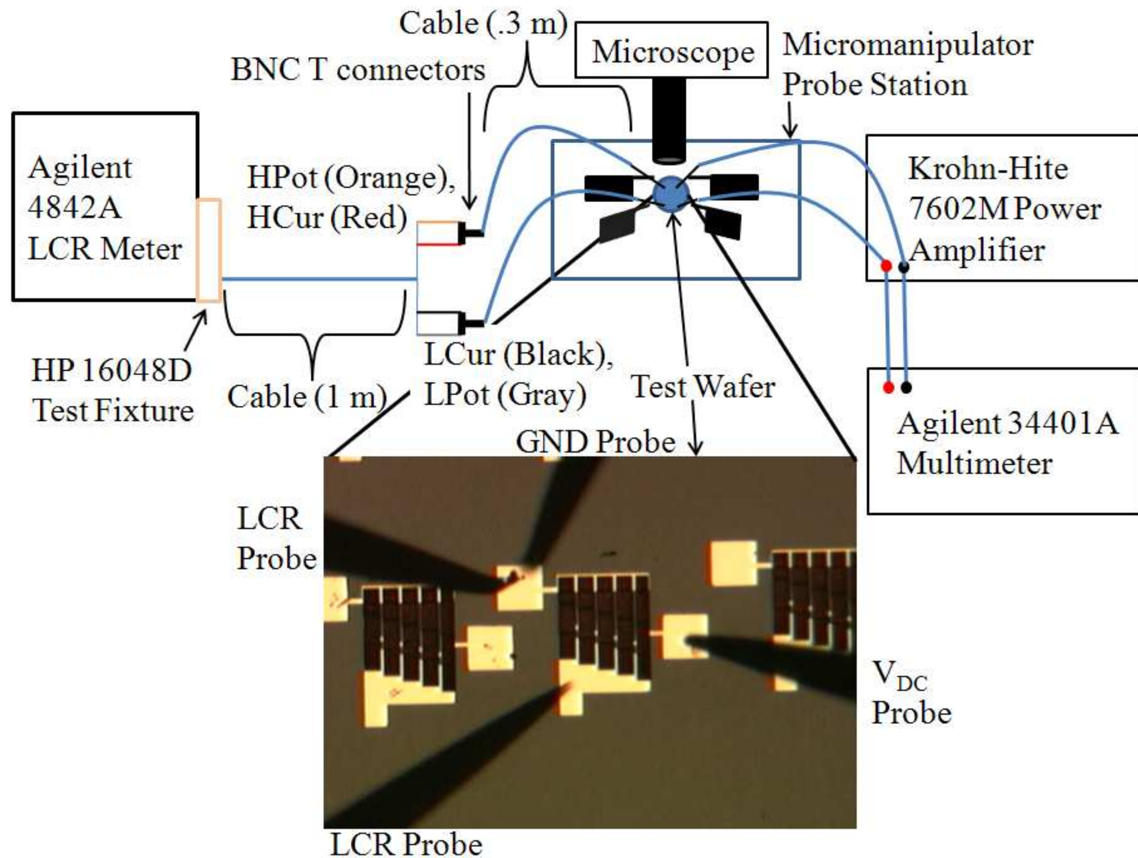

Figure 6.10: Schematic illustration of the experimental test setup used to actuate cantilevers and then measure resulting capacitance. During capacitance measurements, it was found that the amplifier ground was contaminating measurement data since the LCR meter provides its own virtual ground [62], therefore, the ground probe from the amplifier was not used for capacitance measurements.

surement correction (optic powers, 5×, 20×, 50×, etc., are different distances from the wafer which causes different parasitic capacitances). A thin-film chip capacitor with a known capacitance of 3.3 pF (+/ − 0.05 pF) was then tested with the LCR meter to ensure accuracy. The optics were focused on the SRR landing pad which makes the cantilever beams out of focus as shown in Figure 6.11(a). When the cantilever beams pull-in, they come into focus (Figure 6.11(b)) (this method allows the user to observe deflection without using an interferometer). Voltage on the electrodes was increased until the first cantilever came into focus. At that point, voltage and capacitance values were recorded, then voltage was increased again until the next beam pulled-in. After all beams pulled-in, voltage was reduced to release the beams. When the first

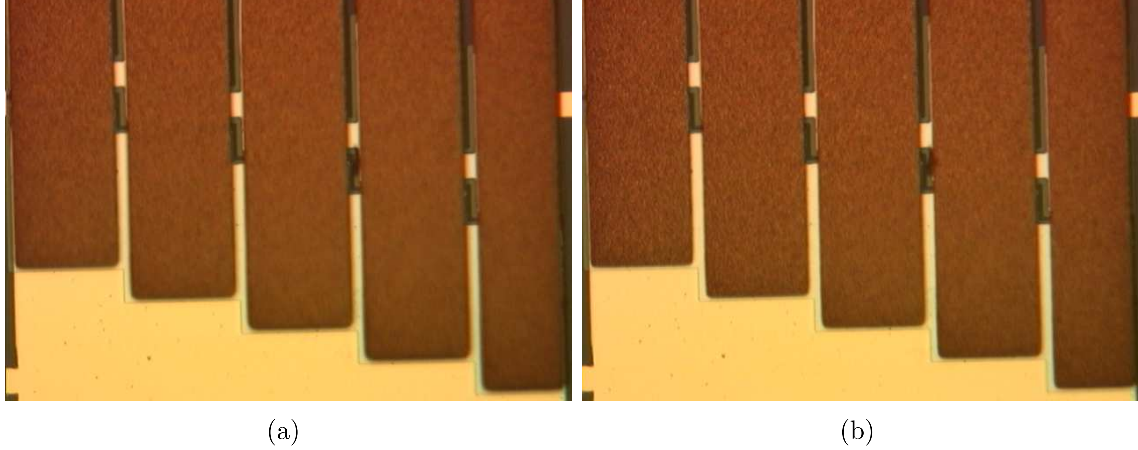

(a) (b)

Figure 6.11: Optics are focused on SRR landing pad, which leaves cantilevers out of focus (a), when beams pull-in, they come into focus (b).

beam released, amplifier voltage and capacitance were measured immediately before and after beam release. Voltage was then reduced until the next beam released and measurements were repeated. Voltage and capacitance measurements were taken periodically to show the capacitance measured between beams pulling-in and releasing. The following section presents the capacitance test results.

6.3.2 Capacitance Results. Figure 6.12 shows the C–V curve for the cantilever array during the pull-in cycle. From the data recorded in Figure 6.12, each cantilever provides an average increase of 0.085 pF when it pulls-in. This capacitance is 32 times less than the expected value of 2.789 pF. Measurements also show that capacitance decreases between beams pulling-in, which is opposite of the predicted behavior. Both results are caused because the beams collapse onto the electrode at pull-in. As shown in Figure 6.13, a collapsed beam has little surface area touching the landing pad, thus the low capacitance added per beam pulling-down. Additionally, when voltage increases beyond the collapse voltage, the collapsed surface area increases, which deflects the tip of the beam away from the landing pad as shown in Figure 6.13.

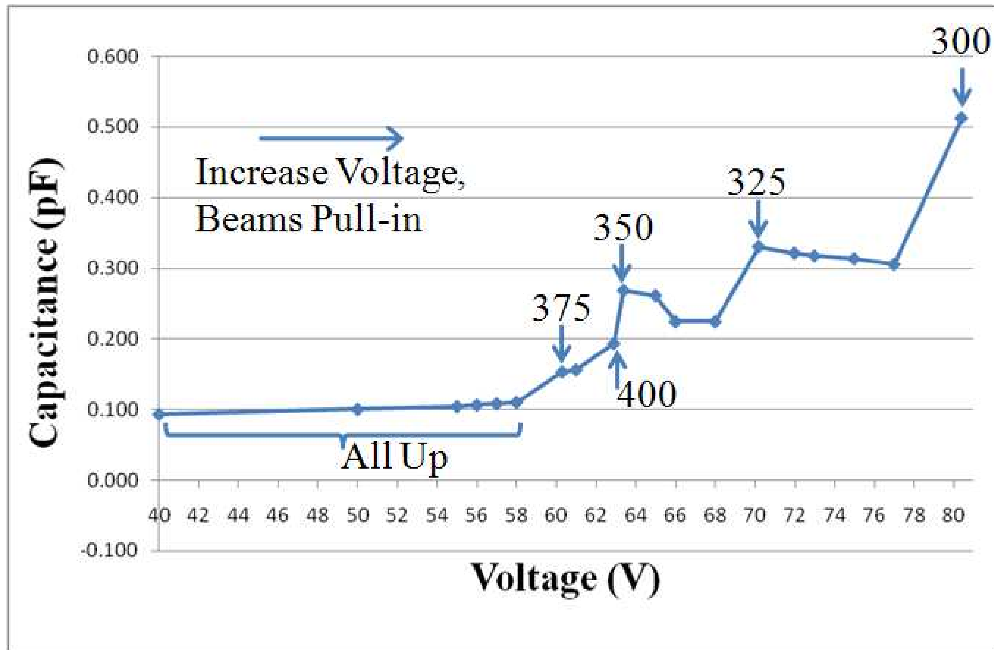

Figure 6.12: CV experimental test measurement for cantilever array. As voltage is increased, the cantilever beams pull-in, and capacitance slightly increases. The data points labelled with a beam length are where that respective beam pulled-in.

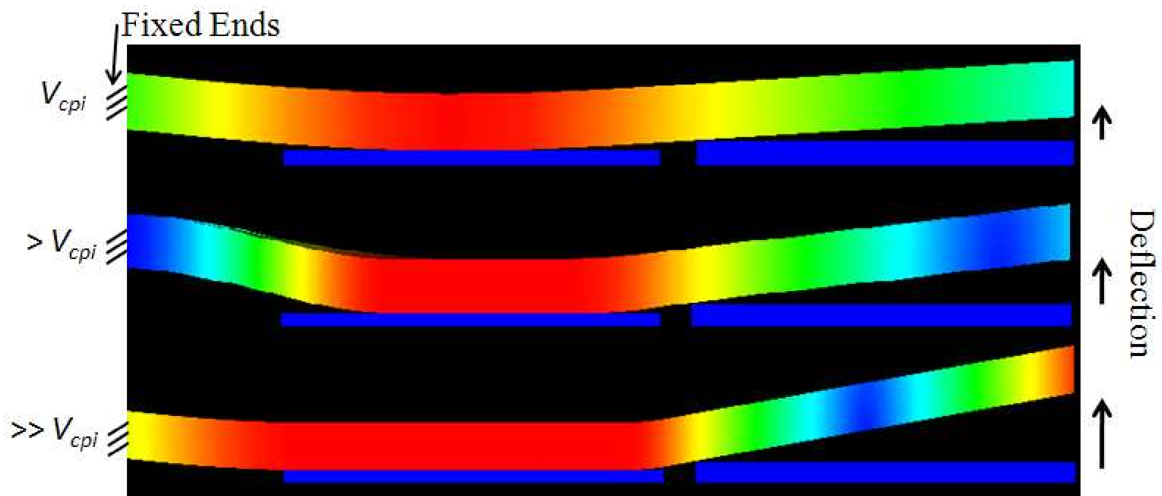

Figure 6.13: CoventorWare® simulation showing different stages of a collapsed beam. When voltage is applied beyond collapse voltage, the collapsed surface area on the electrode increases, which deflects the tip of the beam upwards. Capacitance decreases as the beam deflects away from the landing pad.

After the last beam pulled-in, the applied voltage was reduced. Figure 6.14 shows the C–V curve for the cantilever array during the release cycle. It is observed

in Figure 6.14 that the capacitance increases as voltage is reduced even with all beams pulled-in. This behavior agrees with the Zygo actuation voltage tests where the beams were collapsing immediately onto the electrode, but as voltage is reduced, the beams slightly pull off of the electrode, yet still remain down on the landing pad. When the beam pulls up from the collapsed-state, it increases the surface area touching the SRR landing pad (or decreases the distance to the landing pad), which increases capacitance (view Figure 6.13 from bottom-to-top; as voltage is reduced, the beam lifts up from the electrode).

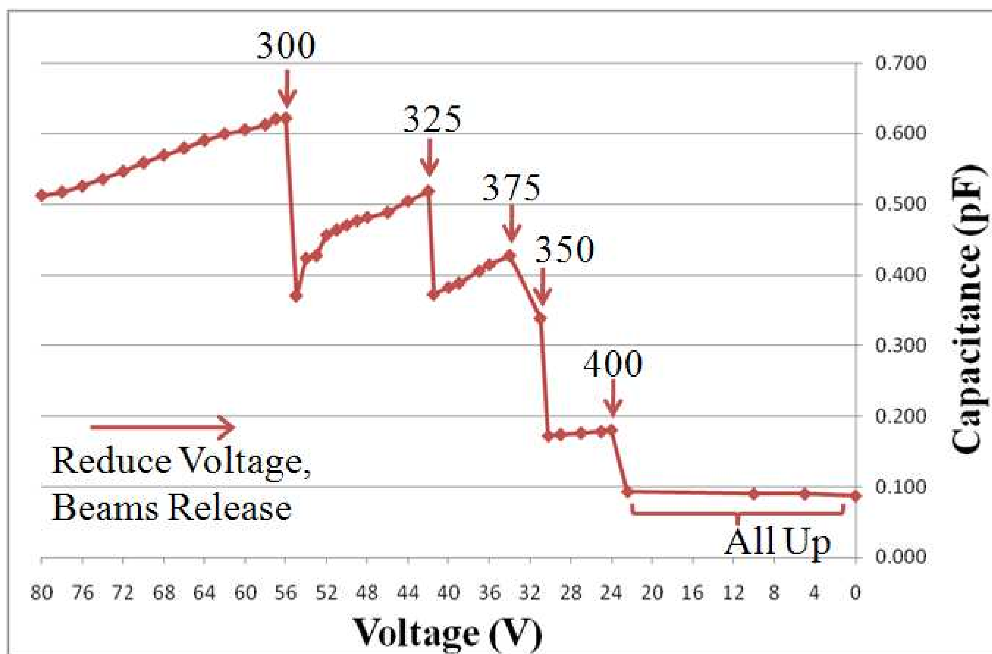

Figure 6.14: CV experimental test measurement for cantilever array. After the last beam pulls-in, voltage is reduced and then beams release. The data points labelled with a beam length are where that respective beam released.

6.3.3 Capacitance Measuring Issues. Since the microprobe connecting the power amplifier's ground to the device contaminated the capacitive results, one can hypothesize that the presence of the amplifier in the circuit affects the LCR meter. Removing the probe that supplies bias voltage did have an observed effect on the LCR meter. With the probe placed down on the electrode supply pad, the up-state capacitance read 0.087 pF. However, when the probe was removed, the LCR meter

displayed 0.12 pF which is closer to the predicted up-state value of 0.206 pF. Since the power amplifier is clearly changing the LCR readout, a test was conducted to measure the capacitance of a beam using a probe to physically press the beam down onto the landing pad as shown in Figure 6.15. Measurements from this test are shown in Table 6.5.

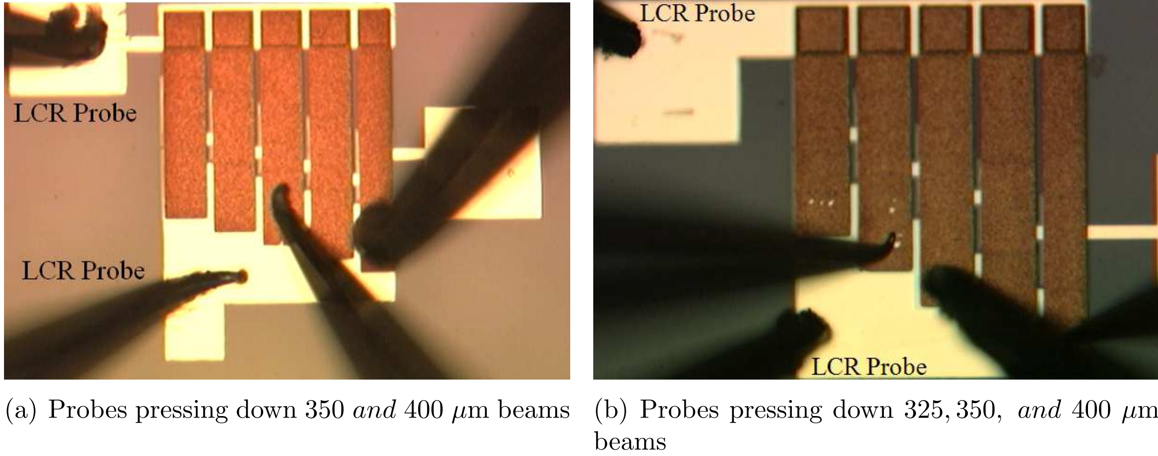

(a) Probes pressing down 350 *and* 400 μm beams (b) Probes pressing down 325, 350, *and* 400 μm beams

Figure 6.15: Measuring capacitance by pressing down beams with probe tips.

Table 6.5: Measured capacitance using probe tips to depress beams onto landing pads. The measured capacitance is read directly from the LCR meter. The capacitance added from a beam pulling-in is calculated by subtracting the previously measured value from the current value (i.e., 0.77 pF − 0.12 pF = 0.65 pF added by the 300 μm beam).

Length of Beam(s) Pressed Down (μm)	Measured Capacitance (pF)	Capacitance Added from Beam Pull-in (pF)
All Beams Up	0.12	
300	0.77	0.65
300 & 350	1.31	0.54
300, 350, & 375	1.93	0.62
300, 350, & 400	1.85	0.54

The capacitance measured using probe tips to press the beams down is much closer to the predicted value from Chapter 4. The deviation from calculated capacitance is most likely caused by dielectric and beam surface roughness. Recall that Lakshminarayanan et al. [26] reported a reduction of capacitance by 46 percent due

to dielectric surface roughness; the surface roughness underneath the beam (sputtered seed layer) also adds to this percentage reduction.

Another test was conducted where a probe tip was used to press down on the beam section above the electrode, as shown in Figure 6.16, to reproduce the capacitance results of a collapsed beam. The results are shown in Table 6.6.

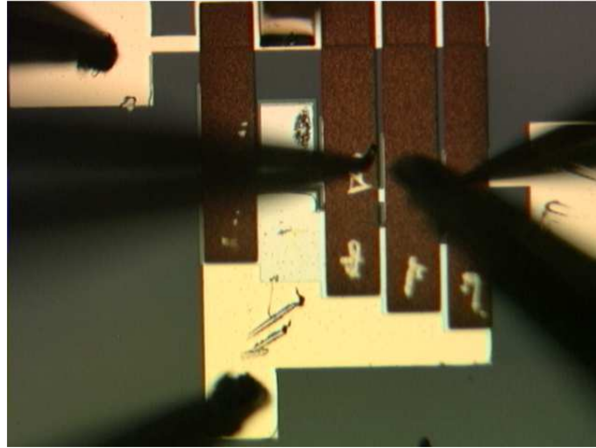

Figure 6.16: Probes pressing down beam sections directly over electrodes.

Table 6.6: Capacitance measured when probe tips are used to depress beams onto electrodes.

Beam Length (μm)	Capacitance per Beam (pF)
400	0.086
375	0.096
350	0.078
325	0.09
300	0.085

The test results are nearly identical to the capacitance measured when a voltage was used to actuate the beams (average was 0.085 pF). This test strengthens the assumption that the beams collapse onto the electrodes at pull-in.

6.4 Cantilever Lifetime Test

A limited lifetime test was conducted on a cantilever array. A signal generator was used with a voltage source to create a pulse that actuates the beam multiple times-

per-second. Visual confirmation of device actuation was confirmed by the microscope on the microprobe station. Frequency (25 Hz), DC voltage (80 V), and pulse width (19 ms) were adjusted to actuate all beams at once. At the termination of the test (18 hours), all five beams were still actuating. The beams actuated a total of 1.62×10^6 cycles.

6.5 SRR Testing

SRR unit cells were diced for individual testing as shown in Figure 6.17. The cantilever beams on the SRRs were bent up more than the test cantilever structures and did not pull-down less than 100 V. The difference in beam curvature across the wafer is due to different Au electroplated thicknesses. Au electroplates slower in the center of the wafer, which is where the SRR cells are located.

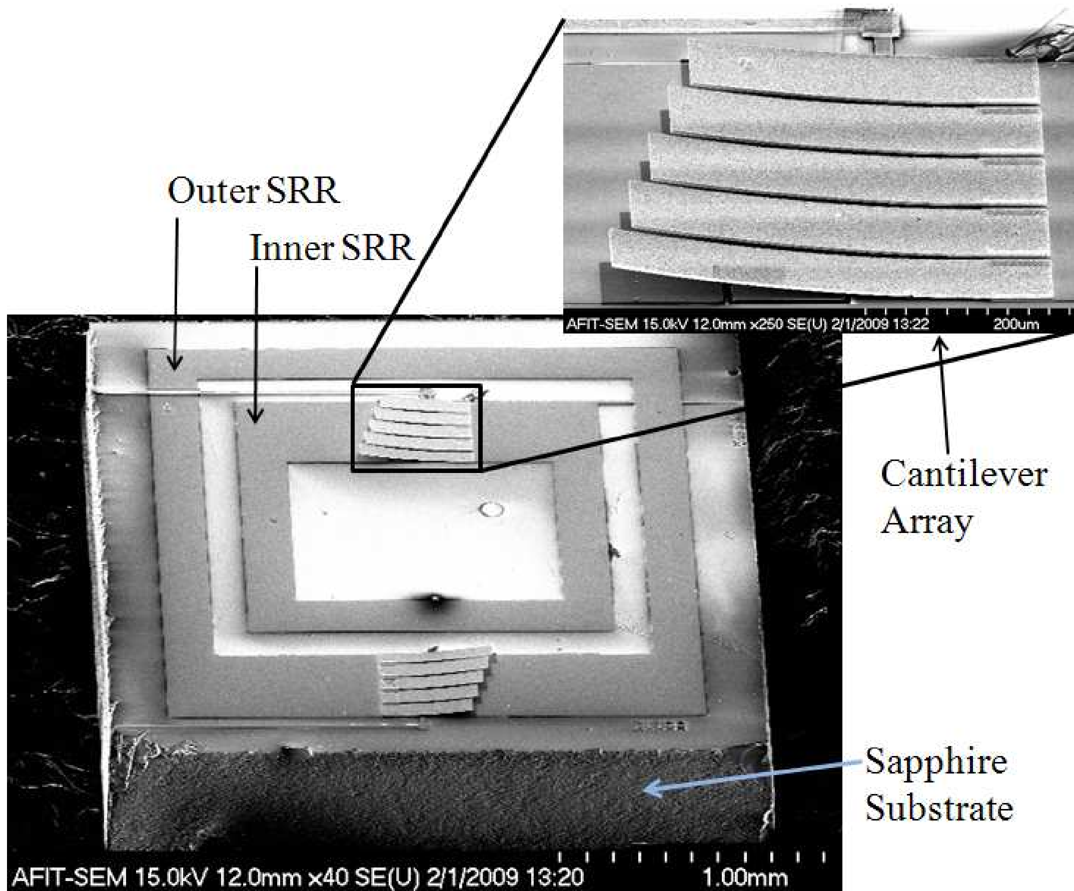

Figure 6.17: SEM image of SRR unit cell.

6.6 S-parameter Measurements

S-parameters are used to infer the effective medium properties from a unit cell SRR structure. Reflection and transmission measurements are made using a parallel-plate rectangular waveguide as shown in Figure 6.18. The waveguide efficiently shields the sample from the external environment [55].

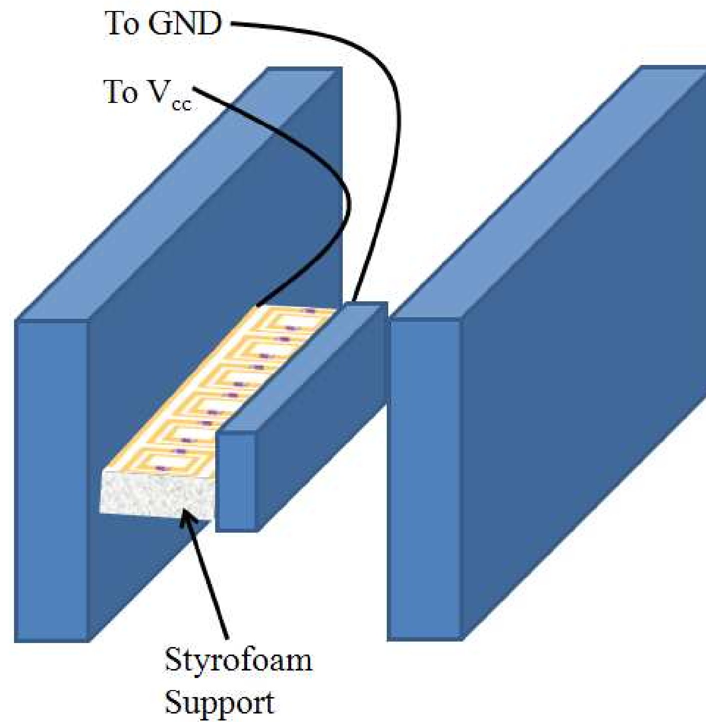

Figure 6.18: Waveguide test setup to measure S-parameters of SRR devices.

6.7 Chapter Summary

This chapter presented the results from testing conducted on the cantilever array test devices. Tests were conducted on all test wafers, however, only SaW3 and SaW4 produced testable devices. During pull-in tests, devices would stick or breakdown, however, after being plasma ashed, failures were minimal. Pull-in voltages were higher than predicted because beam curl from tensile stress had increased the gap between the beams and electrodes. Capacitance values were lower than expected because the beams were collapsing onto the electrodes instead of pulling down onto the SRR

landing pad. Lifetime testing showed that beams are capable of actuating over one million cycles. Conclusions of testing and recommendations for further research are presented in the next chapter.

VII. Conclusions and Recommendations

7.1 Overall Summary

In this thesis, the design, fabrication, and testing of a MEMS capacitive array were presented. Analytical equations were developed to predict pull-in voltages, however, a comparison with test results could not be made because of tensile stress in the cantilever beams. Overall, the results show that the cantilever beams pull-in one-at-a-time as predicted and each pulled-in beam adds capacitance to the SRR. However, the voltage needed to actuate the beams is double the predicted pull-in voltage, which causes the beams to collapse onto the electrode instead of the SRR landing pad. A brief summary of specific conclusions is presented next.

7.1.1 SRR with MEMS Devices.

Most notably, this study presents the first known in-situ fabrication of an SRR and MEMS device. This design offers a smaller device footprint, compatible fabrication steps, and a variable voltage controlled capacitance.

7.1.2 Device Fabrication.

Coutu's fabrication process [20] was a valuable starting point for this research. Modifications were made due to different equipment and chemicals available. The final fabrication process followers are in Appendix 1.

7.1.2.1 SF-11 Planar Coating.

A planar sacrificial layer was not achieved during fabrication (due to insufficient re-flow time), which caused the cantilever beams to be conformal to the previous layers–an undesired result.

7.1.2.2 Plasma Ashing.

It is necessary to plasma ash the MEMS devices after release to reduce stiction and breakdown failures. Stiction was nearly non-existent in most cases after the device had been plasma ashed.

7.1.2.3 Tensile Stress in Electroplated Beams.

The most significant problem for this research was attempting to develop an electroplating process that deposits low tensile stress Au (not accomplished). The fabrication timeline for this

study did not allow time to conduct an intensive analysis of variance on the electroplater machine settings. The tensile stress causes the cantilever beams to curl up, which affects pull-down voltage and indirectly results in low capacitance added at pull-in.

7.1.3 Experiments and Results.

7.1.3.1 Capacitance Measurements. It is possible that the power amplifier is affecting the LCR measuring device. For future research, a S-parameter measurement is needed to determine if this is the case.

7.1.3.2 Device Consistency. Currently, the gap underneath the beam is not a user controlled dimension because of tensile stress, which causes beam deflection. Also, tensile stress varies across sample wafers, therefore, identical cantilevers on different areas of the same chip did not consistently actuate at the same voltages. Without a controllable gap, the SRR ring arrays do not resonate at the same frequency. Additionally, the electroplated Au thickness across the wafer is not consistent, which affects pull-in voltages (current density is higher on the wafer edge, which causes a faster deposition).

7.2 Recommendations for Future Research

The results of this thesis demonstrate the feasibility of using a MEMS cantilever array to control the resonating frequency of an SRR. This study also serves to provide a foundation for future research in MEMS on metamaterial. As such, the following recommendations learned through fabrication and testing are provided.

7.2.1 Design Recommendations. The following is a list of recommendations and explanation for design changes.

1. Increase dielectric coverage on SRR landing pad. This prevents devices from shorting if masking during lithography is misaligned.

2. Experiment with beam widths (i.e., 90 *or* 100 μm instead of 75 μm). If tensile stress is still an issue, a wider beam does not curl as much because it has a higher spring constant.
3. Make all cantilever beam widths the same. The different spring constant for the 400 μm long beam makes it curl more than the others. Or, if electroplating is perfected and beams do not curl from residual stress, then Luo et al.'s [40] beam width equation to create a linear C–V relationship can be used:

$$W_i = W_1(1 + 0.3i) \tag{7.1}$$

   where W_1 is the width of the first cantilever beam, W_2 is the width of the next longer beam, etc.
4. Create single SRR structures with no center ring. Bringing a voltage bias to the inner ring adds complexity and a greater chance of failure to the design. Also, the Au line connecting the inner ring to the outer ring might change the resonant behavior of the SRR unit cell. It has been shown that a center ring is not needed to produce a SRR [5, 46].
5. Create a via hole to supply V_{cc} power directly to inner ring electrodes instead of passing over split ring.
6. Create unit cells or small groups of SRRs instead of one large array. One short in the array causes total device failure.
7. Create more test SRR structures with probe pads close to each other for easy testing.
8. Create bigger alignment marks in mask design with large windows nearby. This decreases the amount of time spent aligning dark masks.
9. Change alignment mark design to the AFRL/SN standard alignment mark system for more accurate results.

10. Create circular SRR structures to test. Most research has focused on circular SRRs, therefore, more equations are available to predict device behavior.
11. Change current SRR structure to have a uniform width.
12. Test a cantilever structure with the electrode at the same height as the SRR (instead of being slightly lower). The beam collapses at a lower voltage, however, it should not deflect upwards.
13. Incorporate plating clip areas into cantilever mask. This provides the user with a known surface area open to be electroplated (needed to calculate current density).

7.2.2 Fabrication Recommendations. The following is a list of recommendations and explanation for fabrication changes.

1. Perform an analysis of variance on the electroplating machine settings which produce beams with the least amount of tensile stress.
2. Sputter a thinner seed layer of Au. The sputtered and electroplated Au layers could potentially have different coefficients of thermal expansion, which causes a tensile stress.
3. Research using a different material for the cantilever beam such as nickel (Ni). Luo et al. [40] fabricated Ni cantilever beams with low stress.
4. Research alternative depositing methods besides electroplating (i.e., LIGA or micromolding). Most research is conducted on metallic SRR structures that are greater than 15 μm thick.
5. Purchase thicker lift off resist (LOR) to evaporate thicker structures.
6. Research creating a planar layer of SF-11. More time/heat might be needed to correctly re-flow the PMGI. A seed layer sputtered on a flat layer of SF-11 ensures electroplating deposition is more uniform.

7. Use LPCVD to deposit the dielectric layer to get better breakdown and less pinholes. Low pressure chemical vapor deposition (LPCVD) has no pinholes, conformal step coverage, and has a dielectric strength of 10 MV/cm [56]. Another option–Chang et al [13] report on using high density inductively coupled plasma (HDICP) chemical vapor deposition (CVD) in place of using PECVD and observed that the HDICP CVD Si_3N_4 film had a lower surface roughness, a higher breakdown voltage (> 9 MV/cm), and less pin hole density than PECVD grown Si_3N_4. HDICP CVD is conducted at low temperatures ($90 - 170\,^{\circ}$C [13]) which is compatible with micromachine fabrication.

8. Deposit a thicker dielectric if using PECVD because of pinholes and low breakdown strength. Note that a thicker dielectric layer decreases the switch capacitance provided at pull-in.

9. Use other high-k dielectrics. For example, Park et al. [12] use strontium titanate oxide ($SrTiO_3$) for a dielectric layer which has a dielectric constant ranging from $30 - 120$ depending on what temperature it was deposited at—higher temperature results in a higher dielectric constant. $SrTiO_3$ also has low loss, low leakage current, and high breakdown voltage [12]. HfO_2 as used by Luo et al. [40] is another option for a high-k dielectric.

VIII. Appendix 1. Process Followers

Wafer	Purpose	Mask	Process	Print Date
SaW4	**MEMS**	***SRR***	**SRR Base Metal**	February 8, 2009

Init.	Process Step	Notes	Date Time
	INSPECT WAFER: ☐ Note any defects	**Start Date** **Start Time**	
	SOLVENT CLEAN WAFER: ☐ 30 sec acetone rinse at 500 rpm ☐ 30 sec methanol rinse at 500 rpm ☐ 30 sec isopropyl alcohol rinse at 500 rpm ☐ Dry with nitrogen at 500 rpm ☐ Dry wafer with nitrogen on clean texwipes		
	DEHYDRATION BAKE: ☐ 2 min 110°C hot plate bake		
	FIRST LOR COAT: ☐ Flood wafer with LOR 3A ☐ 4 sec spread at 500 rpm ☐ 30 sec spin at 2,000 rpm ☐ 2 min 170°C hot plate bake		
	SECOND LOR COAT: ☐ Flood wafer with LOR 3A ☐ 4 sec spread at 500 rpm ☐ 30 sec spin at 2,000 rpm ☐ 2 min 170°C hot plate bake		
	1818 COAT: ☐ Flood wafer with 1818 ☐ 4 sec spread at 500 rpm ☐ 30 sec spin at 3,000 rpm ☐ 2 min 110°C hot plate bake ☐ Use acetone to remove 1818 on backside		
	EXPOSE 1818 WITH SRR MASK: ☐ No alignment for first level mask needed, however mask should be straight ☐ 3.0 sec exposure using EVG 620		
	1818 DEVELOP AND LOR UNDERCUT: ☐ 70 sec develop with LDD-26W, flood wafer first, then use a spin/stop/spin/stop method at 500 rpm ☐ 30 sec DI water rinse at 500 rpm ☐ Dry with nitrogen at 500 rpm ☐ Dry wafer with nitrogen on clean texwipes		
	INSPECT RESIST: ☐ Inspect photoresist under microscope		
	ASHER DESCUM: ☐ 4 min, 150 W, LFE Barrel Asher		
	TENCOR MEASUREMENT: ☐ Measure photoresist step height T ______________ C ______________ B ______________		
	BOTTOM METAL DEPOSITION: ☐ Evaporate 200 Å Ti / 5500 Å Au with Figure 8 pattern at 4.8 kV, 30 mA		
	LIFT-OFF METAL: ☐ Heat 1165 remover to 90°C (set hot plate to 170°C) ☐ 30 min soak in acetone ☐ 5 min vibrobath in acetone ☐ 60 min soak in 1165 at 90°C ☐ 5 min vibrobath in acetone ☐ 10 min soak in 1165 at 90°C ☐ 20 sec DI rinse at 500 rpm ☐ 30 sec acetone rinse at 500 rpm ☐ 30 sec methanol rinse at 500 rpm ☐ 30 sec isopropyl alcohol rinse at 500 rpm ☐ Dry with nitrogen at 500 rpm ☐ Dry wafer with nitrogen on clean texwipes		

Process Step #1 **Revision 1.00** (29 Jan 09) Page 1

Wafer	Purpose	Mask	Process	Print Date
SaW4	**MEMS**	***SRR***	**SRR Base Metal**	February 8, 2009

	INSPECT METAL: ☐ Inspect metal under microscope		
	ASHER DESCUM: ☐ 4 min, 150 W, LFE Barrel Asher		
	TENCOR MEASUREMENT: ☐ Measure metal step height T ______________ C ______________ B ______________		

Wafer	Purpose	Mask	Process	Print Date
SaW4	**MEMS**	***Electrode***	**Electrode Base Metal**	February 8, 2009

Init.	Process Step	Notes	Date Time
	DEHYDRATION BAKE: ☐ 2 min 110°C hot plate bake	**Start Date** **Start Time**	
	FIRST LOR COAT: ☐ Flood wafer with LOR 3A ☐ 4 sec spread at 500 rpm ☐ 30 sec spin at 2,000 rpm ☐ 2 min 170°C hot plate bake		
	SECOND LOR COAT: ☐ Flood wafer with LOR 3A ☐ 4 sec spread at 500 rpm ☐ 30 sec spin at 2,000 rpm ☐ 2 min 170°C hot plate bake		
	1818 COAT: ☐ Flood wafer with 1818 ☐ 4 sec spread at 500 rpm ☐ 30 sec spin at 3,000 rpm ☐ 2 min 110°C hot plate bake ☐ Use acetone to remove 1818 on backside		
	EXPOSE 1818 WITH ELECTRODE MASK: ☐ Align to bottom metal alignment marks ☐ 3.0 sec exposure using EVG 620		
	1818 DEVELOP AND LOR UNDERCUT: ☐ 70 sec develop with LDD-26W, flood wafer first, then use a spin/stop/spin/stop method at 500 rpm ☐ 30 sec DI water rinse at 500 rpm ☐ Dry with nitrogen at 500 rpm ☐ Dry wafer with nitrogen on clean texwipes		
	INSPECT RESIST: ☐ Inspect photoresist under microscope		
	ASHER DESCUM: ☐ 4 min, 150 W, LFE Barrel Asher		
	TENCOR MEASUREMENT: ☐ Measure photoresist step height T _______________ C _______________ B _______________		
	BOTTOM METAL DEPOSITION: ☐ Evaporate 200 Å Ti / 4500 Å Au with Figure 8 pattern at 4.8 kV, 30 mA		
	LIFT-OFF METAL: ☐ Heat 1165 remover to 90°C (set hot plate to 170°C) ☐ 30 min soak in acetone ☐ 5 min vibrobath in acetone ☐ 60 min soak in 1165 at 90°C ☐ 5 min vibrobath in acetone ☐ 10 min soak in 1165 at 90°C ☐ 20 sec DI rinse at 500 rpm ☐ 30 sec acetone rinse at 500 rpm ☐ 30 sec methanol rinse at 500 rpm ☐ 30 sec isopropyl alcohol rinse at 500 rpm ☐ Dry with nitrogen at 500 rpm ☐ Dry wafer with nitrogen on clean texwipes		
	INSPECT METAL: ☐ Inspect metal under microscope		
	ASHER DESCUM: ☐ 4 min, 150 W, LFE Barrel Asher		
	TENCOR MEASUREMENT: ☐ Measure metal step height T _______________ C _______________ B _______________		

Process Step #1 **Revision 1.00** (29 Jan 09) Page 1

Wafer	Purpose	Mask	Process	Print Date
SaW4	**MEMS**	***Dielectric***	**Dielectric Deposition**	February 8, 2009

Init.	Process Step	Notes	Date Time
	DIELECTRIC DEPOSITION: ☐ Deposit 2000 Å Si_3N_4 ☐ PECVD BLAH min, 17 sccm 5% Silane in N_2, 25 sccm N_2, 10 sccm NH_4, 20W, 850 mTorr, 250 °C	**Start Date** **Start Time**	
	INSPECT DIELECTRIC: ☐ Inspect dielectric under microscope and look for ○ Uniform color ○ Pin holes ○ Cracks around metal ○ Flaking		
	1818 COAT: ☐ Flood wafer with 1818 ☐ 4 sec spread at 500 rpm ☐ 30 sec spin at 3,000 rpm ☐ 2 min 110°C hot plate bake ☐ Use acetone to remove 1818 on backside		
	EXPOSE 1818 WITH DIELECTRIC MASK: ☐ Align to bottom metal alignment marks ☐ 3.0 sec exposure using EVG 620		
	1818 DEVELOP: ☐ 70 sec develop with 351:DI (1:5), flood wafer first, then use a spin/stop/spin/stop method at 500 rpm ☐ 30 sec DI water rinse at 500 rpm ☐ Dry with nitrogen at 500 rpm ☐ Dry wafer with nitrogen on clean texwipes		
	INSPECT RESIST: • Inspect photoresist under microscope		
	ASHER DESCUM: ☐ 4 min, 150 W, LFE Barrel Asher		
	TENCOR MEASUREMENT: ☐ Measure photoresist step height T ______________ C ______________ B ______________		
	RIE DIELECTRIC: ☐ 3:15 min Plasma Therm 790 RIE Etch, 40-sccm CF_4, 3-sccm 10% O_2, at 50 mTorr, 100 W		
	INSPECT DIELECTRIC: ☐ Inspect dielectric removal under microscope		
	REMOVE 1818: ☐ 30 sec acetone rinse at 500 rpm ☐ 30 sec methanol rinse at 500 rpm ☐ 30 sec isopropyl alcohol rinse at 500 rpm ☐ Dry with nitrogen at 500 rpm ☐ Dry wafer with nitrogen on clean texwipes		
	INSPECT RESIST: • Inspect under microscope for resist removal		
	ASHER DESCUM: ☐ 4 min, 150 W, LFE Barrel Asher		
	TENCOR MEASUREMENT: ☐ Measure metal step height T ______________ C ______________ B ______________		

Wafer	Purpose	Mask	Process	Print Date
SaW4	**MEMS**	***Post***	**Sacrificial layer and Post**	February 8, 2009

Init.	Process Step	Notes	Date Time
	DEHYDRATION BAKE: ☐ 2 min 110°C hot plate bake	**Start Date** **Start Time**	
	FIRST SF-11 (PMGI) COAT: ☐ Flood wafer with SF-11 ☐ 4 sec spread at 500 rpm ☐ 30 sec spin at 4,000 rpm ☐ 2 min 270°C hot plate bake		
	SECOND SF-11 (PMGI) COAT: ☐ Flood wafer with SF-11 ☐ 4 sec spread at 500 rpm ☐ 30 sec spin at 4,000 rpm ☐ 2 min 270°C hot plate bake		
	1813 COAT: ☐ Flood wafer with 1813 ☐ 4 sec spread at 500 rpm ☐ 30 sec spin at 4,000 rpm ☐ 75 sec 110°C hot plate bake ☐ Use acetone to remove 1818 on backside		
	EXPOSE 1813 WITH POST MASK: ☐ Align to bottom metal alignment marks ☐ 3.5 sec exposure using EVG 620		
	1813 DEVELOP: ☐ 40 sec develop with 351 (1:5), flood wafer first using *two* bottles, then use a spin/stop/spin/stop method at 500 rpm ☐ 30 sec DI water rinse at 500 rpm ☐ Dry with nitrogen at 500 rpm ☐ Dry wafer with nitrogen on clean texwipes		
	INSPECT RESIST: ☐ Inspect photoresist under microscope		
	ASHER DESCUM: ☐ 4 min, 150 W, LFE Barrel Asher		
	TENCOR MEASUREMENT: ☐ Measure photoresist step height T ______________ C ______________ B ______________		
	FIRST DUV CYCLE (~1.5 µm / cycle): ☐ 200 sec DUV exposure @ 35 mW/cm², 254 nm		
	SF-11 DEVELOP: ☐ 60 sec bucket develop with SAL 101 ☐ 4x DI bucket rinse ☐ Dry wafer with nitrogen on clean texwipes		
	INSPECT RESIST: ☐ Inspect SF-11 under microscope, check for fringe patterns indicating residual SF-11		
	SECOND DUV CYCLE (~1.5 µm / cycle): ☐ 200 sec DUV exposure @ 35 mW/cm², 254 nm		
	SF-11 DEVELOP: ☐ 60 sec bucket develop with SAL 101 ☐ 4x DI bucket rinse ☐ Dry wafer with nitrogen on clean texwipes		
	INSPECT RESIST: ☐ Inspect SF-11 under microscope, check for fringe patterns indicating residual SF-11		
	TENCOR MEASUREMENT: ☐ Measure resist step height T ______________ C ______________ B ______________		

Wafer	Purpose	Mask	Process	Print Date
SaW4	**MEMS**	***Post***	**Sacrificial layer and Post**	February 8, 2009

	REMOVE 1813: ☐ 30 sec acetone rinse at 500 rpm *Do not allow acetone to dry on SF-11 ☐ 30 sec methanol rinse at 500 rpm ☐ 30 sec isopropyl alcohol rinse at 500 rpm ☐ 10 sec DI rinse at 500 rpm ☐ Dry with nitrogen at 500 rpm ☐ Dry wafer with nitrogen on clean texwipes		
	INSPECT RESIST: ☐ Inspect photoresist for 1813 removal		
	ASHER DESCUM: ☐ 4 min, 150 W, LFE Barrel Asher		
	TENCOR MEASUREMENT: ☐ Measure SF-11 step height T ______________ C ______________ B ______________		
	POST REFLOW & INSPECT WAFER: ☐ 90 sec 250°C hot air oven bake **OR** ☐ 45 sec 270°C hot plate bake ☐ Inspect for resist reflow. ☐ Reflow again if necessary *NOTE: This step has not worked to reflow resist, more research is needed		
	TENCOR MEASUREMENT: ☐ Measure SF-11 step height T ______________ C ______________ B ______________		
	HARD BAKE: ☐ Place in 90°C hot air oven 60 min before seed layer deposition ☐ Skip if reflow just completed and seed layer deposition immediately follows		

Wafer	Purpose	Mask	Process	Print Date
SaW4	**MEMS**	***Cantilever***	**Electroplate Beam and Release**	February 8, 2009

Init.	Process Step	Notes	Date Time
	SPUTTER SEED LAYER: ☐ Sputter 1000 Å Au using Discovery-18	**Start Date** **Start Time**	
	AZ 4620 COAT: ☐ Flood wafer with AZ 4620 ☐ 4 sec spread at 300 rpm ☐ 60 sec spin at 1,900 rpm ☐ 85 sec 110°C hot plate bake		
	EXPOSE AZ 4620 WITH CANTILEVER MASK: ☐ Align to bottom metal alignment marks ☐ 100 mJ/cm^2 constant dose exposure using EVG 620		
	AZ 4620 DEVELOP: ☐ 3 min develop with AZ400K:DI (1:4) o Bucket develop using a beaker, agitate, but do not make liquid swirl, create waves parallel with beam ☐ 30 sec DI water rinse using one quick spin at 500 rpm (2 sec) then stop ☐ Dry with nitrogen at 500 rpm ☐ Dry wafer with nitrogen on clean texwipes		
	INSPECT RESIST: ☐ Inspect photoresist under microscope		
	CLEAR PLATING CLIP AREAS: ☐ Use cotton swab with acetone using foil-mask clip template		
	WAFER EDGE PROTECT: ☐ Coat wafer edge with 1400-27 resist using swab ☐ Air dry with nitrogen		
	ASHER DESCUM: ☐ 4 min, 150 W, LFE Barrel Asher		
	TENCOR MEASUREMENT: ☐ Measure photoresist step height T ______________ C ______________ B ______________		
	ELECTROPLATE CANTILEVER BEAMS: ☐ Plating conditions* : o Bath temp 58.5°C o Duty cycle 40-on/60-off o Current density at 2.0 mA/cm^2 o Average current 12 mA ☐ Electroplate for 0.5 A-min		
	TENCOR MEASUREMENT: ☐ Measure electroplated step height Posts: T ______________ C ______________ B ______________ Beam End: T ______________ C ______________ B ______________ ☐ Repeat electroplating step if needed		
	REMOVE AZ 4620: ☐ 30 sec acetone rinse at 500 rpm ☐ 30 sec methanol rinse at 500 rpm ☐ 30 sec isopropyl alcohol rinse at 500 rpm ☐ 30 sec DI rinse at 500 rpm ☐ Dry with nitrogen at 500 rpm ☐ Dry wafer with nitrogen on clean texwipes		
	ASHER DESCUM: ☐ 4 min, 150 W, LFE Barrel Asher		

Process Step #1 **Revision 1.00** (29 Jan 09) Page 1

Wafer	Purpose	Mask	Process	Print Date
SaW4	**MEMS**	***Cantilever***	**Electroplate Beam and Release**	February 8, 2009

	SEED LAYER ETCH: ☐ 1 min KI etch ☐ 4x DI bucket rinse ☐ Dry with nitrogen on clean texwipes		
	INSPECT RESIST: ☐ Make sure seed layer is completely removed		
	AZ 4620 RE-COAT FOR DICING: ☐ Flood wafer with AZ 4620 ☐ 4 sec spread at 300 rpm ☐ 60 sec spin at 1,900 rpm ☐ 85 sec 110°C hot plate bake		
	WAFER DICING: ☐ Dice wafer at AFRL/SN ☐ Create a cutting map in L-edit for dicing technician ☐ Sections must fit in 1-inch CO_2 Dryer		
	REMOVE AZ 4620: ☐ 30 sec acetone rinse at 500 rpm ☐ 30 sec methanol rinse at 500 rpm ☐ 30 sec isopropyl alcohol rinse at 500 rpm ☐ 30 sec DI rinse at 500 rpm ☐ Dry with nitrogen at 500 rpm ☐ Dry wafer with nitrogen on clean texwipes		
	ASHER DESCUM: ☐ 10 min, 150 W, LFE Barrel Asher		
	STRIP SF-11 SACRIFICIAL LAYER (RELEASE PROCESS): ☐ Do NOT vibrobath devices ☐ Heat 1165 remover to 90°C (set hot plate to 170°C) ☐ 45 min soak in 1165 at 90°C ☐ Wet transfer from 1165 beaker to 1st IPA in petri dish, 30 sec soak ☐ Wet transfer to 2nd IPA in petri dish, 30 sec soak ☐ Wet transfer to 3rd IPA in petri dish, 30 sec soak ☐ Wet transfer to 4th IPA in petri dish, 30 sec soak ☐ Wet transfer to 1st methanol in petri dish, 30 sec soak ☐ Wet transfer to 2nd methanol in petri dish, 30 sec soak ☐ Wet transfer to 3rd methanol in petri dish, 30 sec soak ☐ Wet transfer to 4th methanol in petri dish, 30 sec soak ☐ Fill CO^2 dryer chamber with enough methanol to cover the wafer. ☐ Remove wafer from 4th methanol dish and place in CO^2 dryer chamber. ☐ Immediately cover CO^2 dryer and start process		
	ASHER DESCUM: ☐ 30 min, 150 W, LFE Barrel Asher		

Bibliography

1. J. B. Pendry, A. J. Holden, D. J. Robbins, and W. J. Stewart, “Magnetism from conductors and enhanced nonlinear phenomena,” *IEEE Transactions on Microwave Theory and Techniques*, vol. 47, pp. 2075–2084, November 1999.
2. K. Aydin and E. Ozbay, “Capacitor-loaded split ring resonators as tunable metamaterial components,” *Journal of Applied Physics*, vol. 101, pp. 024911 1–5, 2007.
3. R. Marqués, “Some recent topics in bulk split-ring metamaterials,” in *Metamaterials*, (Pamplona, Spain), September 2008.
4. I. Gil, J. Garcia-Garcia, J. Bonache, F. Martin, M. Sorolla, and R. Marqués, “Varactor-loaded split ring resonators for tunable notch filters at microwave frequencies,” *Electronics Letters*, vol. 40, pp. 1347–1348, October 2004.
5. T. Hand and S. Cummer, “Characterization of tunable metamaterial elements using mems switches,” *IEEE Antennas and Wireless Propagation Letters*, vol. 6, pp. 401–404, 2007.
6. D. R. Smith, D. C. Vier, T. Koschny, and C. M. Soukoulis, “Electromagnetic parameter retrieval from inhomogeneous metamaterials,” *Physical Review E*, vol. 71, pp. 1–11, March 2005.
7. G. M. Rebeiz, *RF MEMS Theory, Design, and Technology.* New Jersey: John Wiley & Sons, Inc., 2003.
8. C. Buccella, M. Feliziani, and G. Manzi, “Circuit modeling of rf capacitive mems switch,” *Industrial Electronics, 2005. ISIE 2005. Proceedings of the IEEE International Symposium on*, vol. 3, pp. 1117–1121, June 2005.
9. C. Goldsmith, Z. Yao, S. Eshelman, and D. Denniston, “Performance of low-loss rf mems capacitive switches,” *IEEE Microwave and Guided Wave Letters*, vol. 8, pp. 269–271, August 1998.
10. P. D. Grant, M. W. Denhoff, and R. R. Mansour, “A comparison between rf mems switches and semiconductor switches,” in *International Conference on MEMS, Nano and Smart Systems*, pp. 515–521, National Research Council of Canada, August 2004.
11. D. Saias, P. Robert, S. Boret, C. Billard, G. Bouche, D. Belot, and P. Ancey, “An above ic mems rf switch,” *IEEE Journal of Solid-State Circuits*, vol. 38, pp. 2318–2324, December 2003.
12. J. Park, G. Kim, K. Chung, and J. Bu, “Monolithically integrated micromachined rf mems capacitive switches,” *Sensors and Actuators A: Physical*, vol. 89, pp. 88–94, 2001.

13. C. H. Chang, J. Y. Qian, B. A. Cetiner, Q. Xu, M. Bachman, H. K. Kim, Y. Ra, F. De Flaviis, and G. P. Li, “Rf mems capacitive switches fabricated with hdicp cvd sinx,” *Microwave Symposium Digest, 2002 IEEE MTT-S International*, vol. 1, pp. 231–234, 2002.

14. C. Wheeler, “The superior rf switch technology - part 1 - the advantages of mems,” *MagLatch*, www.microlab.net.

15. L. Liu, “High performance rf mems series contact switch design and simulations,” *Electronic Components and Technology Conference*, pp. 158–164, May 2007.

16. R. A. Coutu Jr., P. E. Kladitis, L. A. Starman, and J. R. Reid, “A comparison of micro-switch analytic, finite element, and experimental results,” *Sensors and Actuators A: Physical*, vol. 115, pp. 252–258, September 2004.

17. R. C. Platteborze, “Microelectromechanical systems (mems) safe-and-arm barrier for low-energy exploding foil initiators (leefi),” Master’s thesis, Air Force Institute of Technology, 2008.

18. G. T. A. Kovacs, *Micromachined Transducers Sourcebook*. McGraw-Hill, 1998.

19. R. A. Coutu Jr., J. R. Reid, R. Cortez, R. E. Strawser, and P. E. Kladitis, “Microswitches with sputtered au, aupd, au-on-aupt, and auptcu alloy electric contacts,” *IEEE Transactions on Components and Packaging Technologies*, vol. 29, pp. 341–348, June 2006.

20. R. A. Coutu Jr., *Electrostatic Radio Frequency (RF) Microelectromechanical Systems (MEMS) Switches with Metal Alloy Electric Contacts*. PhD thesis, Air Force Institute of Technology, September 2004.

21. J. R. Reid and L. A. Starman, “Simulation of cantilever beam micro-switch pull-in and collapse voltages,” *Nanotechnology Conference and Trade Show*, vol. 1, pp. 432–435, 2003.

22. R. A. Coutu Jr., P. E. Kladitis, L. A. Starman, and R. L. Crane, “Rf mems switches with metal alloy electric contacts.”.

23. A. D. Oliver and D. W. Plummer, *The MEMS Handbook*, ch. Surface-Micromachined Mechanisms, pp. 1–20. New York: CRC Press, 2002.

24. C. L. Goldsmith, J. Ehmke, A. Malczewski, B. Pillans, S. Eshelman, Z. Yao, J. Brank, and M. Eberly, “Lifetime characterization of capacitive rf mems switches,” *IEEE Microwave Symposium Digest*, vol. 1, pp. 227–230, May 2001.

25. J. F. Kucko, J. C. Petrosky, J. R. Reid, and Y. K. Yeo, “Non-charge related mechanism affecting capacitive mems switch lifetime,” *IEEE Microwave Symposium Digest*, vol. 16, pp. 140–142, March 2006.

26. B. Lakshminarayanan, D. Mercier, and G. M. Rebeiz, “High-reliability miniature rf-mems switched capacitors,” *IEEE Transactions on Microwave Theory and Techniques*, vol. 56, pp. 971–981, April 2008.

27. G. Gonzalez, *Microwave Transistor Amplifiers: Analysis and Design.* New Jersey: Prentice Hall, second ed., 1997.

28. H. Newman, "Rf mems switches and applications," *Reliability Physics Symposium Proceedings, 2002. 40th Annual*, pp. 111–115, 2002.

29. X. Rottenberg, H. Jansen, B. Nauwelaers, P. Fiorini, W. De Raedt, and H. Tilmans, "Boosted rf-mems capacitive shunt switches," *Workshop on Semiconductor Sensor and Actuator Technology (3rd SeSens)*, pp. 667–671, November 2002.

30. J. R. Reid, L. A. Starman, and R. T. Webster, "Rf actuation of capacitive mems switches," *IEEE Microwave Symposium Digest*, vol. 3, pp. 1919–1922, June 2003.

31. K. M. Strohm, B. Schauwecker, D. Pilz, W. Simon, and J. F. Luy, "Rf-mems switching concepts for high power applications," *Silicon Monolithic Integrated Circuits in RF Systems, 2001. Digest of Papers. 2001 Topical Meeting on*, pp. 42–46, 2001.

32. B. Pillans, J. Kleber, C. Goldsmith, and M. Eberly, "Rf power handling of capacitive rf mems devices," *Microwave Symposium Digest, 2002 IEEE MTT-S International*, vol. 1, pp. 329–332, 2002.

33. H. Yamazaki, T. Ikehashi, T. Ohguro, E. Ogawa, K. Kojima, K. Ishimaru, and H. Ishiuchi, "An intelligent bipolar actuation method with high stiction immunity for rf mems capacitive switches and variable capacitors," *Sensors and Actuators A: Physical*, vol. 139, pp. 233–236, March 2007.

34. J. F. Kucko, *Insulator Charging in RF MEMS Capacitive Switches.* PhD thesis, Air Force Institute of Technology, June 2005.

35. X. Yuan, Z. Peng, J. C. M. Hwang, D. Forehand, and C. L. Goldsmith, "Acceleration of dielectric charging in rf mems capacitive switches," *IEEE Transactions on Device and Materials Reliability*, vol. 6, pp. 556–563, December 2006.

36. S. M. Sze and K. K. Ng, *Physics of Semiconductor Devices.* New Jersey: John Wiley & Sons, third ed., 2007.

37. J. R. Reid, R. T. Webster, and L. A. Starman, "Non-contact measurement of charge induced voltage shift in capacitive mem-switches," *IEEE Microwave and Wireless Components Letters*, vol. 13, pp. 367–369, September 2003.

38. D.-M. Fang, S. Fu, Y. Cao, Y. Zhou, and X.-L. Zhao, "Surface micromachined rf mems variable capacitor," *Microelectronics Journal*, vol. 38, pp. 855–859, 2007.

39. M. Bakri-Kassem and R. R. Mansour, "A high-tuning-range mems variable capacitor using carrier beams," *Canadian Journal of Electrical and Computer Engineering*, vol. 31, pp. 89–95, Spring 2006.

40. J. K. Luo, M. Lin, Y. Q. Fu, L. Wang, A. J. Flewitt, S. M. Spearing, N. A. Fleck, and W. I. Milne, "Mems based digital variable capacitors with a high-k dielectric insulator," *Sensors and Actuators A: Physical*, vol. 132, pp. 139–146, May 2006.

41. A. Sihvola, "Metamaterials in electromagnetics," *Metamaterials*, vol. 1, pp. 1–11, February 2007.

42. C. R. Simovski and S. A. Tretyakov, "Local constitutive parameters of metamaterials from an effective-medium perspective," *Physical Review B*, vol. 75, pp. 195111:1–10, May 2007.

43. S. Miller, "Lighter, stronger, more affordable: Darpa's quests in the realm of materials science," *DARPA*, pp. 128–133, August 2008.

44. D. R. Smith, *Novel Electromagnetic Materials.* Online, http://people.ee.duke.edu/drsmith/neg ref home.htm, Accessed January, 2009.

45. B. Sauviac, C. R. Simovski, and S. A. Tretyakov, "Double split-ring resonators: Analytical modeling and numerical simulations," *Electromagnetics*, vol. 24, pp. 317–338, 2004.

46. A. Degiron, J. J. Mock, and D. R. Smith, "Modulating and tuning the response of metamaterials at the unit cell level," *Optics Express*, vol. 15, pp. 1115–1127, February 2007.

47. G. L. Pollack and D. R. Stump, *Electromagnetism.* New York: Addison Wesley, 2002.

48. I. V. Shadrivov, S. K. Morrison, and Y. S. Kivshar, "Tunable split-ring resonators for nonlinear negative-index metamaterials," *Optics Express*, vol. 14, pp. 9344–9349, October 2006.

49. J. E. Shigley, C. R. Mischke, and R. G. Budynas, *Mechanical Engineering Design.* New York: McGraw Hill, 7 ed., 2004.

50. S. Chowdhury, M. Ahmadi, and W. Miller, "Pull-in voltage calculations for mems sensors with cantilevered beams," *IEEE-NEWCAS Conference, 2005. The 3rd International*, pp. 143–146, June 2005.

51. Q. Meng, M. Mehregany, and R. L. Mullen, "Theoretical modeling of microfabricated beams with elastically restrained supports," *Journal of Microelectromechanical Systems*, vol. 2, pp. 128–137, September 1993.

52. J. G. Korvink and O. Paul, *MEMS: A Practical Guide to Design, Analysis, and Applications.* New York: William Andrew Publishing, 2006.

53. A. Grichener, D. Merrier, and G. Rebeiz, "High-power high-reliability high-q switched rf mems capacitors," *Microwave Symposium Digest, 2006. IEEE MTT-S International*, pp. 31–34, June 2006.

54. F. Schwierz and J. J. Liou, *Modern Microwave Transistors: Theory, Design, and Performance.* New Jersey: John Wiley & Sons, Inc., 2003.

55. N. Engheta and R. W. Ziolkowski, eds., *Metamaterials: Physics and Engineering Explorations.* New Jersey: John Wiley & Sons, Inc., 2006.

56. M. Madou, *Fundamentals of Microfabrication.* New York: CRC Press, 1997.

57. J. Carter, A. Cowen, and H. Busbee, *PolyMUMPs^{TM}Design Handbook.* MEMSCAP Inc, Copyright 1992-2008. Revision 11.0.

58. G. S. May and S. M. Sze, *Fundamentals of Semiconductor Fabrication.* John Wiley & Sons, Inc., 2004.

59. R. C. Jaeger, *Introduction to Microelectronic Fabrication*, vol. 5. New Jersey: Prentice Hall, second ed., 2002.

60. MicroChem, Corp, http://www.microchem.com. Accessed September, 2008.

61. CoventorWare® Inc., Analyzer Ref. Guide, http://www.coventor.com. Accessed September, 2008.

62. M. Robinson, "Private correspondance." January 2009.

63. Agilent Technologies, *4284A Precision LCR Meter Operation Manual*, January 2000.

REPORT DOCUMENTATION PAGE

Form Approved OMB No. 0704–0188

The public reporting burden for this collection of information is estimated to average 1 hour per response, including the time for reviewing instructions, searching existing data sources, gathering and maintaining the data needed, and completing and reviewing the collection of information. Send comments regarding this burden estimate or any other aspect of this collection of information, including suggestions for reducing this burden to Department of Defense, Washington Headquarters Services, Directorate for Information Operations and Reports (0704–0188), 1215 Jefferson Davis Highway, Suite 1204, Arlington, VA 22202–4302. Respondents should be aware that notwithstanding any other provision of law, no person shall be subject to any penalty for failing to comply with a collection of information if it does not display a currently valid OMB control number. **PLEASE DO NOT RETURN YOUR FORM TO THE ABOVE ADDRESS.**

1. REPORT DATE *(DD–MM–YYYY)*
26–03–2009

2. REPORT TYPE
Master's Thesis

3. DATES COVERED *(From — To)*
Sep 2007 — Mar 2009

4. TITLE AND SUBTITLE
A MEMS Multi-Cantilever Variable Capacitor On Metamaterial

5a. CONTRACT NUMBER

5b. GRANT NUMBER

5c. PROGRAM ELEMENT NUMBER

5d. PROJECT NUMBER
08-141

5e. TASK NUMBER

5f. WORK UNIT NUMBER

6. AUTHOR(S)
Luke A. Rederus, Capt, USAF

7. PERFORMING ORGANIZATION NAME(S) AND ADDRESS(ES)
Air Force Institute of Technology
Graduate School of Engineering and Management (AFIT/EN)
2950 Hobson Way
WPAFB OH 45433-7765

8. PERFORMING ORGANIZATION REPORT NUMBER
AFIT/GE/ENG/09-35

9. SPONSORING / MONITORING AGENCY NAME(S) AND ADDRESS(ES)
Air Force Materiel Command, 781 Test Squadron (Brian Sandlin)
871 DeZonia Road
Holloman Air Force Base, New Mexico 88330
(937-349-3323, brian.sandlin@46tg.af.mil)

10. SPONSOR/MONITOR'S ACRONYM(S)
AFMC 781 TS

11. SPONSOR/MONITOR'S REPORT NUMBER(S)

12. DISTRIBUTION / AVAILABILITY STATEMENT
Approval for public release; distribution is unlimited.

13. SUPPLEMENTARY NOTES

14. ABSTRACT Negative refractive index materials are an example of metamaterials that are becoming increasingly popular. Research into these metamaterials could possibly be the first steps toward bending electromagnetic radiation (i.e., microwaves, light, etc.) around an object or person. Split ring resonators (SRR) are classified as metamaterials that create an artificial magnetic response from materials with no inherent magnetic properties. Once fabricated, an SRR has a specific resonant frequency due to its permanent geometry. This research introduces a new concept of using a variable capacitive micro-electro-mechanical system (MEMS) device located at the gap of an SRR to mechanically alter the capacitance of the SRR structure and thus change its resonance. This design simplifies fabrication and offers to use less space than a varactor diode or MEMS switch since the MEMS device is the capacitive element and is fabricated in-situ with the SRR. This research is the first known to demonstrate the fabrication of a MEMS device on an SRR. This thesis reports on the model, design, fabrication, and testing of the capacitive MEMS device as a stand-alone test structure and located on an SRR. When pulled-in, the cantilever beams add between $0.54 - 0.62$ pF.

15. SUBJECT TERMS
MEMS, metamaterial, split ring resonator, varactor

16. SECURITY CLASSIFICATION OF: a. REPORT	b. ABSTRACT	c. THIS PAGE	17. LIMITATION OF ABSTRACT	18. NUMBER OF PAGES
U	U	U	UU	130

19a. NAME OF RESPONSIBLE PERSON
Maj LaVern Starman

19b. TELEPHONE NUMBER *(include area code)*
(937)785–3636,ext4618; lavern.starman@afit.edu